Satellite and Model Data to Inform Solar Radiation Modification Techniques

STATISTICS

Final report

prepared by

Document Change Record

Version	Date	Changes	Originator
v1	23 April 2025	First version prior to PM1 with delivery of Chapter 1 to ESA	Chong Li / Olivier Boucher
v2	3 June 2025	Second version of Chapter 1 updated after comments from ESA	Chong Li / Olivier Boucher
v3	10 Sept 2025	Final version of Chapter 1. First version prior to PM2 with delivery of Chapter 2 to ESA	Chong Li / Olivier Boucher
v4	11 Jan 2026	Merging of Chapters 2 and 3. First draft of Chapter 4 (now Chapter 3).	Chong Li / Olivier Boucher
v5	27 Feb 2026	Final report (submission)	Chong Li / Olivier Boucher

Table of Contents

Purpose and Objectives

Although the Paris Agreement has set ambitious climate targets, current policies are projected to result in approximately 2.7°C of warming by the end of the century, exceeding those goals. While carbon dioxide removal (CDR) is now recognized as a necessary complement to emissions mitigation, its slow deployment raises concerns about a potential overshoot in global temperatures. In response, solar radiation modification (SRM) is gaining attention as a possible – though controversial – backstop, prompting calls for further research despite its associated risks and uncertainties. The STATISTICS project aims to examine the three main SRM techniques – Stratospheric Aerosol Injection (SAI), Marine Cloud Brightening (MCB), and Cirrus Cloud Thinning (CCT) – from a fresh perspective with a focus on how spaceborne Earth observations can be better used and how information from models and satellites can be better integrated together to progress our understanding on these techniques.

The European Union has affirmed its willingness to support international assessments of SRM, and it has received the recommendation – from its Chief Scientific Advisors – to invest into monitoring capabilities.[1] In light of the significant knowledge gaps and the lack of empirical research, this project seeks to support such efforts by examining the current knowledge and data availability and the possibilities for further development. The project therefore maps sources of data, potential small-scale field experiments, and the possibilities of model-based research with a view to gaining clarity on how uncertainties and knowledge gaps might be reduced through dedicated research. It includes a focus on the potential role of satellite data alongside other tools—including artificial intelligence and machine learning.

The project also anticipates future observational requirements for detecting potential SRM deployments and their effects. Such insights would be crucial if the EU seeks to implement the Science Advisors' recommendation to develop monitoring capabilities. Technical capabilities for monitoring would likely be required in case of decisions both for or against the use of SRM. While focusing on scientific and technical questions, the project also seeks to inform governance-related discussions at the international level, where there is a growing recognition that transparent monitoring efforts might be an important element for an internationally collaborative approach to SRM overall and to steer clear of any competitive or confrontational dynamics between countries.

[1] Recommendation 3.5: "Invest in operational Earth observation satellite and other technologies to improve the EU's capability to detect and quantify any undeclared deployment of SRM by public or private actors, anywhere in the world."

Chapter 1. Requirements Baseline Document

As laid out in the STATISTICS proposal, we base the requirements for this project on:

- a review of research gaps from the literature
- a review of existing products, datasets, models and algorithms
- a survey of accessible auxiliary and validation data sets
- an analysis of potential existing observing systems to monitor SRM
- an identification and description of relevant target areas and/or periods
- an analysis of the energy budgets for SAI, MCB, and CCT
- a survey of current and ongoing (public and private) initiatives on SRM research.

This information is summarized in the following subsections, leading to the rationale for the proposed work for the STATISTICS project and an analysis of the potential risks and their impact on the products and project.

1.1 Review of research gaps from the literature

Climate intervention has become a very active field of research with the literature on the topic now growing exponentially. Spontaneous scientific reviews on SRM were regularly published until 2015 to establish our understanding of the physical mechanisms, climate impacts, and uncertainties (e.g., Bellamy et al., 2012; Zhang et al., 2015). As this scientific groundwork matured, governance, ethical considerations, and societal implications also became important, which requires coordinated, transdisciplinary approaches. Consequently, institutional initiatives have superseded individual reviews by addressing SRM within structured frameworks to inform policy and international dialogue (NASEM, 2021; UNESCO, 2023; UNEP 2024; SAPEA, 2024). To inform the STATISTICS project and guide how it can best contribute to the advancement of the field, we focus on three recent studies that analysed research gaps based on the available literature. This approach allows for a more strategic and policy-relevant research agenda than broad reviews. The three studies in question are Feingold et al. (2024), which deals specifically with the MCB technique, and Haywood et al. (2025) and Eastham et al. (2025), which address all of SAI, MCB, and CCT techniques.

Marine Cloud Brightening (MCB) involves the intentional introduction of aerosol (sea-salt) particles into shallow marine clouds to enhance their cloud droplet number concentration and hence their reflectivity, thereby increasing the amount of solar radiation reflected by the climate system. From a physical science perspective, Feingold et al. (2024) consider that the viability of MCB depends on its potential to scale up from local to more regional or even global scales and how this scalability can be assessed robustly using observations and models. Given the heterogeneous nature of MCB, another issue is how

to develop strategies that ensure an equitable geographical distribution of both the benefits and risks associated with potential regional changes in temperature and precipitation. To bridge key physical science knowledge gaps necessary for assessing the societal implications of MCB, Feingold et al. (2024) advocate for a comprehensive and focused research program, encompassing field and laboratory experiments, systematic monitoring, and numerical modeling across multiple spatial and temporal scales. It is clear that Earth observations from space would have to play a critical role in such an endeavour.

Haywood et al. (2025) examined research gaps associated with each of the SAI, MCB and CCT techniques – the latter being extended with Mixed-phased Cloud Thinning (MCT). We display their findings in Table 1.1 as a list of research gaps in five categories that go from fine to large scale and more holistic considerations: generation and delivery of particles into the atmosphere, process-level understanding, scale required and deployment strategies, large-scale circulation response, and impacts. CCT and MCT being less mature, the identification of research gaps follows a less structured approach.

Table 1.1. Research gaps identified by Haywood et al (2025).
The research gaps addressed in this study are highlighted with grey shading.

SAI	**Generation and delivery** Quantification of technical barriers and costs. Credible estimates for delivery timescales for deployment systems. Joined-up collaboration. A framework for evaluating financial risks.
	Process-level understanding Model sophistication (aerosol microphysics, gas-particle interactions). Consistency of GCM (General Circulation Model) results. Number of models capable of modelling impacts on stratospheric ozone. Study of alternate particles to sulfates.
	Scale required and deployment strategies The large uncertainties in metrics associated with SAI. The small number of CMIP models that have engaged in GeoMIP simulations. The limitations in scenarios and strategies. Coupling with technical feasibility.
	Large-scale circulation response Characterization of the stratospheric circulation. Understanding of stratospheric circulation response. Representation of stratosphere-troposphere exchange in models. Impacts on dynamics in the troposphere and ocean.
	Impacts Understanding of ecosystem response. The oversimplification of climate-biosphere interactions. The air-quality response to SAI.

MCB	**Generation and delivery** Practical technological limitations of delivery on emission rate, altitude, and particle size distribution and their impact on cloud microphysical and macrophysical properties. Limited experimental evidence from deployments. Consistency between aerosol activation schemes. Paucity of high-resolution modelling studies of MCB. Traceability from process scale to the global scale.
	Process-level understanding Representation of key microphysical processes. Process-level validation of aerosol-cloud-interactions in GCMs. Process-level understanding across a range of cloud-regimes. Understanding large-scale changes in aerosols.
	Scale required and deployment strategies Realism in MCB deployment strategies. The potential synergetic role of Marine Sky Brightening (MSB) Multi-model studies targeting the amelioration of other impacts of global warming such as protecting sea-ice, ecologically sensitive regions such as coral reefs, or cooling specific regions such as the Mediterranean.
	Large-scale circulation response Model dynamical responses of regional cooling and associated inter-model consistency need to be thoroughly investigated using a suitable risk–risk framework. The role of the oceans in redistributing thermal anomalies associated with MCB. The additivity (or lack of) of regional MCB deployments.
	Impacts Engagement with the marine biology/ecological community. Engagement with the community engaged in modelling fisheries.
CCT and MCT	**Susceptibility**: It is not clear whether a sufficient number of cirrus and mixed-phase clouds are susceptible to seeding in regions and seasons that would yield significant cooling. **Scalability**: The bounds on the effective radiative forcing and associated cooling that could be achieved by CCT, MCT, or a combination of the two, is highly uncertain. **Interdependency**: It is not clear whether CCT and MCT are inextricably linked, such that one cannot occur without the other.

Eastham et al (2025) further assessed the gaps in SRM research by reviewing sources of uncertainties. They identified two common areas of improvements needed across all three techniques: “a common focus on the demand for more observations to better constrain models and improve process-level understanding” and “improving the consistency of process representation across models of different scales”. The research gaps they identify are displayed in Table 1.2.

Table 1.2. Research gaps identified by Eastham et al (2025).
The research gaps addressed in this study are highlighted with grey shading.

SAI	1/ The first modeling gap that has been identified is representation of detailed microphysical changes in the stratospheric aerosol layer that occur when aerosols or their precursors are injected into the stratosphere. 2/ A second key modeling gap to address is model uncertainties in aerosol interactions with radiation, in particular uncertainties under SAI in (a) the radiative heating response in the stratosphere; (b) changes in radiative forcing at the surface; and (c) changes in tropospheric photolysis. 3/ A third major modeling gap is missing or poorly-simulated aerosol interactions with chemistry.
MCB	1/ A fundamental first need is to improve models' ability to represent MCB aerosol emissions using realistic aerosol size distributions. 2/ A second issue regards accurately representing the point-source nature of MCB. 3/ How cloud macrophysical responses to aerosol perturbations are affected by the timing and spatial distribution of the injection strategy?
CCT	1/ The key dynamical gap is our ability to simulate the occurrence, location, intensity, and extent of ice supersaturated regions. 2/ The key cloud-physics gap is in the microphysics of cirrus cloud formation, which inhibits advances in knowledge on cirrus clouds and CCT. 3/ Central among these gaps is the uncertainty surrounding the properties of cirrus formed on seeded aerosols.

It can be seen from these three studies that research gaps are diverse and encompass a large range of scales and tools. Current approaches have focused on the use of models (from process models to climate models), the analysis of observational datasets, and synergetic uses of both. Natural analogues to SRM techniques (e.g., explosive volcanic eruptions in the stratosphere, passive volcanic degassing in the lower troposphere, soot emissions from commercial aircraft) represent interesting case studies that can inform the processes involved in SAI, MCB and CCT. Studying natural analogues has already contributed a lot of knowledge but they have not been fully exploited yet and continue to provide a useful framework to learn more on relevant processes. However, for some research gaps (e.g., those related to generation and delivery), SRM research is approaching a point where field experiments will be needed if further progress is to be made. While field tests remain controversial, it should be noted that field tests have already taken place (e.g., Great Barrier Reef MCB trials) and that further field tests have been funded or are planned outside the European Union. Within this context, there are several reasons why Earth observations from space are particularly relevant:

- **Process-level understanding**. Some processes are still poorly understood; the combination of satellite retrievals of aerosols and clouds and modelling will play a crucial role in improving our understanding of aerosol microphysics and aerosol-cloud interactions, in particular from natural analogues.

- **Monitoring of field tests**. Satellite observations could play a role to monitor field tests in a wider environment (and to plan such field tests if this is considered to be a sound approach).

- **Monitoring of deployment**. Monitoring of the potential impacts of SRM on all components of the Earth's system would become critical if there were a deployment (whether it is unilateral or collaborative).

Observing systems need to have the capability to detect small perturbations to be effective. This may be challenging for field tests as such experiments would likely involve fairly small modification of aerosol and clouds fields (e.g., injections of a few hundred kg of SO_2 in a putative SAI experiment). It is likely that satellite instruments will require enhanced sensitivity to detect and observe such field experiments.

Research gaps also exist in the social sciences and humanities including on how scientific and technical cooperation could strengthen international governance and how international cooperation on monitoring could unlock governance opportunities as tentatively observed by scholars of nuclear non-proliferation (Philippe, 2019) and explored in some of the SRM governance literature (Brent et al., 2024).

A commonality of these research gaps is that many can only be addressed through a coordinated and often interdisciplinary effort as all components of the Earth's system are potentially affected.

1.2 Review of existing products, datasets, models and algorithms

As discussed above, SRM methods have been primarily evaluated through model simulations and analysis of natural analogues in observational datasets. Specifically, **models** can be used to i) evaluate particular processes, ii) simulate natural analogues to test relevant processes against observations, iii) perform idealised experiments of SRM to gain understanding in the large-scale climate response, and iv) perform more realistic experiments of SRM deployment. The model simulations may be multi-model ensembles (to test the robustness of the findings to uncertainties in model formulations) or initial-condition ensembles (to test the robustness of the findings to climate variability). In order to guide the work to be done in STATISTICS, we compiled in Table 1.3 a list of model datasets relevant to SRM research that are publicly available. STATISTICS will use four of the models involved in GeoMIP and ISA-MIP.

Table 1.3. Model datasets relevant to SRM research.
PR: processes. NA: natural analogues. ID: idealised experiments. RE: realistic experiments. MME: multi-model ensemble. ICE: initial-condition ensemble.

GLENS and ARISE-SAI-1.5 were performed with the Community Earth System Model.

Dataset	Type	Location	Reference
GeoMIP, phase 5	ID, MME	ESGF, https://aims2.llnl.gov/search Then select CMIP5 and GeoMIP project	Kravitz et al. (2013)
GeoMIP phase 6	ID/RE, MME	ESGF, https://aims2.llnl.gov/search Then select CMIP6 and GeoMIP project	Kravitz et al. (2015)
GLENS	RE, ICE	https://www.cesm.ucar.edu/community-projects/glens/diagnostics	Tilmes et al. (2018)
Aerosol injection	PR, MME	https://dataverse.harvard.edu/dataverse/AM-H2SO4_Intercompare_Data	Weisenstein et al. (2021)
ISA-MIP	NA, MME	https://isamip.eu/models	Timmreck et al. (2018)
ARISE-SAI-1.5	RE, ICE	https://doi.org/10.26024/0cs0-ev98 https://doi.org/10.5065/9kcn-9y79 https://registry.opendata.aws/ncar-cesm2-arise/	Richter et al. (2022)

There are a multitude of **observational datasets** that can be used to study SRM-relevant processes and/or SRM analogues though none of the datasets is “SRM-ready” and substantial pre-processing and treatment may be needed. Most studies tend to rely on available satellite datasets, e.g. from ESA or NASA (see below) and/or reanalysis (e.g., CAMS and MERRA-2). The requirements for studying SRM analogues are not different from those to study aerosol and clouds in a general sense. We provide below a list of satellite and ground products useful for SRM related impact monitoring and observational gaps.

Ground-Based & In-situ Products

Ground-based and in-situ instruments and networks can monitor aerosols and radiation. They could potentially detect aerosol and/or radiative changes potentially caused by SRM.

Table 1.4. Ground-based observational datasets relevant to SRM research.

	Instruments/ Networks	Parameters	Notes
Aerosol Monitoring	Sun-photometers/ AERONET	Aerosol Optical Depth (AOD), Ångström exponent, size distribution, other	Based on the retrieved aerosol properties, AERONET also

		optical properties (e.g., scattering, absorption) in the atmospheric column	provides calculated broadband solar flux at the top and bottom of the atmosphere
	Max-DOAS, Pandora/ Pandonia	Column trace gas (e.g., NO_2, O_3) in the troposphere and in the column	
	LIDAR/ EARLINET, MPLNET	Profiles of aerosol layers (backscatter, extinction)	Useful for detecting stratospheric aerosol layers
	Sun-photometers/ GAWPFR, SKYNET	Direct solar radiation to infer aerosol properties	
	ACTRIS	Measurements of the parameters mentioned above including from in-situ measurements	
Radiation Flux Measurements	BSRN (Baseline Surface Radiation Network)	Surface solar and terrestrial radiation fluxes	High precision. Useful for detecting changes in surface radiation
	SURFRAD	Surface radiation budget	
	Others (Pyranometers / Pyrgeometers)	Incoming shortwave and longwave radiation	
Atmospheric Composition	Dobson and Brewer Spectro-photometers	Total column ozone	Useful in tracking potential ozone depletion from SAI
	Radiosondes	Vertical profiles of temperature, humidity, and pressure	
In-Situ instrumentation	Aircraft and balloon platforms	Direct aerosol particle size, composition, and radiative properties in the stratosphere	Limited spatial and temporal coverage; not feasible for continuous or global monitoring

Satellite-Based Products

Satellites provide global, and potentially long-term datasets that are extremely useful to study natural analogues and could help detect SRM activities, particularly in the stratosphere and in terms of its impact on the radiation budget.

Table 1.5. Satellite-based observational datasets relevant to SRM research.

	Instruments/ Satellites	**Parameters**	**Notes**
Missions/ datasets relevant to aerosol and cloud studies	CALIOP/CALIPSO	Profiles of aerosol and cloud layers	Useful for detecting high-altitude particles; Challenging to distinguish ash/sulphate mixtures (Tackett et al., 2023)
	MODIS/ Aqua,Terra	Aerosol column properties, cloud properties, surface albedo	
	OMPS Limb Profiler / Suomi-NPP, NOAA-20	Stratospheric aerosol and ozone profiling	
	SAGE III / ISS (International Space Station)	Vertical profiles of aerosols, ozone and other trace gases	"Errors at the peak of the stratospheric aerosol layer range from 20-25% for median radius and 5-7% for mode width". These retrieval uncertainties limit the precision of aerosol size distribution estimates – important for identifying engineered aerosol vs. volcanic or natural background sources (Wrana et al., 2021). Detects 1-2 Tg S/y in steady state globally, it cannot detect injections <1 Tg S/y during initial phases (Lange et al., 2025).

	ATLID, CPR, MSI / EarthCare	AOD, aerosol profiles, TOA radiation, cloud structures	
	OMI/Aura	Ozone, aerosols, and UV radiation	
	GOME-2/MetOp	Atmospheric composition	UV-visible spectra; Useful for ozone and aerosol tracking
	AIRS, MLS/Aqua	Trace gases (total column & vertical profiles), water vapor profiles	
	MISR/Terra	Aerosol and cloud properties	Moroney et al., 2012; Kahn et al., 2010;
	IASI/MetOp-A/B/C	SO_2 total column and layer height	Other trace gases too
	POLDER /PARASOL	Polarimetric aerosol and cloud properties; Derived aerosol composition (fraction and volume concentration of soluble aerosol (ammonium, sulfate, nitrate), non-absorbing dust and absorbing components (BC, BrC, FeOx) in total atmospheric column	Buriez et al., 1997; Deuzé et al., 2000; GRASP/Components algorithm (Li et al., 2019) developed and applied to POLDER/ PARASOL;
	3MI (Multi-viewing, Multi-channel, Multi-polarization Imager) mission (future)	Polarimetric monitoring of clouds/tropospheric aerosols	GRASP/component to be applied to future 3MI (day+1 product); Fougnie et al., 2018
	HARP2, SpexOne, OCI/PACE	Plankton, aerosol, cloud properties	Multi-angle polarimeters & spectrometer; Hasekamp et al., 2019
	ALADIN Lidar/Aeolus	Aerosol properties	First high-spectral resolution lidar in space (2018-2023); Flament et al., 2021; Gkikas et al., 2023

	OSIRIS/ODIN	Stratospheric aerosol extinction at 750 nm with vertical profiles	Limited to the Northern/Southern Hemisphere seasonally; lacks continuous global coverage. Bourassa et al., 2012.
	CERES (Clouds and the Earth's Radiant Energy System)	Direct measurements of reflected solar and emitted thermal radiation across UV to far-infrared wavelengths	Can detect large-scale SRM deployment but require substantial effects for small experiments; Siedel et al., 2014.
	GloSSAC (Global Space-based Stratospheric Aerosol Climatology) v2.2	Stratospheric aerosol dataset	1979–present; Kovilakam et al., 2020, 2023
	CREST v2	Stratospheric aerosol dataset	October 1984 until December 2023; Sofieva et al. 2024
Sentinel Satellites (Copernicus Programme)	MSI/Sentinel-2	Surface reflectance, NDVI, Albedo, land cover classifications	High-resolution (10–60m) multispectral imagery; Detection of vegetation changes from altered radiation, detection of cloud brightening or surface reflectivity interventions.
	OLCI, SLSTR /Sentinel-3A/B	AOD, sea/land surface temperature, Cloud cover and cloud top properties, Radiation budget elements (radiance, reflectance)	Atmospheric aerosol retrievals, water vapor, and ocean color can be helpful for indirect detection of SRM effects over oceans
	TROPOMI/ S5-P	SO_2, NO_2, O_3, HCHO, CH4, aerosol layers	High-resolution trace gas monitoring

	UVN Spectrometer /Sentinel-4 (upcoming)	O_3, SO_2, aerosol properties	High temporal resolution; Useful for continuous monitoring of rapid changes associated with regional SRM trials.

1.3 Survey of accessible auxiliary and validation data sets

For SAI and MCB natural analogues, SO_2 data represent an important auxiliary input. An example of a coupled SO_2 and sulphate aerosol can be the RAL-Space IMS product, which has been used in the context of the Hunga Tunga eruption (Sellitto et al., 2024). The Volcplume web platform, developed by collaboration of Univ.Lille/LOA and AERIS national center for atmospheric data and services (Boichu and Mathurin 2022, see https://dx.doi.org/10.25326/655), and the associated SO_2 flux calculator can inform on daily SO_2 mass time series from various polar orbiting Low Earth Orbit satellite sensors including the most recent S5P/TROPOMI. This is particularly useful for recurrent or long-term eruptions to diagnose periods when the volcano is actively erupting or degassing. The methodology is described in Grandin et al. (2024).

Ground-based FTIR instrument lidar measurements from NDACC, and the AERONET sunphotometer network can provide useful information to measure SO_2 (and other gases) as well as aerosol optical and microphysical properties. Boichu et al. (2023) provide an example of how SO_2, aerosol size distribution and composition could be informed using a synergy of instruments.

Other datasets are potentially useful to study SRM methods such as

- reanalysis data (e.g., ECMWF ERA5, CAMS, MERRA-2) that synthesize atmospheric data integrating model, satellite and ground data,
- UV index measurements that can indicate changes in stratospheric ozone.

1.4 Analysis of existing observing systems to monitor SRM

Monitoring SRM (whether a field test or at deployment stage) would require an observing system that is not necessarily the same as for progressing the scientific knowledge on the topic. Different satellite observing systems exist that can be used to detect, monitor and track SRM interventions and their impacts on the atmospheric composition and the radiative balance, but a more comprehensive system would be needed for a thorough monitoring.

The most obvious natural analogues for SAI interventions are from stratospheric volcanic eruptions. The stratospheric aerosol perturbations resulting from moderate volcanic eruptions have been observed primarily with existing: 1) solar occultation, 2) limb scattering, 3) limb emission, and 4) space LiDAR sensors. These different techniques all have their own sensitivity to stratospheric aerosols and have their own horizontal, vertical and temporal resolution. As an example, solar occultation observations of sensors like SAGE III on the International Space Station (SAGE III/ISS) have proven very sensitive to the stratospheric aerosol perturbations resulting from moderate volcanic eruptions but can miss the crucial small-spatial-scales phases occurring during and immediately after the volcanic SO_2 injection (e.g. Kloss et al., 2021). A scarce spatiotemporal coverage is also a strong limitation of the otherwise very sensitive space LiDAR observations, such as those from CALIOP-CALIPSO, in the recent past, and EarthCare-ATLID, at present. On the contrary, limb scattering observations, such as those from the OMPS-LP sensor, have a scarcer sensitivity but much better spatial coverage than solar occultation or space LiDAR instruments (e.g. Sellitto et al., 2022). These instrumental techniques are all based on the observation of the ultraviolet/visible range of the Earth's spectra. This range, unfortunately, is not sensitive to the composition of the aerosol perturbation and can only bring a limited information on the aerosol microphysical properties (even if recently methodologies have been proposed to derive stratospheric aerosol size distribution information from solar occultation observations, see e.g. Duchamp et al., 2023). Specific composition information, and then a specific aerosol-type detection, can be obtained using the infrared range of the Earth's spectra, with solar occultation observations, such as those from ACE-FTS (e.g. Bernath et al., 2023). Some column-integrated information can also be derived from infrared nadir-looking instruments, like the IASI (e.g., Sellitto et al. 2024). With infrared observations, the simultaneous retrieval of SO_2 injections and the resulting sulphate aerosols, as well as their spatiotemporal evolutions, can also be obtained. For all these different techniques, it might be, nevertheless, quite arduous to detect small-intensity "near-term" SAI interventions (i.e. thousands or millions or times smaller than a moderate volcanic eruption.), including unilateral interventions or experiments, due to their relatively large detection limits. It was recently shown that new-generation high-spectral-resolution limb emission sensors, like CAIRT, are expected to be able to detect these "near-term" experiments, with limited uncertainties on spatiotemporal location and mass of the SO_2 injection (CAIRT Report for Mission Selection, under review). Unfortunately, the CAIRT concept mission was not finally selected as the ESA's 11th Earth Explorer mission. In practice a combination of satellite instruments, i.e. from nadir and limb observing geometries, or from active and passive techniques, is required to bring the most reliable information.

Understanding MCB and CCT also benefits from Earth observations that characterise and monitor cloud amount and properties on a global scale by focusing on regions where

aerosols are perturbed, either for natural or anthropogenic reasons. By providing consistent, high-resolution data across temporal and spatial domains, satellites enable the retrieval of key cloud parameters such as cloud fraction, optical thickness, effective radius, cloud top height and temperature, and phase (liquid or ice). Passive sensors, including radiometers and spectrometers operating in the visible, infrared, and microwave domains, contribute significantly to long-term climatologies and trend analyses, while active sensors such as spaceborne lidars (e.g., CALIOP) and radars (e.g., CloudSat) offer vertical profiling capabilities essential for understanding cloud vertical structure and microphysical properties. ML techniques have proved useful to bridge between different instruments that have different strengths but also varying swaths and revisit times. As discussed above, the new generation of polarimeters has a large potential to monitor aerosols and clouds and would represent an important element in a monitoring system. Table 1.6 outlines the observational limitations, gaps and highlights the improvements needed for SRM monitoring.

Table 1.6. Current observational gaps, limitations, and monitoring needs relevant to SRM research.

Category	**Limitations**	**Needs for SRM monitoring**
Stratospheric Aerosol Profiling Limitations	No continuous, high-resolution global monitoring of stratospheric aerosols, especially in the upper stratosphere or over the poles.	Global high-vertical-resolution limb and occultation sensors for continuous stratospheric aerosol tracking.
Temporal Resolution	Lack of high-frequency (hourly or better) monitoring from polar satellites, especially over oceans. Geostationary satellites for air quality are still emerging.	Deployment of geostationary aerosol and gas sensors over under-monitored regions like the Pacific and Southern Hemisphere.
Low AOD detection & lack of absorption properties	Difficult to detect localized low AOD from experimental SRM due to low contrast with background aerosols. Accurate satellite absorption metrics (e.g., SSA) are lacking.	Improvement of satellite based AOD and especially other (absorption, SD) properties.
Ground-based solar network	Sparse coverage of ground-based solar networks in remote areas and developing countries especially in Africa and parts of Asia.	Expansion of ground-based radiation and aerosol networks, especially in Africa and the Southern hemisphere.

Trace Gas high resolution detection related uncertainties	Source attribution models are underdeveloped for small-scale or covert SRM activities.	Unmanned aerial systems (UAS) and stratospheric balloons for in situ aerosol and gas measurements.
Satellite data validation in Key Areas	Validation and calibration of satellite data in these regions are poor, increasing uncertainty in global detection.	
Satellite retrieval limitations	Limitations of satellite retrievals in polar areas and bright surfaces.	
Stratospheric AOD change detection sensitivity	Changes of less than 20% in stratospheric AOD levels cannot be detected confidently, which means that small-scale or early-stage SRM activities (e.g., trial SAI deployments) may fall below satellite detectability thresholds (Kremser et al., 2016).	

Data assimilation systems such as CAMS or MERRA-2 would also play a critical role in any monitoring system by optimally combining model and information. However, this implies adapting the underlying models so that it includes the best available information on how SRM is deployed.

Finally, it should be noted that international monitoring of SRM would involve a lot more than an observing system. Felgenhauer et al. have fleshed a framework for such international monitoring, which is reproduced here, as it represents an interesting framing for this and subsequent projects on SRM methods (see their poster below). Current discussions point to non-technical challenges which include the need for keeping pace with future SRM developments, the low priority of SRM on current policy agendas, the need for building trust and countering misinformation, the concentration of technical capabilities among a few nations, and the setbacks from reduced U.S. engagement in international climate science and diplomacy, necessitating strategies to compensate for lost technical and institutional contributions.[2]

[2] A workshop convened by the independent think tank Centre for Future Generations explored such governance implications, challenges and opportunities for strengthening international collaboration.

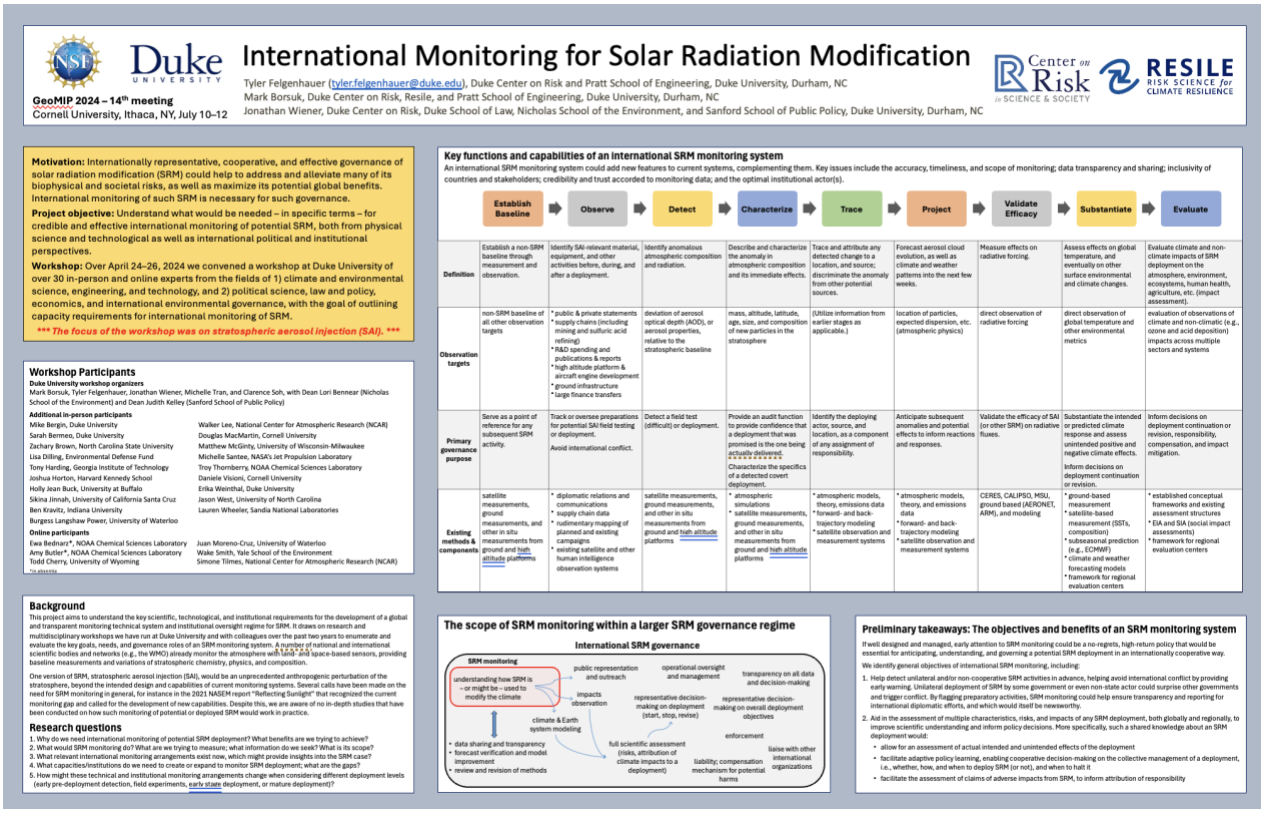

1.5 Identification and description of relevant target areas and/or periods

In order to define the work to be done in STATISTICS, we compiled and present below a list of natural (and industrial) analogues for SAI, MCB and CCT in Tables 1.7 to 1.9. Many of these have already been studied (see references) but it may still be possible to get new knowledge by revisiting some of these using better or synergetic satellite products. These natural analogues may also be modelled to evaluate relevant processes and their uncertainties. This analysis forms the basis to define the content of WP2100/2200/2300 and 3100/3200/3300 (see Section 1.8).

Table 1.7. Natural analogues for Stratospheric Aerosol Injection. The natural analogue selected for this project is indicated with grey shading (see Section 1.8).

Eruption	Eruption periods	References
Pinatubo, Philippines	June 1991	Quaglia et al. (2023) Kleinschmitt et al. (2017) Many other articles.

Sarychev, Japan	June 2009	Haywood et al. (2010)
Ambae, Vanuatu,	April and July 2018	Kloss et al. (2020)
Raikoke, Russia	20 - 21 June 2019	Wrana et al. (2023)
Ulawun, Papua New Guinea	26 June 2019, 3 August 2019	Wrana et al. (2023)

Table 1.8. Natural analogues for Marine Cloud Brightening. The natural analogue selected for this project is indicated with grey shading (see Section 1.8).

Eruption / Event	**Eruption periods**	**Reference**
Holhauraun, Iceland (North Atlantic)	Fissure eruption, 2014-2015	Malavelle et al. (2017) (10.1038/nature22974) Schmidt et al. (2015)
Kilauea, Hawaï, Tropical West Pacific	June 2008 May 2018 29 Sept 2021 - 9 Dec 2021 5 Jan 2023 - 7 March 2023 (61 days) 7 June 2023 - 19 June 2023 (13 days) 10 Dec 2023 - 16 Dec 2023 (7 days) 15 Sept 2024 - 20 Sept 2024 (6 days) 23 Dec 2024 => January 2025	Breen et al. (2021) (10.5194/acp-21-7749-2021) Flower et al. (2021) (10.1016/j.jvolgeores.2021.107247) Chen et al. (2024) (10.1038/s41561-024-01427-z)
Ambae, Ambrym, and Yasur, Vanuatu, Tropical East Pacific	On and off since 2004 with peaks in 2018 (not sure after 2018)	Bani et al. (2012) Carn et al (2017) Shreve et al. (2019)
Composites	900 volcanic plumes	Toll et al. (2017) (10.1002/2017GL075280)
IMO 2020	Rapid reduction in sulphur content of shipping fuels following IMO 2020 regulation. Comparison of pre-2020 and post-2020 cloud albedo in shipping regions. Comparison of the contrast across shipping lanes before and after 2020.	Yuan et al. (2022) (10.1126/sciadv.abn7988) Watson-Parris et al. (2022) (10.1073/pnas.2206885119) Diamond (2023) (10.5194/acp-23-8259-2023)

Table 1.9. Natural analogues for Cirrus/Mixed-phase Cloud Thinning.

Event	**Eruption/event period**	**Reference**
COVID-19 aircraft traffic reduction (reduced soot)	Reduced global aircraft emissions (soot specifically) in 2020 - analogues for CCT in reverse	Zhu et al. (2022) (10.1029/2021AV000546)

Industrial ice nucleating particle (INP) point-source emissions observed by MODIS	Mixed-phase cloud glaciation events observed by MODIS at industrial point sources in the mid/high northern latitudes over the period 2000-2021. Analogues for mixed-phase cloud thinning.	Toll et al. (2024) (10.1126/science.adl0303)

1.6. Analysis of the energy budgets for SAI, MCB and CCT

For each of SAI, MCB and CCT, we estimate from thermodynamic principles the minimum energy budget required to conduct a unit SAI, MCB or CCT (E_i, energy invested) and by how much it may cool the planet (E_r, energy returned to the planet). We define the leverage of SRM techniques as the energy returned on energy invested (ERoEI, a concept that we borrow from energy economics). In a second step we also estimate by how much this minimum energy budget could be reduced by piggy-backing on natural processes or in contrast increased in a more realistic implementation. To put these numbers in perspective, we then estimate the power required to cool the planet by 1 Wm^{-2} as this represents a typical value to cool the Earth by about 1°C if applied in the long term. For the sake of comparison, the current estimate of the total anthropogenic radiative forcing is ~3 Wm^{-2} and that of the Earth Energy Imbalance is ~1 Wm^{-2}. We also compare the required power to sustain a 1 Wm^{-2} radiative forcing to the world's consumption of energy. Indeed, SRM techniques are only viable if they have a strong leverage and do not involve too strong feedback on greenhouse gas emissions.

Energy budget for SAI

Injection of aerosols in the stratosphere can be achieved from a few locations but requires at least some injection in the Tropics where the tropopause is the highest. We consider here an injection point at an altitude of 20 km. The minimum energy necessary to actively lift m=1 kg of sulfur (S) to a height z=20 km is given by its change in potential energy:

$$E_i = m\ g\ z \approx 1 \times 10 \times 20000 = 2\ 10^5\ J \qquad (1.1)$$

It would cause a radiative cooling (energy forcing) that can be estimated from the radiative efficiency of sulfate aerosols in the stratosphere:

$$E_r = (M_{SO4} / M_S)\ RE_{SO4}\ t_{SO4} \approx 10^{13}\ J \qquad (1.2)$$

with $M_{SO4} / M_S = 3$ is the ratio of the molecular masses of SO_4 and S, $RE_{SO4} = 100$ W/g is the typical cooling efficiency of stratospheric sulfate aerosols and $t_{SO4} = 1$ year is the typical lifetime of sulfate aerosols in the stratosphere.

Hence the maximum leverage of SAI or ERoEI is estimated to be $5\ 10^7$ (1 joule used for lifting the S to the stratosphere would bring a maximum of 50 million joules of cooling for the planet). This estimate should be qualified for several reasons. First the cost of lifting

the sulphur to the stratosphere could be much larger as the most likely delivery method is through aircraft which have a limited payload and efficiency. Smith (2020), building on Smith and Wagner (2018), estimated that 250 gallons of jet fuel were needed to lift 1 ton S using a fleet of aircraft, which would correspond to 3.3 10^7 J/kg (computed as 250 x 3.78 l/gallon x 35 MJ/l /1000 kg/ton) and would bring additional CO_2 emissions. The energy cost would be twice larger if SO_2 were to be lifted instead of S. Therefore, a more conservative estimate could be 10^8 J/kg to account for various inefficiencies, which would give a leverage or ERoEI of 10^5.

The power necessary to maintain a radiative forcing $\Delta F = -1$ Wm^{-2} would be

$$P_i = E_i * Flux_S = E_i * \Delta F * S_T / E_s = 5 \text{ GW} \quad (1.3)$$

where S_T is the Earth's surface area.

The energy cost of lifting the S could be less if it could be emitted at a lower altitude. This could be the case if the S is emitted at high latitudes where the tropopause is lower but the efficacy of the method would be significantly less because of a shorter aerosol lifetime. It could also be the case if the S gets transported into the stratosphere (e.g. due to self-lofting) but the scientific basis for this option is missing.

Alternatively, the sulfur could be emitted as a chemical compound that is inert in the troposphere, gets transported to the stratosphere through the global circulation where it gets broken down and can be oxidised to sulphuric acid. Surface emissions of carbonyl sulfide (COS) have been proposed as such an alternative approach that would alleviate the need for the deployment of stratospheric aircraft (Quaglia et al., 2022). However, the rate of COS uptake by soils and plants and the negative impact of prolonged human exposure to this chemical are not known. For these reasons we do not consider this option further to quantify the energy budget for SAI.

In all cases, the energy cost of mining and manufacturing the sulfur compounds would also need to be accounted for.

Energy budget for MCB

We now perform a similar analysis for MCB. The minimum energy requirement for spraying one unit mass of seawater from bulk water is given by the surface energy associated with surface tension of the sprayed droplets and their kinetic energy:

$$Ei = \gamma \cdot 4 \pi r^2 + 1/2 \, m \, v^2 \quad (1.4)$$

where γ is the surface tension of seawater, r is the radius of the sprayed particle, m its mass and v its speed. When expressed per unit mass of seawater and assuming the distribution is monomodal, the minimum energy requirement takes the form:

$$Ei = 3 \gamma / (\rho r) + 1/2 \, v^2 \quad (1.5)$$

where ρ is the seawater density. For submicronic particles, the required energy is generally dominated by the first term. Using γ = 73 mN/m, the surface tension energy is 850 J/kg for 0.25 μm radius seawater particles (corresponding to a dry sea salt particle radius of 70 nm). The values are 1150 and 1930 J/kg for 0.18 and 0.11 μm radius seawater particles (corresponding to dry seasalt particle radii of 30 nm). In comparison the kinetic energy for a release speed of 10 m/s would be 50 J/kg. The minimal energy requirement is thus estimated to be of the order of 1 to 2 10^3 J/kg seawater for optimally-sized sea spray particles. This corresponds to 28-57 10^3 J per sprayed kg of dry seasalt particles after accounting for the seawater salinity of 35 ‰. It is assumed here that the water in the sea spray evaporates naturally in the boundary layer depth at no energetic cost.

For this aerosol size range, Wood (2021) tentatively estimated that a flux of 50-70 Tg/a of dry seasalt particle was needed to offset 3.7 Wm^{-2} forcing, which is much less than in climate model experiments. This corresponds to a cooling expressed per kg of dry seasalt particles of

$$Er = \triangle F_{2xCO2} * S_T / Flux \quad (1.6)$$

where S_T is the Earth's surface and the flux is now estimated in kg/s. The energy returned in this optimistic scenario is therefore 850 10^9 J per kg dry seasalt particles. The maximum theoretical leverage or ERoEi is therefore 1.5 10^7 (1 joule used for producing the seasalt particles would bring a maximum of 15 million joules of cooling for the planet).

The development of spraying technologies aimed at marine cloud brightening has emerged as a new field of research. However, there are to date few estimates of their energetic requirements. Salter et al (2008) estimated the power of a ship to spray at a rate of 30 kg s^{-1} to be 150 kW. However, this did not correspond to any proven or tested spraying technology. More recently Medcraft et al. (2025) demonstrated a system that, if scaled up, could spray 10^{17} particles per second with a power of 3.6 MW (a factor 10 improvement compared to a previous technology). However, the size distribution of the sprayed particles is far from being monomodal and would translate into an energetic cost of 2.5 10^5 J/kg sea spray (to be compared to our best thermodynamic estimate of 1-2 10^3 J/kg). Accounting for various other inefficiencies, the ERoEI is reduced to the order of 10^5.

Energy budget for CCT

CCT works as intended only for large solar zenith angles, corresponding to high latitudes and preferentially in the winter hemisphere. Storelvmo and Herger (2014) concluded that an optimal seeding strategy (at least in the CESM atmospheric model CAM5) would be to seed these areas with approximately 20 particles per liter, corresponding to approximately 40% of Earth's surface at any given time. At the latitudes in question, the tropopause is relatively low, located at an altitude of approximately 9 km. Seeding would

ideally be introduced in a layer just below the tropopause, for example between 7 and 9 km. Research on ice nucleating particles (INPs) indicate that dust particles with an approximate radius of 0.5 μm or larger are efficient INPs, and the approximate dust density is $\rho = 2500$ kg/m^3. Given the relatively short lifetime of medium-sized dust particles in the troposphere (approximately 1 week, Kok et al., 2021), dust particles would have to be re-injected approximately once a week. 40% of Earth's surface area corresponds to approximately 200 million km^2. The volume that should be seeded once per week is thus 400 million km^3 or $4 \cdot 10^8$ km^3. This volume should be seeded with 20 particles per liter, i.e. $2 \cdot 10^{13}$ km^{-3}. Multiplying this with the volume to be seeded, the total number of seeded particles per week would be $8 \cdot 10^{21}$ particles. The mass of a particle is approximately $\rho \pi r^3$, so about $2500 \cdot 4 \cdot 10^{-19}$ kg or 10^{-15} kg. Multiplying this with the total number of particles, we end up with a mass of seeding particles per week of 8 million kg, or 8000 metric tons. Per year, the mass that needs to be lifted would therefore be approximately 400 metric tons. The energy required to lift 400 metric tons to a mean altitude of 8 km is:

$$E_i = m\ g\ z \approx 4\ 10^8 \times 10 \times 8000 = 3.2\ 10^{13}\ J \qquad (1.7)$$

Since this is the mass lifted over a year, the corresponding power would be obtained by dividing by the number of seconds in a year, $3.1\ 10^7$, which yields 1 MW.

The cooling achieved for the above seeding scenario is highly model dependent (-2 Wm^{-2} in CESM/CAM5, significantly less in ECHAM-HAM, see e.g. Gasparini et al., 2020). We choose an intermediate value of -1 Wm^{-2} here. When multiplying with Earth's surface area ($5\ 10^{14}$ m^2), the cooling power becomes $5\ 10^{14}$ W.

This yields an ERoEI of approximately $5\ 10^8$, but this number comes with significant uncertainty, as every single step in the above reasoning is quite uncertain. Optimal seeding concentrations, atmospheric lifetimes, global negative forcing achieved and altitude of delivery are examples of uncertain quantities, but varying these within their plausible ranges would not change the ERoEI by many orders of magnitude.

Summary

A summary of the energy budgets is available in Table 1.10. The maximum theoretical leverages (ERoEi) come out fairly similar for the three techniques (within a factor 10). It is somewhat less for MCB than for SAI but the difference could be compensated by SAI being less efficient so that our estimates of the practical ERoEi are of the same magnitude at 10^5. The practical power needed to maintain a -1 Wm^{-2} cooling is estimated to be 5 GW. This may be compared to the world consumption of primary energy which is about 160,000 TWh[3] that corresponds to 576 EJ or a power of 18,000 GW. Hence the power needed to SAI and MCB is small compared to the world's primary energy. It should be

[3] https://ourworldindata.org/grapher/global-primary-energy

remembered that all these estimates are very uncertain and could be off by at least one order of magnitude.

Table 1.10. Summary table for ERoEI and required power for the three SRM techniques considered in the STATISTICS project.

Method	Max theoretical ERoEI	Min theoretical power for -1 Wm^{-2} cooling	Practical ERoEI	Practical power for -1 Wm^{-2} cooling
SAI	$5\ 10^7$	10 MW	10^5	5 GW
MCB	$1.5\ 10^7$	33 MW	10^5	5 GW
CCT	$5\ 10^8$	1 MW	Not evaluated	Not evaluated

1.7 Survey of current and ongoing initiatives on SRM research

The SRM landscape is evolving rapidly and gaining some understanding of this evolution is critical for making progress and calibrating the R&D effort adequately. We list in Tables 1.11 some past and ongoing initiatives on SRM research worldwide. We adopt a relatively broad definition for “initiatives” but categorize these into professional organisations that have provided an opinion on SRM, private actors operating as a foundation or public charity (and equivalent), international initiatives, and for-profit companies. In addition, some research funding agencies have been funding SRM-related projects as part of their operations at the national or international (e.g. EU) levels.

Professional bodies have shaped the scientific, governance, and ethics discourse on SRM with a few standing out in particular: The Royal Society published its seminal 2009 report, “Geoengineering the Climate,” providing one of the earliest comprehensive assessments of SRM. Another report is under preparation for release later in 2025. The American Geophysical Union (AGU) has issued position statements since 2009, with a notable ethical framework for climate intervention research proposed in October 2024. The US National Academies advanced governance discussions with their 2021 report, “Reflecting Sunlight,” emphasizing research and oversight needs. The World Climate Research Programme (WCRP), through initiatives like the Geoengineering Model Intercomparison Project (GeoMIP), drives critical SRM modeling efforts. A more recent lighthouse activity seeks to coordinate research on “climate interventions”. UNESCO’s 2023 report on climate engineering ethics underscores global governance challenges and the UN Environment Programme (UNEP) has also contributed through its “One Atmosphere” review and SRM discussions at the UN Environment Assembly (UNEA) in 2019 and 2024 highlighting political complexities. In May 2025, UNEP and the World Meteorological Organisation (WMO) jointly held a consultative workshop and science-

policy dialogue on SRM in Geneva. Finally, the SAPEA (Science Advice for Policy by European Academies) report offers a European perspective and recommendations on SRM.

Public and private funding, alongside non-governmental and for-profit entities, further shape the SRM landscape. The UK's ARIA (£56.8m) and UKRI (£10m) programs fund SRM research, while the Simons Foundation supports natural science studies. An interesting new resource is the SRM funding tracker from SRM360.org that is available here (https://srm360.org/funding-tracker/) highlighting the different sources of funding worldwide and their amount. Non-governmental organizations like the Degrees Initiative, which evolved from the Solar Radiation Management Governance Initiative (SRMGI), prioritize developing countries in SRM research capacity development. The Climate Overshoot Commission advocates for risk reduction strategies including a moratorium on SRM deployment as well as public SRM research funding. Organizations such as the Centre for Future Generations (CFG), SilverLining and SRM360.org also support public discussion and informed research, while SRMYouthWatch amplifies youth voices in governance. For-profit ventures like Make Sunsets and Stardust explore commercial SRM applications, reflecting growing private-sector interest. Together, these actors – spanning academia, policy, philanthropy, advocacy, and industry – shape a complex and rapidly evolving SRM ecosystem.

Table 1.11. Past and ongoing initiatives on SRM.

Professional bodies and international organisations

Royal Society	Published the "Geoengineering the climate" report in 2009. New report under preparation.	https://royalsociety.org/news-resources/publications/2009/geoengineering-climate/
American Geophysical Union (AGU)	Early statement adopted in December 2009 in collaboration with the AMS, revised and reaffirmed in February 2012. Position statement adopted in January 2018; revised and reaffirmed in April 2023. Ethical framework proposed in October 2024.	https://www.agu.org/share-and-advocate/share/policymakers/position-statements/climate-intervention-requirements https://news.agu.org/press-release/ethical-framework-climate-intervention-research/
American Meteorological	Early statement adopted by the AMS Council in July 2009. Policy statement	https://www.ametsoc.org/ams/about-ams/ams-

Society (AMS)	adopted in January 2022.	statements/statements-of-the-ams-in-force/climate-intervention
US National Academies	Reflecting Sunlight: Recommendations for Solar Geoengineering Research and Research Governance (2021)	https://nap.nationalacademies.org/catalog/25762/reflecting-sunlight-recommendations-for-solar-geoengineering-research-and-research-governance
WMO ozone assessment	Chapter 6. Stratospheric Aerosol Injection and Its Potential Effect on the Stratospheric Ozone Layer. Published in 2022.	https://ozone.unep.org/sites/default/files/2023-02/Scientific-Assessment-of-Ozone-Depletion-2022.pdf
UNESCO	Report of the World Commission on the Ethics of Scientific Knowledge and Technology (COMEST) on the ethics of climate engineering (2023)	https://www.unesco.org/en/articles/cop28-new-unesco-report-warns-ethical-risks-climate-engineering
Chief Scientific Advisors (GCSA)	Informed by the evidence review report by the Scientific Advice Mechanism and the SAPEA (Science Advice for Policy by European Academies). Published in December 2024.	https://scientificadvice.eu/advice/solar-radiation-modification/
European Group on Ethics (EGE)	Opinion on Solar Radiation Modification	https://op.europa.eu/en/publication-detail/-/publication/80988f27-b5e3-11ef-acb1-01aa75ed71a1/language-en
World Climate Research Programme	Lighthouse Activity on Climate Intervention; WCRP in general coordinates global climate research. The Lighthouse Initiative addresses CDR and SRM.	https://www.wcrp-climate.org/ci-overview
UNEP	One Atmosphere: An Independent Expert Review on Solar Radiation Modification Research and Deployment; UNEA - the political body - has discussed draft resolutions twice to date (2019, 2024)	https://www.unep.org/resources/report/Solar-Radiation-Modification-research-deployment

GeoMIP	The Geoengineering Model Intercomparison Project is a sub-project of the Climate Modelling Intercomparison Project, which itself is a project of WCRP; its work is critical for SRM modelling.	https://climate.envsci.rutgers.edu/GeoMIP/about.html

Public and private funders active on the topic

ARIA	Research funding program: Exploring Climate Cooling (£56.8m).	https://www.aria.org.uk/opportunity-spaces/future-proofing-our-climate-and-weather/exploring-climate-cooling
Simons foundation	Funds natural science indoors research on SRM	https://www.simonsfoundation.org/grant/solar-radiation-management/
UKRI	Modelling environmental responses to solar radiation management – programme (£10m)	https://www.ukri.org/what-we-do/browse-our-areas-of-investment-and-support/modelling-environmental-responses-to-solar-radiation-management/
SilverLining	Advocating for better information on SRM including through research	https://www.silverlining.ngo/
Reflective	Developing SRM knowledge and technology research and development	https://reflective.org/
Harvard global empowerment	University Incubation fund has supported SRM related projects	https://www.hks.harvard.edu/centers/cid/voices/2023-gem-incubation-fund-award-recipients#solar-radiation-modification-impacts-based-dashboard-1847900
University of Chicago, Climate System Engineering Initiatives	CSEi is funding interdisciplinary research projects to advance our understanding of climate systems engineering.	https://climateengineering.uchicago.edu/research/
University of Cambridge, Centre for Climate Repair	Advancing research on solutions for a warming world	https://www.climaterepair.cam.ac.uk/

Non-governmental organizations

Carnegie Climate Governance Initiative	Operated 2016-2023 (concluded its activities)	https://c2g2.net/
The Solar Radiation Management Governance Initiative (SRMGI)	Co-convened by the Environmental Defense Fund, the Royal Society and TWAS, the Academy of Sciences for the Developing World	Set up in 2010, later converted into DEGREES
The Degrees Initiative	Formerly SRMGI. Aims to put developing countries at the centre of the SRM conversation (including through research funding)	https://www.degrees.ngo/
Gordon Research Conference	Hosts specialized meetings focussed on natural sciences, some of which cover SRM.	https://www.grc.org/climate-engineering-conference/2024/
Planetary Sunshade Foundation	Space-based SRM	https://www.planetarysunshade.org/
Climate Overshoot Commission	Reducing the risks of climate overshoot (2023). The CARE agenda.	https://www.overshootcommission.org/report
SRM360.org	Not-for-profit organization	https://srm360.org/
Centre for Future Generations	Think tank / not-for-profit organisation	https://cfg.eu/
The Alliance for Just Deliberation on Solar Geoengineering	Advocating for inclusive discussion of SRM	https://sgdeliberation.org/
SilverLining	Advocating for better information on SRM including through research	https://www.silverlining.ngo/
Reflective	Developing SRM knowledge and technology research and development	https://reflective.org/
SRMYouthWatch	Demanding youth voices be heard in SRM governance (incl. research)	https://www.srmyouthwatch.org/
Operaatio Arktis	Advocating for climate strategies to reality and	https://www.operaatioarktis.fi/

	integrating research and development of climate interventions.	
Resources for the Future	Holds an annual conference on the social science aspects of SRM in Washington DC	https://www.rff.org/events/conferences/2025-rff-and-harvard-srm-social-science-research-workshop-governance-in-a-fractured-world/

For-profit companies

Make Sunsets	Start-up	https://makesunsets.com/
Stardust	For-profit company	https://www.stardust-initiative.com/
MEER	For-profit (cooling) company	https://www.meer.org/

1.8 Rationale for the work proposed in STATISTICS

The work content proposed for the STATISTICS proposal has been refined based on the analyses performed above. It aims to address research gaps that were identified so far, while exploiting the strengths of the STATISTICS team and achieving the results on time and on budget keeping in mind the short timeframe for the project.

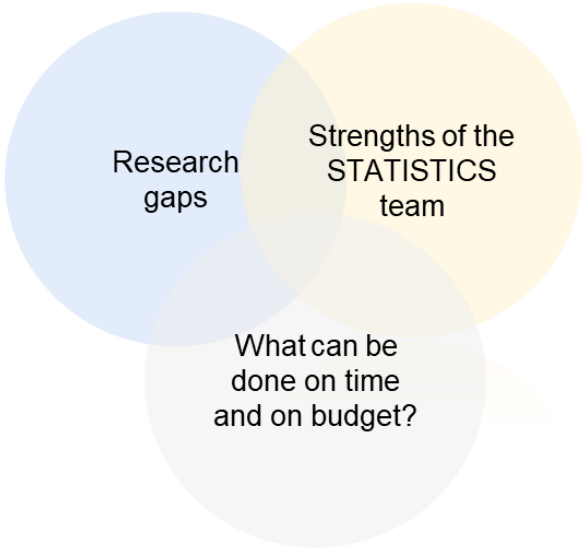

Measurements from spaceborne polarimeters and lidars were identified as being good candidates to provide further insight into SRM analogues. CALIOP-CALIPSO and EarthCare-Atlid would represent natural choices to study marine areas downwind of low-level passive degassing volcanoes. In particular it would be interesting to separate marine boundary-layer (MBL) and free-troposphere (FT) aerosols to understand how CCN

populations affect low-level and mid-level clouds. Current cloud retrievals have limitations to diagnose the evolution of the cloud droplet size distribution (e.g. its effective dispersion). The new generation of polarimeters (PACE SPEXone and 3MI) are quite promising in that respect. While such research avenues are promising, it was considered to be too early to go in that direction as PACE data are only becoming available now and 3MI is yet to be launched.

Instead, we focus the research objectives in STATISTICS on two under-studied natural analogues and three research topics that address critical gaps in our understanding and for which rapid progress can be made. For SAI, the project will revisit the Raikoke and Ulawun eruptions using different climate models to assess the evolution of aerosol size distributions under detailed microphysical processes and contrast it with observations. Preliminary work has shown that one model fails to reproduce the evolution of the aerosol size distribution In the MCB context, the project tackles the current paucity of observational constraints on aerosol properties and their interactions with clouds by focusing on the post-2018 Kilauea degassing. Only data for degassing episodes before 2018 have been considered in the literature. Leveraging TROPOMI-derived SO_2 dataset and the Volcplume service, aerosol retrievals will be performed using the GRASP algorithm to improve aerosol characterization. Furthermore, the project will investigate potential changes in cloud fraction using cloud masking products. For CCT and MCT, where the susceptibility of cirrus and mixed-phase clouds to intervention remains poorly constrained, the project will utilize newly available satellite-derived datasets of cloud microphysical properties. These data will be used to evaluate the fidelity of modelled cloud susceptibility and to quantify the associated uncertainty in negative radiative forcing, thereby contributing to a more robust assessment of the cooling potential of these techniques.

In addition, we will perform state-of-the-art radiative transfer calculations to quantify aerosol-radiation interactions, including heating rates and perturbations to surface and top-of-atmosphere (TOA) radiative fluxes. A novel contribution of the project is the integration of PV yield modelling, going beyond traditional PV indicators, to evaluate the impact of modified radiative fluxes on PV production and mitigate these effects through PV system design optimization. Finally, detectability studies will be conducted to assess the potential for observing SAI signals in the climate system with new observing systems.

The research gaps addressed by the STATISTICS project are shaded in grey in Tables 1.1 and 1.2. Likewise, the natural analogues that are being looked at are shaded in grey in Tables 1.7 and 1.8.

1.9 Analysis of potential risks and their impact on the products and project

The proposed research on Solar Radiation Modification (SRM) techniques – such as stratospheric aerosol injection (SAI), marine cloud brightening (MCB), and cirrus cloud thinning (CCT) – aims to bridge critical knowledge gaps and contribute to international assessments of SRM's uncertain potential as a climate intervention. The project faces some risks in regards to the achievement of its overall objectives.

Insufficient data utilization and resolution limitations

Existing observational data, including satellite datasets with resolutions of 100m-1km, remain under-utilized, while climate models often fail to resolve fine-scale processes critical to SRM (e.g., aerosol-cloud interactions near injection points). This risk could lead to incomplete or inaccurate assessments of SRM techniques if high-resolution modeling and synergistic data retrievals (e.g., via the GRASP algorithm) are not effectively integrated. Delays in accessing or processing these datasets within the project's short timeframe could further exacerbate this issue.

Uncertainty in natural and anthropogenic analogues

The project relies on analogues like passive volcanic degassing (e.g., Holuhraun 2014–2015) and shiptrack emissions to infer SRM effects. However, the project may find these analogues may not fully replicate SRM conditions, introducing uncertainty in extrapolating findings to intentional deployment scenarios. If discrepancies between analogues and SRM processes are not reconciled, the validity of resulting insights could be questioned, weakening the evidence base for international assessments.

Ethical and governance controversies

SRM remains highly controversial due to ethical concerns (e.g., unintended regional climate impacts in case of future deployment) and governance challenges (e.g., lack of comprehensive international frameworks). The project's exploration of field experiments and detectability assessments could inadvertently fuel public or political backlash, especially if perceived as endorsing deployment over mitigation. Failure to address these sensitivities transparently may limit stakeholder buy-in and hinder collaboration with policymakers and the broader scientific community.

Technical feasibility and scalability constraints

Assessing the energy budgets and scalability of SRM techniques (e.g., lofting aerosols for SAI or spraying sea particles for MCB) depends on realistic technological assumptions. Current technologies exhibit low efficiency, and the project's thermodynamic analyses may reveal impractical energy requirements or deployment

challenges. If these technical limitations are underestimated, the research could overstate SRM's viability, misguiding future efforts.

Collaboration and stakeholder alignment risks

The project's success hinges on coordination with ongoing initiatives (e.g., CCI, Horizon Europe projects like Co-CREATE and GENIE) and stakeholder engagement (e.g., via workshops). Misalignment or insufficient input from these groups could lead to duplicated efforts, overlooked gaps, or findings irrelevant to policy needs. Given the short project duration, delays in establishing these synergies could jeopardize the delivery of actionable outcomes.

Mitigating these risks requires prioritizing data integration, validating analogues rigorously, embedding ethical considerations, grounding technical analyses in current capabilities, and fostering robust collaboration and information exchange. By addressing these challenges, the project can strengthen its contribution to SRM research and climate action.

Chapter 2. Development methods, validation mechanisms and data pool description

This chapter describes the methods that are used, the validation mechanisms in place, the input datasets and the results obtained under the STATISTICS project.

2.1 Stratospheric Aerosol Injection (SAI) - WP2100/3100

2.1.1 Methods

Comparison with measurements taken after a volcanic eruption is currently the only way to validate the evolution of stratospheric sulfate aerosols in atmospheric and climate models. The most prominent of these eruptions was that of Mount Pinatubo in June 1991. This was also the largest eruption in the last 150 years. The observations following this eruption provide many opportunities for observation-model comparisons. However, the large sulfur emissions of about 16 Tg SO_2 within 3 hours is not comparable to SAI conditions. Here, injections of up to 10 Tg SO_2 per year are discussed. Since aerosol microphysics is non-linear and the final particle size depends strongly on the SO_2 concentration, smaller volcanic eruptions with an eruption height just reaching the stratosphere provide more realistic conditions to compare to SAI conditions. The Raikoke and Ulawun eruptions in 2019 were such eruptions. Wrana et al. (2023) extracted aerosol particle size information from satellite solar occultation measurements from the Stratospheric Aerosol and Gas Experiment III on the International Space Station (SAGE III/ISS) using a robust spectral method. They describe the particle size evolution as observed by SAGE III over several months and compare it with simulation results from ECHAM5-HAM. The observations showed a particle size reduction after the Ulawun eruption (triangle U in Figure 2.1.1) at an altitude of 18 km, which lasted for several months. The model also simulated this particle size reduction (2nd row in the figure), but the reduction lasted only two months. The reason for this discrepancy is still unclear. A comparison of different model results may help to better understand the post-eruption processes. This is important for SAI, as the differences may indicate poorly resolved processes in the model. We want to focus on a set of questions: What happens thereafter? Do other models show a longer period of small particles? Do the models miss processes?

We now describe the protocol for the model intercomparison conducted in WP2100 (see also Table 2.1.1 for a summary). Simulation starts in 2018 and includes the two Ambae eruptions in April and August to get the background sulfate concentrations right. The simulations include the Raikoke and two Ulawun eruptions in 2019. The model should be nudged to ERA5 data.

The model outputs are listed below. Column data include AOD at 550 & 825 nm. Data output on model-levels consist of extinction, effective radius, vertical profile of the heating rates by the sulfate aerosol, preferably calculated by a radiation double call, aerosol size distribution (wet radii, particle numbers). Nucleation and condensation rates are good as well. And, of course, the normal model output, especially meteorological variables needed for interpolation, e.g. temperature, pressure, surface pressure, geopotential height, specific humidity, U, V, W components of the wind.

Daily averages of extinction coefficient and effective radius, interpolated to fixed height levels [m]:
10000,10500,11000,11500,12000,12500,13000,13500,14000,14500,15000,15500,
16000,16500,17000,17500,18000,18500,19000,19500,20000,20500,21000,21500,
22000,22500,23000,23500,24000,24500,25000,25500,26000,26500,27000,27500,
28000,28500,29000,29500,30000,30500,31000,31500,32000,32500,33000,33500,
34000

The simulation period is from January 2018 to January 2020.
Timeline: finish runs by the end of May.

Table 2.1.1. Details on the Ambae, Raikoke and Ulawun eruptions.

Eruption	Lat/Lon	Start	End	SO2 mass [Tg]	Injection level	
Ambae	-15.4 S 167.83 E	6.4.2018 14 h 1.8.2018 14h	6.4.2018 18 h 1.8.2018 18 h	0.12 0.06	92 hPa 95 hPa	
Raikoke	48.29N 153.24 E	21.6.2019 18 h	22.6.2019 3 h	1.37	140 hPa	140-160 hPa
Ulawun	-5.05 S 151.33 E	26.6.2019 4.30h 3.8.2019 9.30h	26.6.2019 7.30h 3.8.2019 11.30h	0.14 0.3	100 hPa 90 hPa	100 – 120 hPa 90 – 110 hPa

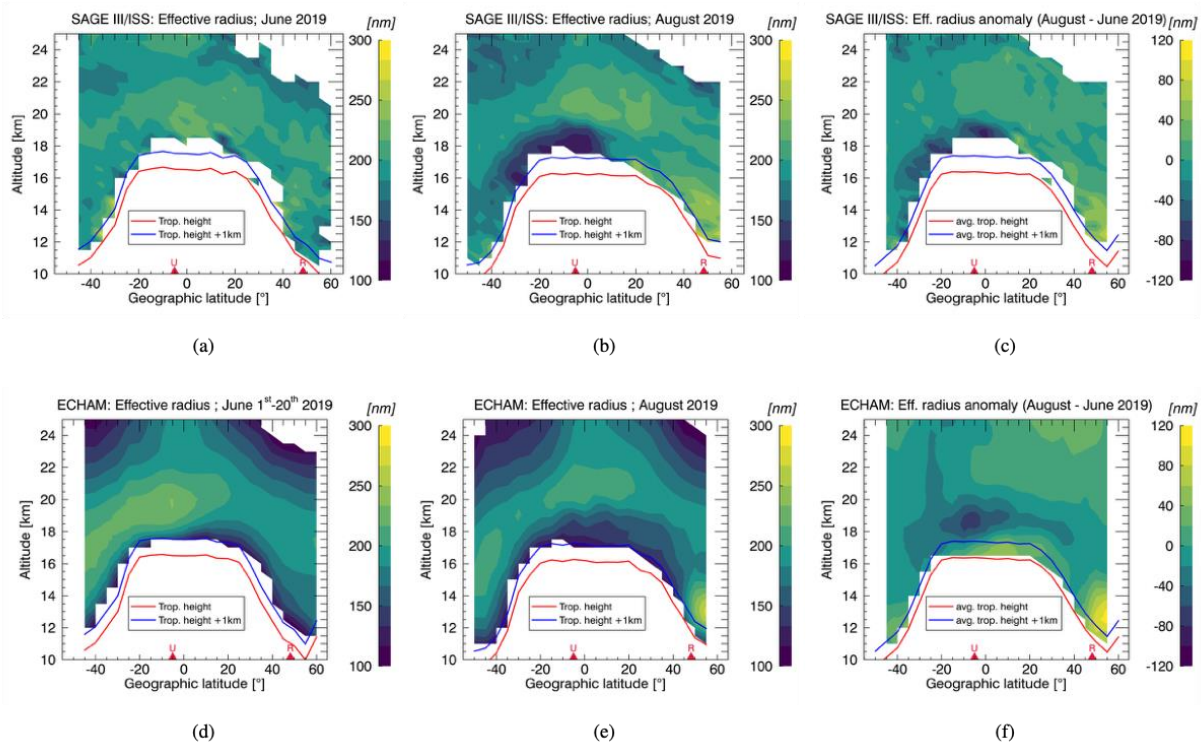

Figure 2.1.1. Zonal means of the effective radius (a–c) retrieved from SAGE III/ISS and (d–f) calculated with the ECHAM model using the spatial and temporal sampling of SAGE III/ISS for (a, d) 1 to 20 June and (b, e) August 2019. Panels (c) and (f) show the temporal anomaly of the effective radius, i.e., the difference between the first two plots in each row. Triangles and letters on the bottom of each plot indicate the locations of the Ulawun (U) and Raikoke (R) volcano. Tropopause height is illustrated by a red line, with the blue line indicating an uncertainty interval of 1 km above the tropopause height. Figure is taken from Wrana et al. (2023).

2.1.2 Retrieval uncertainty of the effective radius data

Intercomparison of models requires reliable reference data, especially for such small events like Ulawun and Raikoke. To retrieve the aerosol size distribution data and to verify the results of Wrana et al. (2023), we used the approach of Jörimann et al. (2025). SAGE III provides aerosol extinction coefficients on up to 9 wavelength bands. From these data, a unimodal log-normal aerosol size distribution with three free parameters was derived by iteratively checking the error between theoretical and measured extinction coefficients for the entire realistic parameter space and selecting the best-fitting parameter. However, not all wavelengths are of sufficient quality for the size distribution retrievals and their inclusion can worsen the bias of the “good” bands. Figure 2.1.2 shows the effective radius retrieved from the SAGE III data using all 9 bands, band #7, and only the 6 best-fit ones, following the wavelength quality criteria analysis as described in Jörimann et al. (2025). Although the inclusion of all wavelengths introduces some uncertainty to the retrievals in

the upper part of the Junge layer, in its lower part the agreement is quite good and all three cases reveal the features discovered by Wrana et al. (2023), namely, a decrease of aerosol effective radius and southward transport following the Ulawun eruption and an increase and equatorward transport after the high-latitude Raikoke eruption.

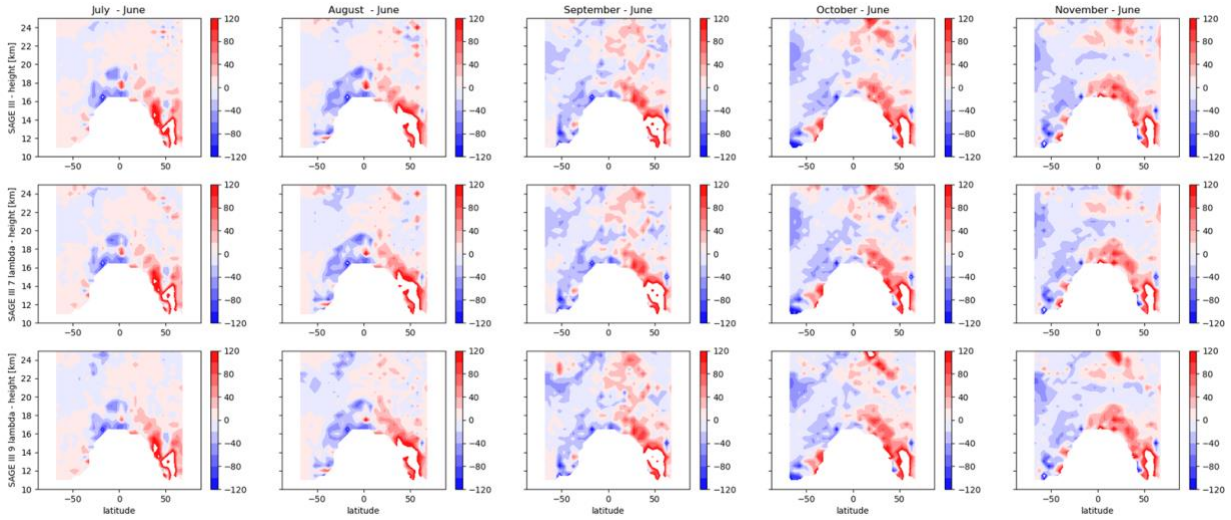

Figure 2.1.2. Zonal means of the change in effective radius relative to June for different choices of wavebands (from top to bottom).

2.1.3 Model intercomparison for Raikoke and Ulawun eruptions

Four different models performed the simulations described in Section 2.1.1: SOCOL, ECHAM5-HAM (Niemeier and Timmreck, 2015), NorESM, and IPSL-ESM (Kleinschmitt et al, 2017). All of the models included aerosol microphysics, such as nucleation, condensation, coagulation, and sedimentation processes. However, the oxidation of SO_2 to H_2SO_4 is treated differently, as some models include detailed chemical processes (e.g., SOCOL), while others use a reduced chemical scheme with prescribed concentrations of precursors, such as OH and NO_x (e.g., ECHAM5-HAM and IPSL-ESM). NorESM has so far mainly been used for tropospheric studies and is in a test phase for stratospheric applications of the aerosol microphysics. We include the model here even though the results may not be perfect. However, they provide additional information.

We compared the simulated effective radii (Figure 2.1.3) and the extinction coefficient (Figure 2.1.4). All models started the simulation in 2018 with the eruption of the Ambae volcano. Including this eruption is important to achieve a reasonable sulfate background concentration. However, the models show quite some differences between the simulated background radii and concentrations in June, with only ECHAM-HAM and NorESM showing an area with increased particle size in the tropics. SOCOL simulates relatively small particle sizes in June and shows small particle sizes for the other months as well.

The observations show a decrease in particle size in the southern hemisphere's lower stratosphere in August (see Fig. 2.1.3, third column). This decrease is due to increased nucleation following the eruption of the Ulawun volcano (Wrana et al, 2023). In the Northern Hemisphere, particle size increased compared to June due to the Raikoke eruption. Raikoke is located at higher latitudes where higher temperatures in the lower stratosphere result in less frequent nucleation. The separation in increasing particle size in the northern hemisphere and decreasing particle size in the southern hemisphere remains in the following months (see Fig. 2.1.2), but the area of decreasing particle size moves southward and decreases over time.

The models simulate the feature of decreasing particle size in August well, with less separation between the northern and southern hemispheres (Fig 2.1.3). ECHAM-HAM (first row) shows the strongest reduction in particle size, with the minimum occurring close to the location of the Ulawun eruption. The other models also simulate particle reduction, but it is mostly spread throughout the tropics. The reason for the strong reduction in particle size in higher northern latitudes in the IPSL-ESM model is unclear.

In November, observations still show very small particles at 15 km altitudes in the Southern Hemisphere. However, this is not reproduced well by the models, but most models do simulate smaller particles in November at higher southern latitudes compared to June, especially SOCOL (second row).

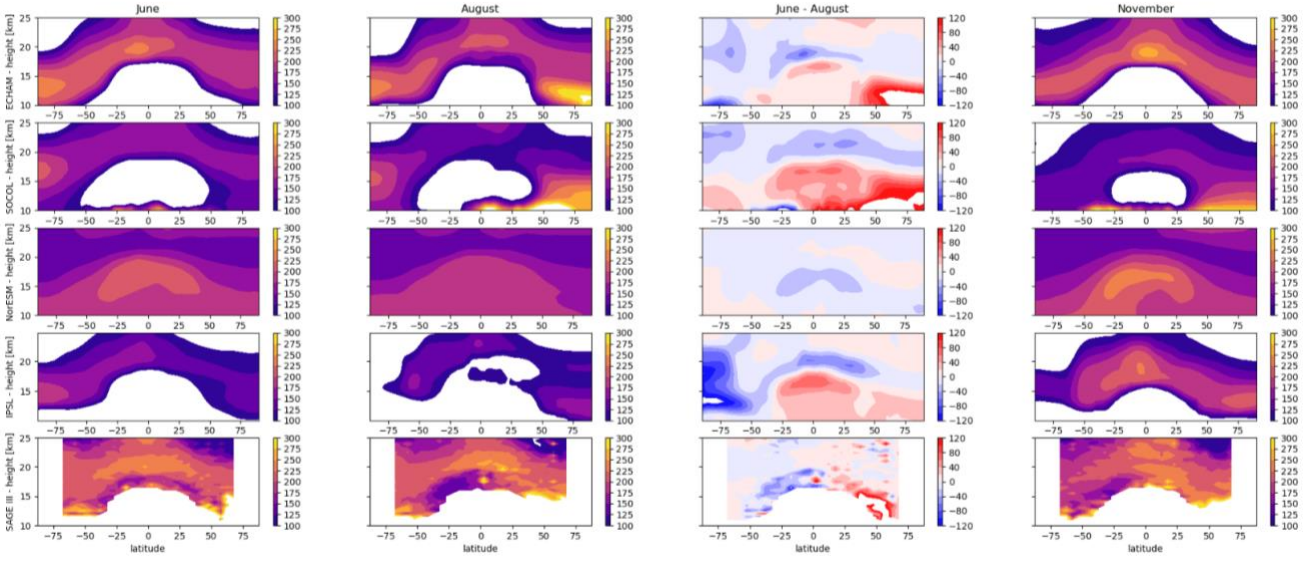

Figure 2.1.3. Zonal means of the monthly averaged effective radius (nm) for four models (ECHAM-HAM, 1st row; SOCOL, 2nd row; NorESM, 3rd row; IPSL-ESM, 4th row) and SAGE III observations (last row) for the months June, August and November and the anomaly between June and August. All models simulated the Raikoke and the two Ulawun eruptions.

Simulated extinctions show that the impact of the Raikoke eruption is overestimated in ECHAM-HAM and SOCOL. The elevated extinctions caused by the Ulawun eruption in the tropics are simulated quite well in all models. Either NorESM misses the Raikoke eruption, or particle growth and the meridional transport to the poles is very strong, causing the sulfate particles to vanish quickly. IPSL-ESM most closely matches the observations for July and August. The simulated extinction fits quite well. However, the subsequent decrease in elevated extinction is slower than observed. Furthermore, IPSL-ESM shows the greatest extinction in November.

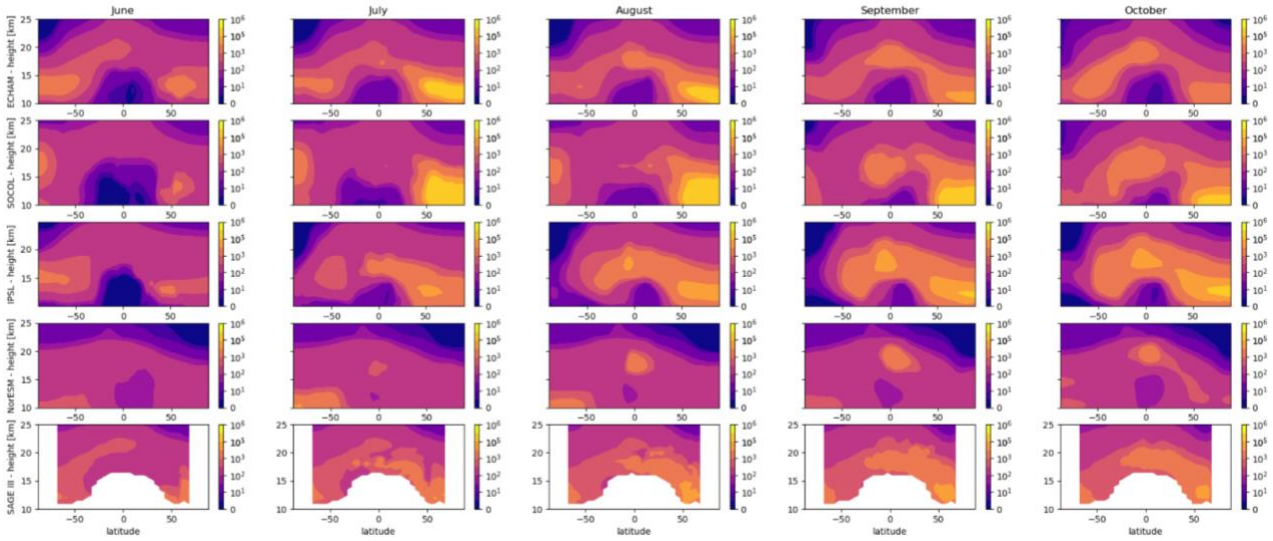

Figure 2.1.4. Zonal means of the monthly averaged extinction for four models (ECHAM-HAM, 1st row; SOCOL, 2nd row; IPSL-ESM, 3rd row; NorESM, 4th row) and SAGE observations (last row) for the months June, August and November and the anomaly between June and August. All models simulated the Raikoke and the two Ulawun eruptions.

2.1.4 Discussion and summary of the results

As mentioned earlier, nucleation is the primary process responsible for forming small particles after the Ulawun eruption. Nucleation is stronger at lower temperatures. The Ulawun eruption emitted sulfur dioxide (SO_2) into the lower tropical stratosphere; the Raikoke eruption emitted it into the mid-latitudes. The lower stratosphere is coldest at the winter poles and in the tropics. Therefore, we observe the formation of small particles following the eruption of Ulawun but not after the eruption of Raikoke. All four models reproduce this feature. However, the location, strength, and duration of the occurrence of smaller particles differ between the models and deviate from the observations. ECHAM-HAM and IPSL show the strongest reduction in particle size in the tropics. Additionally, both models show a significant decrease in size at the southern hemisphere's winter pole.

ECHAM-HAM is the only model that captures the north-south distribution of particle size to some extent. The models tend to simulate a vertical distribution of the anomaly, with an increase in particle size near the tropopause and an additional increase above it. SOCOL is the only model that clearly simulates small particles in November. The other models calculated an increase in particle size.

The reasons for these differences are not currently well understood. Aerosol microphysics, particle formation, and resulting particle sizes are complex, nonlinear processes. Particle size depends not only on nucleation but also on the amount of sulfuric acid available for condensation processes and on the particle size distribution, which is important for coagulation processes. In ECHAM-HAM, particles begin to grow due to coagulation when the nucleation rate declines due to insufficient sulfuric acid or the volcanic cloud rising in altitude. In the latter case, the volcanic cloud reaches warmer layers, and nucleation becomes less effective.

Another possible reason for the differences between the models is the nucleation parameterization. Figure 2.1.5 shows the results simulated with ECHAM-HAM for two different parameterizations. Vehkamäki et al. (2002) developed the parameterization used in many aerosol microphysical models. Määttänen et al. (2018) updated this parameterization for larger parameter ranges (such as very low temperatures) and included particle collision (kinetic or barrierless nucleation) as a separate nucleation process under high sulfur loads. Thus, it is important when simulating volcanic eruptions. The Määttänen et al. (2018) parameterization shows smaller particles in the tropical lower stratosphere in August and less particle growth in September. This parameterization is included in ECHAM-HAM and the IPSL-CM models, which simulate the strongest particle size reduction.

Other details of particle formation simulations in different models can also play an important role. For example, the handling of operator splitting can be significant (Vattioni et al., 2024). In ECHAM-HAM, time integration is solved independently of operator splitting (Kokkola et al., 2009). These differences impact the amount of sulfuric acid available for nucleation and condensation, which affects the final particle size.

These examples show the complexity of particle formation. To better understand the differences between the models, more details need to be examined. We raised a few questions in Section 2.1.1: Do other models show a longer period of small particles? Do the models miss processes?

ECHAM-HAM and IPSL-CM both simulate a relatively short period of reduced particle sizes after the Ulawun eruption. NorESM shows a very low impact of the eruptions. Thus,

the model has other issues to resolve before a good comparison is possible. However, SOCOL shows a long lifetime of small particle sizes, making it closer to the observations than the other models in this aspect. This model does not include a different process of particle formation. Therefore, we cannot assume missing processes are the reason for the discrepancies with the observations.

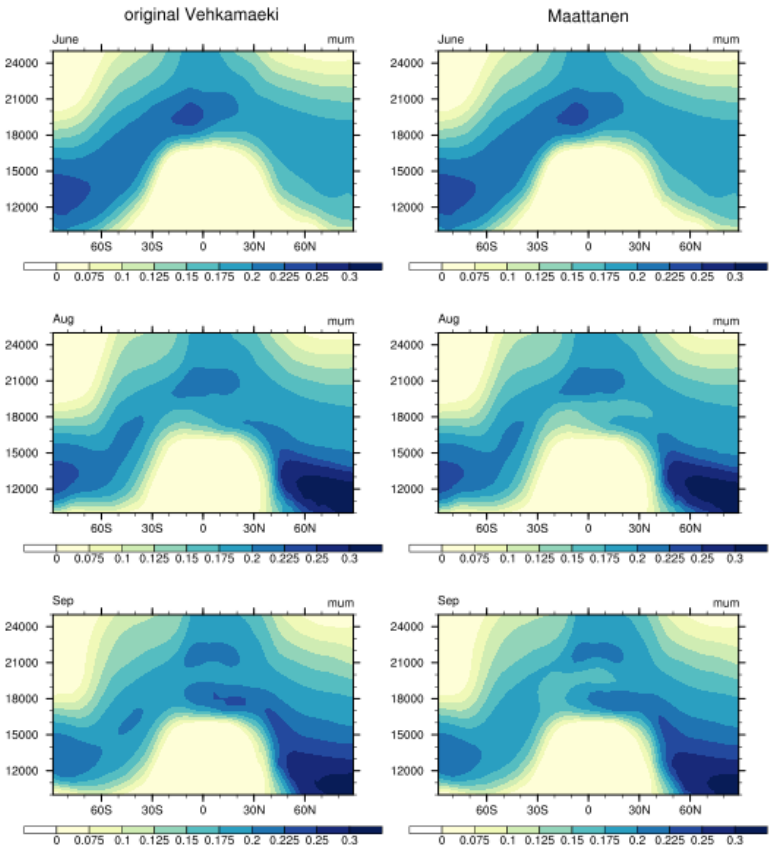

Figure 2.1.5. Zonal means of the monthly averaged effective radius (μm) simulated with two different nucleation parameterizations within ECHAM-HAM. Left: Nucleation parameterization after Vehkamäki et al. (2002). Right: after Määttänen et al. (2018).

2.2 Marine Cloud Brightening (MCB) - WP2200/3200

2.2.1 Methods

As discussed in Chapter 1, the Kilauea volcano eruption represents a very promising case study of MCB using satellite data before, during and after the volcano eruption. This includes:

1. SO_2 estimates from the S5P/TROPOMI.
2. Aerosol retrieval from GRASP algorithm applied to synergy of the S3/OLCI and S5P/TROPOMI

3. Cloud statistics (cloud fraction and cloud reflectivity) derived from the Aerosol Cloud Obstruction Mask (ACOM), applied to the S3/OLCI measurements with native (~300 m) resolution.

Figure 2.2.1 shows SO_2 emission from the Kilauea volcano, derived from TROPPOMI measurements (https://volcplume.aeris-data.fr, https://so2.gsfc.nasa.gov). Substantial increases in SO_2 emissions are well observed during the June-July period in 2018.

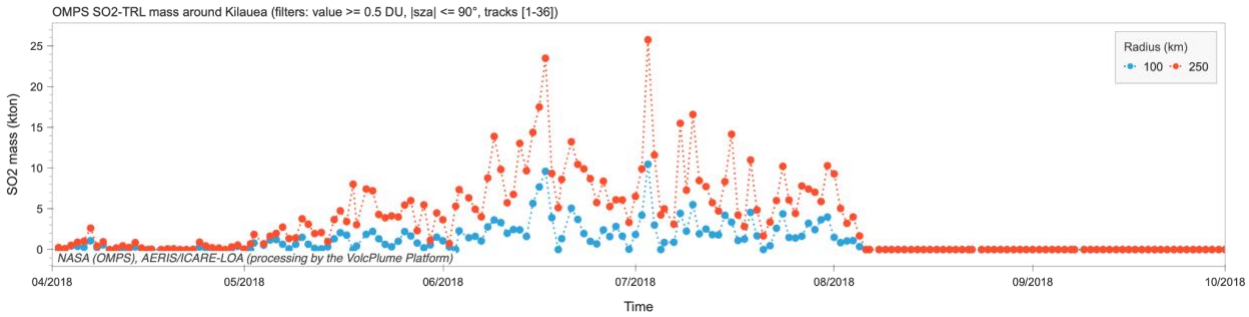

Figure 2.2.1. SO_2 emission from the Kilauea volcano in 2018.

To better characterize the timing and intensity of SO_2 emissions from the passive degassing of the Kilauea volcano, we will compile and visualize five years of satellite retrievals (2020-2025) to diagnose SO_2 burden over disks around Kilauea.

Investigation of aerosol-cloud interaction and the aerosol effect on cloud brightening requires knowledge of the extended aerosol properties, e.g., aerosol chemical composition, size, hygroscopic properties. In general, globally, this information can be obtained only from space-borne multi-angular-polarimetric measurements. Currently, there is still a big gap in such measurements since the end of the PARASOL mission in 2013. The new generation of polarimeters launched in 2024 (PACE/HARP-2 and PACE/SPEXone) do not provide long time series measurements yet, which are required for the MCB studies. Therefore, in this project, the advanced GRASP retrieval from the synergy of different single-angle space-borne optical sensors (SYREMIS/GRASP approach, Litvinov at al., 2025) will be used to study aerosol effect on the MCB. Such advanced retrieval includes the following aerosol extended optical properties as spectral Aerosol Optical Depth (AOD), Angström Exponent (AE) and Single Scattering Albedo (SSA), as well as volume column concertation of the main 4 aerosol species: Biomass Burning (BB), Sulphate-like (SU) aerosol, Sea Salt and Dust. These parameters define the aerosol type information and hygroscopic properties required for aerosol-cloud interaction and, as a result, for MCB studies.

2.2.2 Aerosol retrieval from GRASP/OLCI

Figures 2.2.2 to 2.2.4 show monthly mean aerosol properties (Aerosol Optical Depth (AOD), Angström Exponent (AE), and Single Scattering Albedo (SSA)) for four months in 2018 (June-September) derived from the GRASP/OLCI retrieval over the Kilauea area.

Volcanic aerosol plume is well seen as high AOD cases on the West from the volcano (the area in the red rectangle in Fig. 2.2.2). The area to the East from the volcano is almost not affected by the volcano eruption (the area in the yellow rectangle in Fig. 2.2.2). As one can see, in June 2018 AOD of the volcanic plume was the highest, decreased in July-August 2018, and almost reached background value in September 2018 (Fig. 2.2.2). Similar spatial distribution and the temporal variability is also observed for other aerosol characteristics AE and SSA in Figs. 2.2.3 and 2.2.4.

Figures 2.2.2 to 2.2.4 show strong variability of AOD, AE and SSA depending on the distance to the volcano. In particular, one can observe high AOD cases at the West part of the aerosol plume at a quite big distance from the volcano. This high AOD spot at the west edge of the plume shows large AE with values ~2 (indicative of small particles) and large SSA with values ~1. This may be the results of the gas-to-particle transformation which should be accounted for in MCB studies.

The asymmetry in the West-East spatial distribution of aerosol properties, and the temporal dependence of aerosol properties correlate with SO_2 emission estimates from the Kilauea volcano (e.g., Fig. 2.2.1). Similar West-East asymmetry and the temporal variability in cloud properties have been analysed to investigate the aerosol-cloud interaction and MCB effect in this project.

Overall, Figs. 2.2.1 to 2.2.4 show the importance of accounting for SO_2 emission estimates, aerosol properties and cloud statistical information for MCB studies.

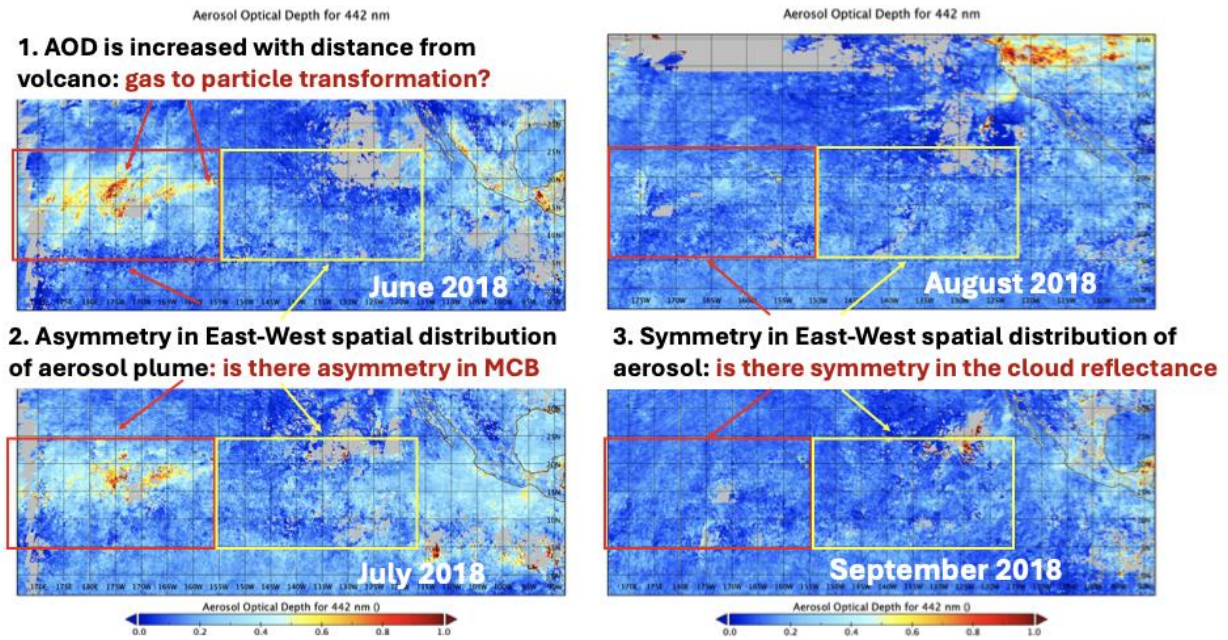

Figure 2.2.2. AOD from GRASP/OLCI retrieval over the Pacific Ocean in June-September 2018.

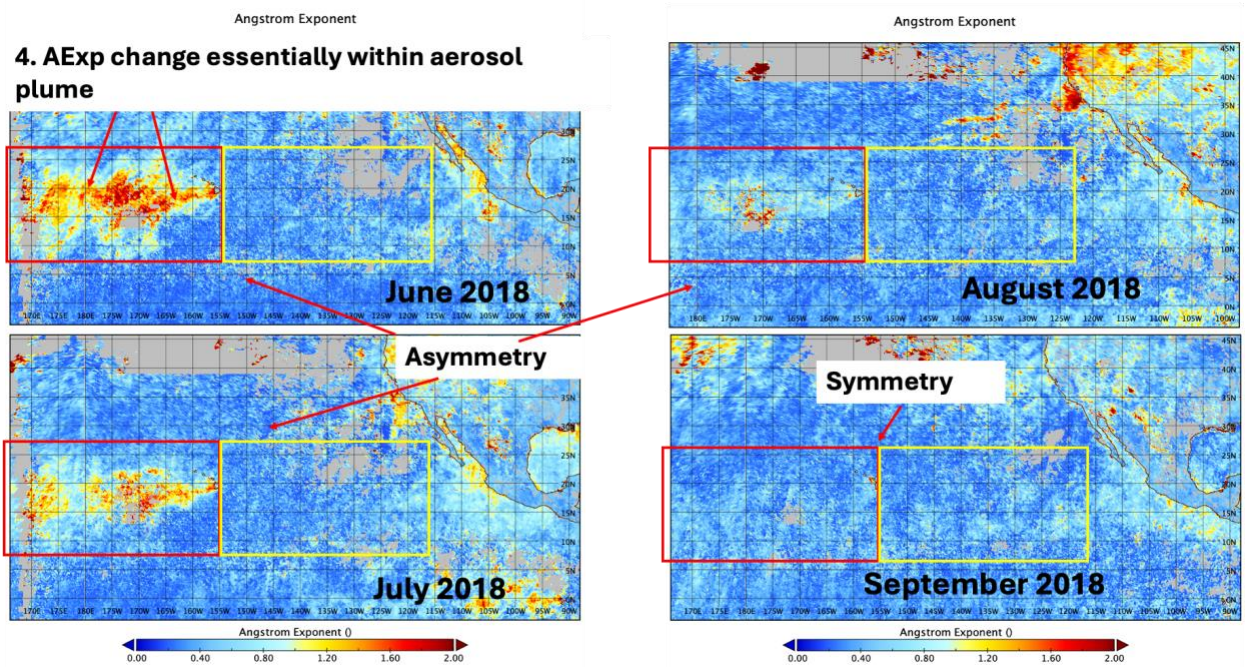

Figure 2.2.3. AE from GRASP/OLCI retrieval over the Pacific Ocean in June-September 2018.

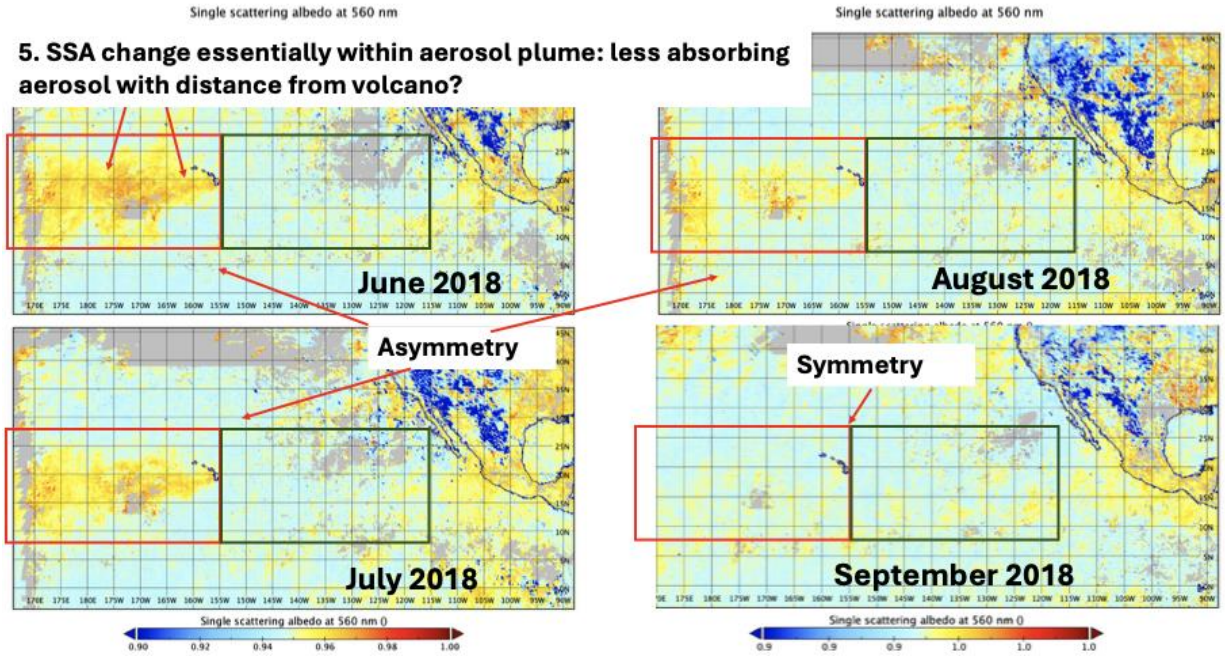

Figure 2.2.4. SSA from GRASP/OLCI retrieval over the Pacific Ocean in June-September 2018.

2.2.3 Aerosol retrieval using SYREMIS/GRASP synergetic approach

To improve the characterization of volcanic aerosols, we applied the Synergetic retrieval from muti-mission spaceborne measurements SYREMIS/GRASP approach to combined Sentinel-3/OLCI and Sentinel-5P/TROPOMI observations over the Kīlauea region for June–September 2018 (during the eruption) and 2019 (after the eruption). The synergy enables improvement of the retrievals of aerosol optical depth (AOD), Ångström exponent (AE), single scattering albedo (SSA), and aerosol species column volume concentration. OLCI and TROPOMI orbits cross the Kīlauea region at approximately 21 UTC and 00 UTC, respectively, and are merged into a single daily map to provide enhanced spatial coverage of the volcanic plume.

Figure 2.2.5 presents daily mean AOD at 560 nm derived from the OLCI+TROPOMI SYREMIS/GRASP synergy. As one can see AOD is markedly elevated in the plume region, with peak values downwind of the volcano.

Figure 2.2.6 displays the retrieved Ångström exponent (AE). Values are close to 2 across large parts of the plume, indicating a strong fine-mode contribution typical of volcanic sulfate aerosols. In some areas further from the source, AE increases, which, as it was already mentioned before, can be due to the secondary particle formation (gas-to-particle transformation).

Figure 2.2.7 shows the single scattering albedo (SSA) at 440 nm. The retrieved values are close to unity, indicating that the volcanic aerosols are predominantly non-absorbing.

Overall, AE and SSA values point to small particles of a sulfate-rich composition, rather than ash or carbonaceous particles, which are relevant natural analogs for studying aerosol–cloud interactions in the context of Marine Cloud Brightening.

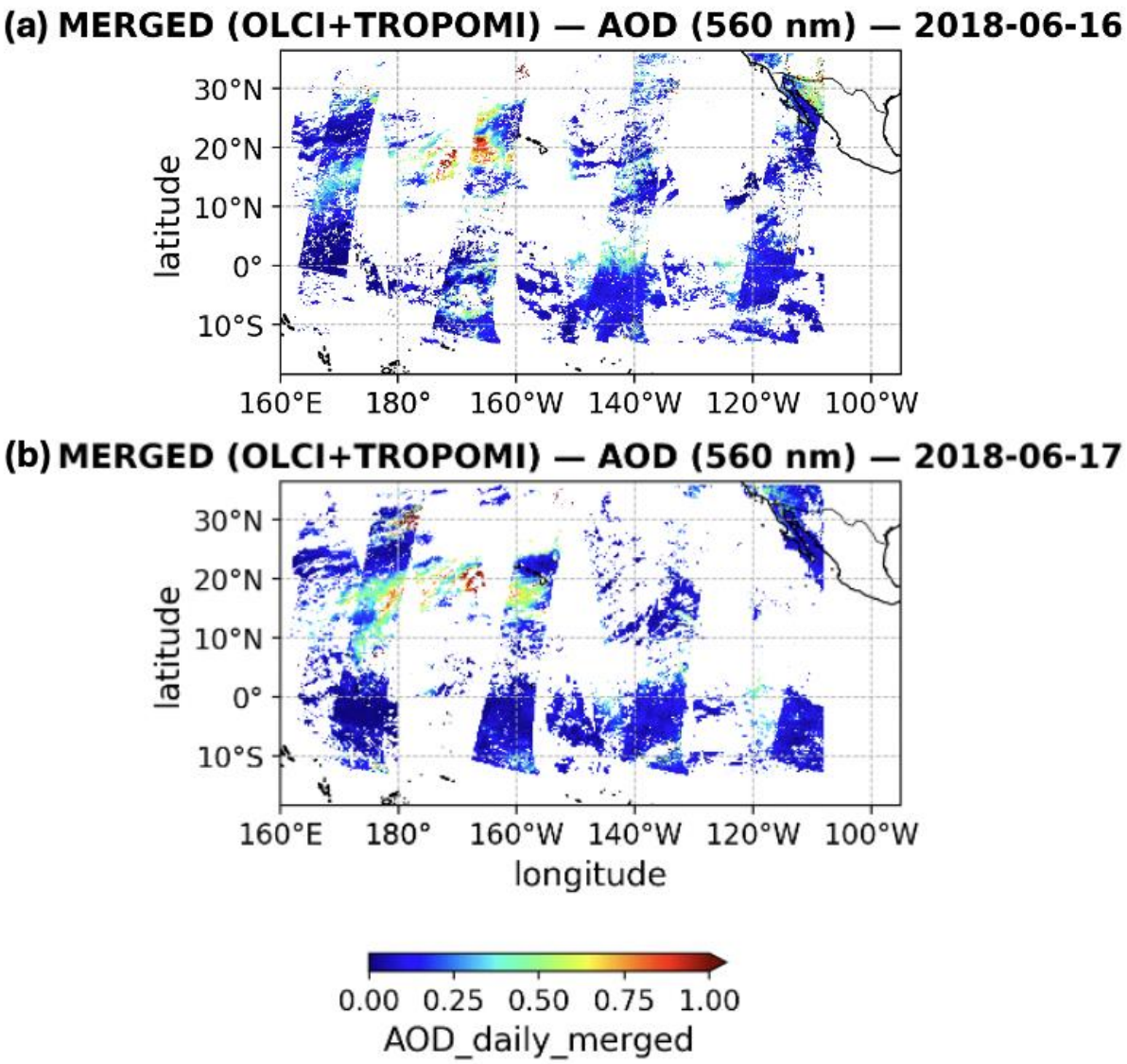

Figure 2.2.5. Daily mean aerosol optical depth (AOD, 560 nm) retrieved with SYREMIS/GRASP OLCI+TROPOMI synergy on (a) 16 June 2018 and (b) 17 June 2018.

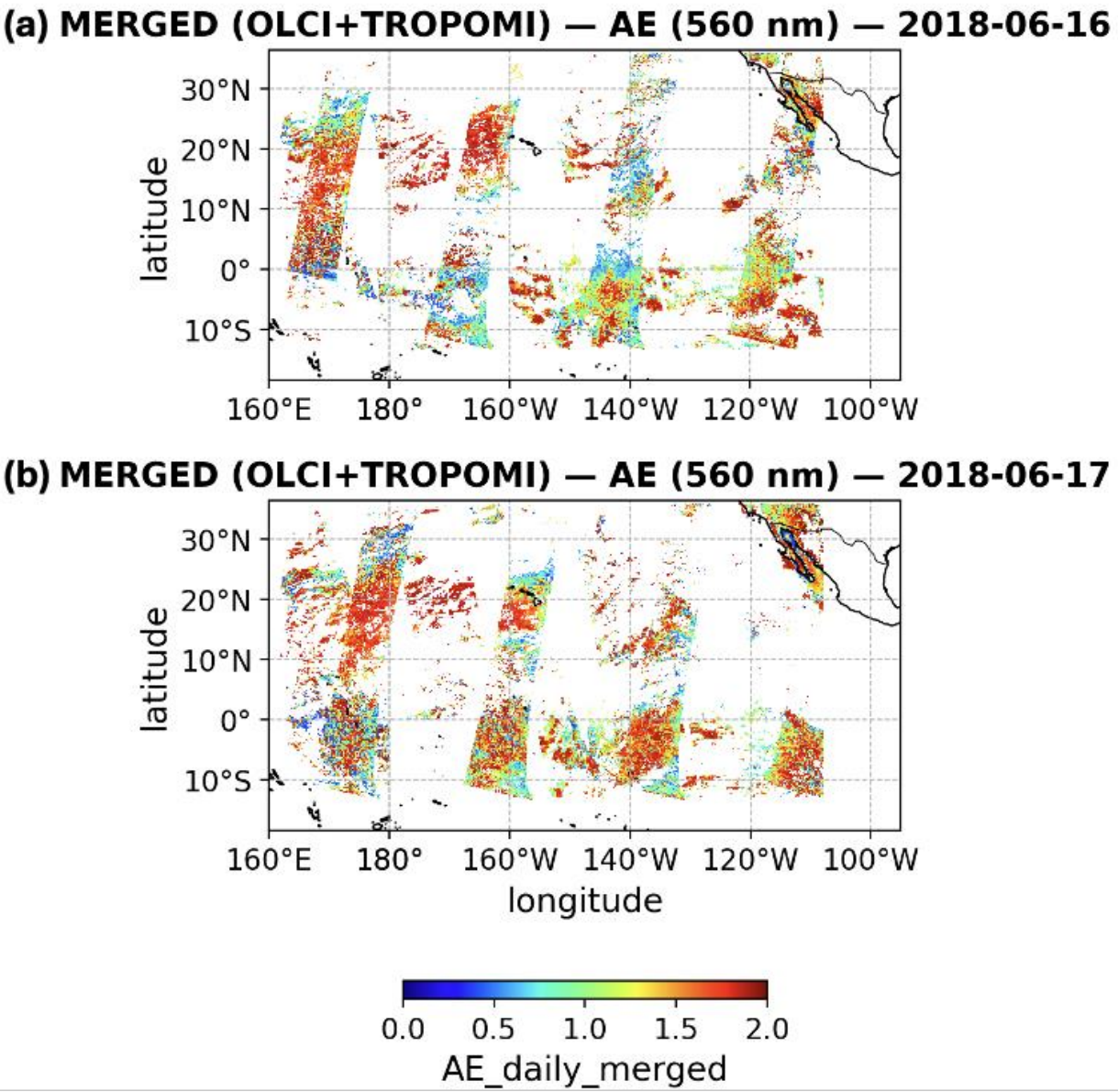

Figure 2.2.6. Daily mean Ångström exponent (AE, 560 nm) from SYREMIS/GRASP OLCI+TROPOMI synergy on (a) 16 June 2018 and (b) 17 June 2018. AE values approach 2, indicating fine-mode dominance consistent with volcanic sulfate aerosols.

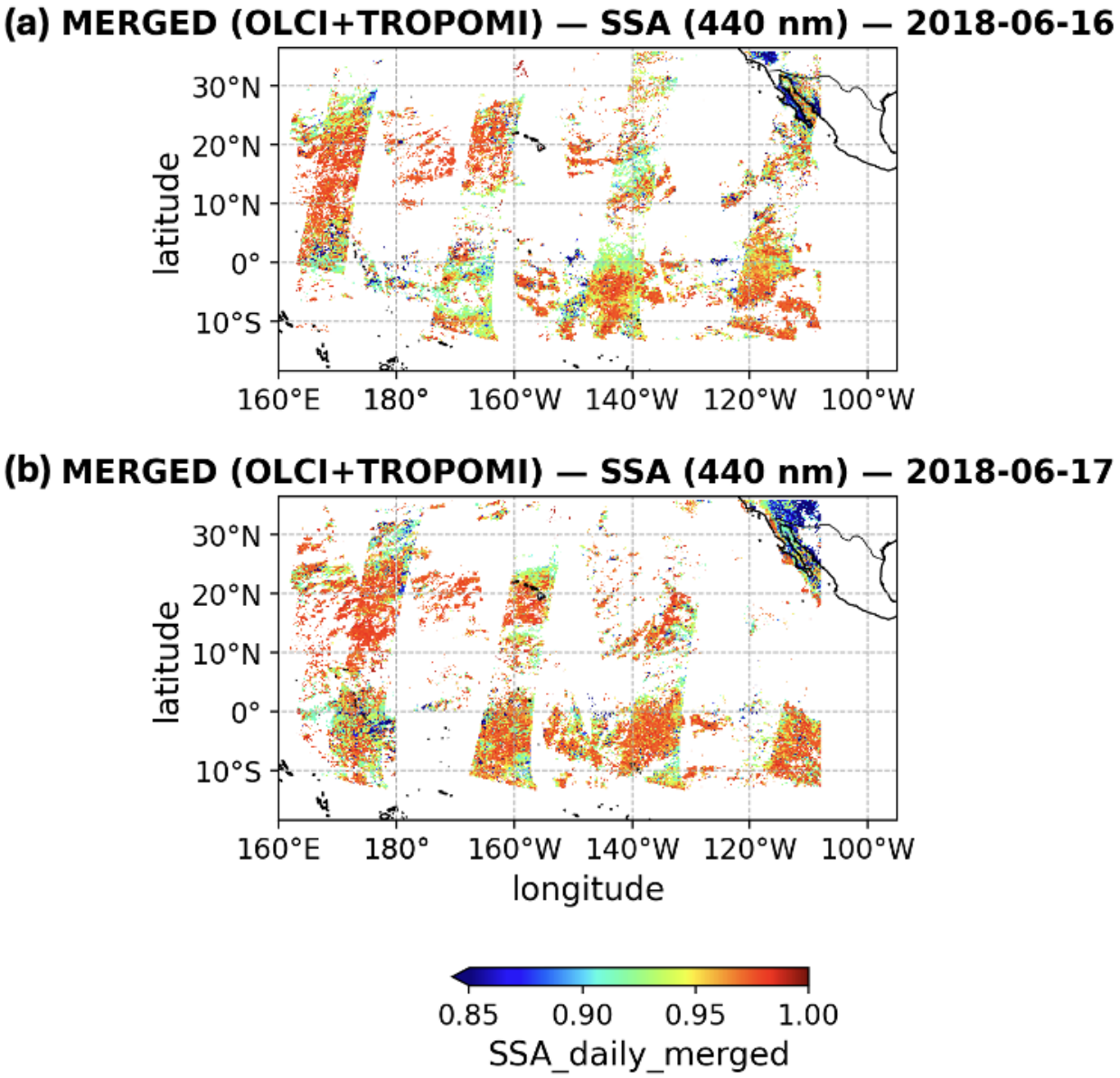

Figure 2.2.7. Daily mean single scattering albedo (SSA, 440 nm) from SYREMIS/GRASP OLCI+TROPOMI synergy on (a) 16 June 2018 and (b) 17 June 2018. Values near unity confirm that the plume consists of largely non-absorbing particles.

2.2.4 Cloud statistics method

The following cloud statistics have been used in MCB analysis for Kilauea volcano case: (i) cloud cover conditions (percentage of the cloudy pixels or number of cloudy pixels within the areas) and (ii) cloud reflectivity properties (cloud reflectance at 412 nm and 865 nm). Such statistics is derived from Aerosol Cloud Obstruction Mask (ACOM) (Litvinov et al., 2024) applied to OLCI measurements with native (~300 m) resolution over the Kilauea area. Figure 2.2.8 shows an example of ACOM aerosol and cloud classification for OLCI-A measurements over Kilauea volcano on 5 May 2018. Red and orange colors in Fig.

2.2.8 correspond to optically thick and moderate clouds. Figure 2.2.9 shows the top of atmosphere (TOA) reflectance from the OLCI-A measurements on 5 May 2018. Assigning OLCI-A TOA reflectance with the ACOM cloud mask classification, the cloud statistics (i) and (ii) has been analysed for the “West” and “East” regions specified in Figs. 2.2.2 to 2.2.4 to investigate possible tropospheric aerosol effect on MCB. The temporal changes in the cloud statistics due to interaction with aerosol, will be considered by applying ACOM mask to OLCI measurements over the Kilauea volcano area for the period June-September 2017 (before the volcano eruption), 2018 (during the volcano eruption) and 2019 (after the volcano eruption).

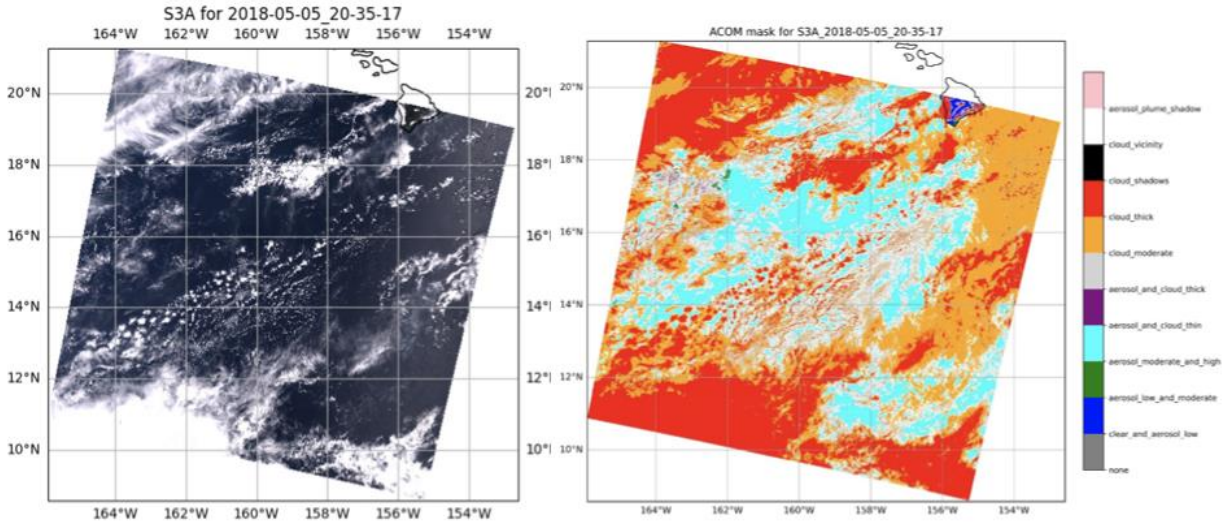

Figure 2.2.8. RGB OLCI-A image and ACOM mask aerosol/cloud classes over the Kilauea area on 5 May 2018.

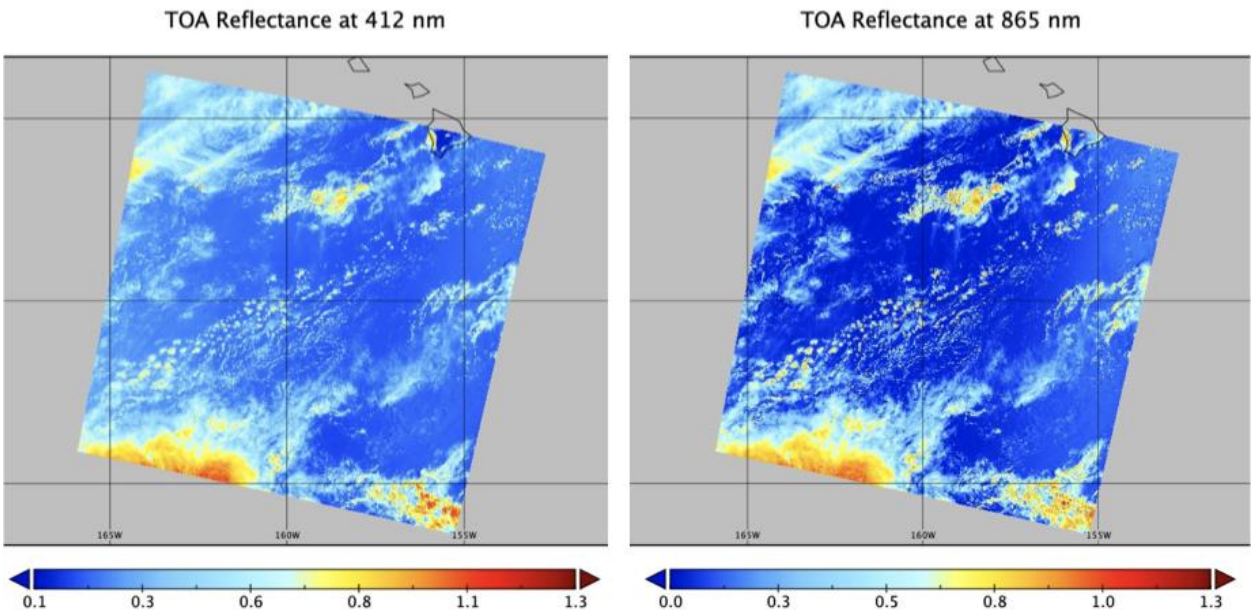

Figure 2.2.9. TOA reflectance from OLCI-A over the Kilauea area, 5 May 2018.

Statistical analysis of cloud reflective properties over the Kilauea volcano area is complicated by the strong dependence of the cloud reflectance on the sun and satellite geometries: zenith and azimuth angles. Figure 2.2.10 shows an example of the geometry variability within OLCI-A orbits.

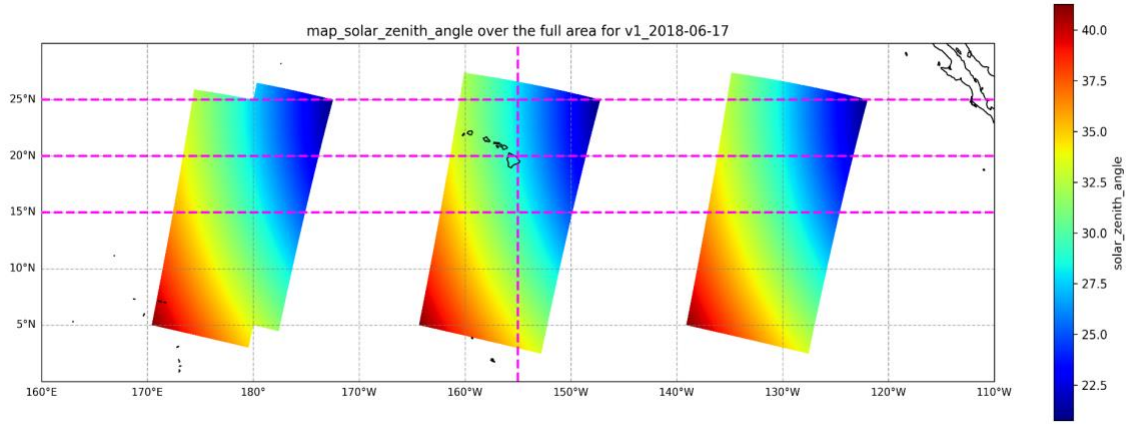

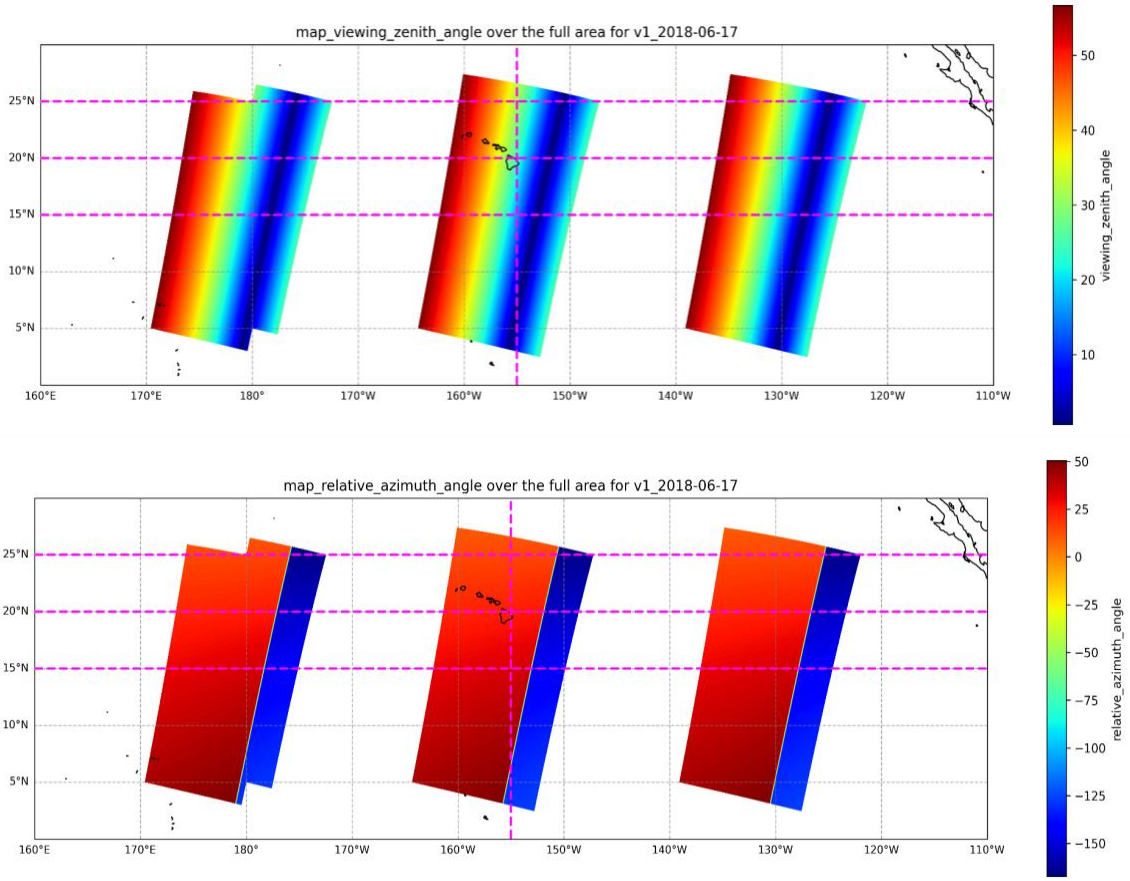

Figure 2.2.10. (top panel) Solar Zenith Angle (SZA), (middle panel) Viewing Zenith Angle (VZA) and (bottom panel) azimuth angle difference (satellite-Sun) within OLCI orbits over the Kilauea volcano area. June 17, 2018.

Therefore, to investigate MCB using OLCI-A measurements the geometry effect should be removed or considerably reduced. For these purposes the statistical properties of the clouds are considered independently in the subregions with the following discretizations of the observation and illumination geometries:
i. Azimuth angle ranges (k = 1... N_{azim}): Azimut_difference >0 and Azimut_difference <0
ii. SZA and VZA ranges (i = 1..N_{sol} ; j = 1..N_{obs}): 0-20°, 20-30°, 30-40°, 40-50°, 50-60°

Such discretization gives 50 geometry subsets. Nevertheless, as seen from Fig. 2.2.10, not all of them may contain OLCI measurements. Figure 2.2.11 shows 12 subregions out of 50 which contain OLCI measurements over the Kilauea volcano area. Moreover, for statistical analysis we selected only the subregions containing enough measurements to perform statistical analysis. An example of such subregions, with the number of OLCI measurements indicated inside, is presented in Fig. 2.2.12.

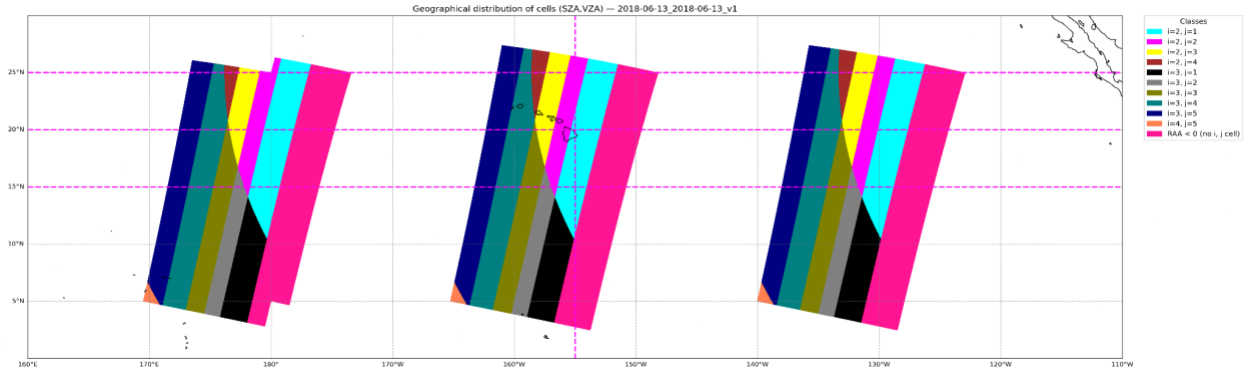

Figure 2.2.11. Sun/Observation subregions for OLCI measurements over Kilauea volcano area.

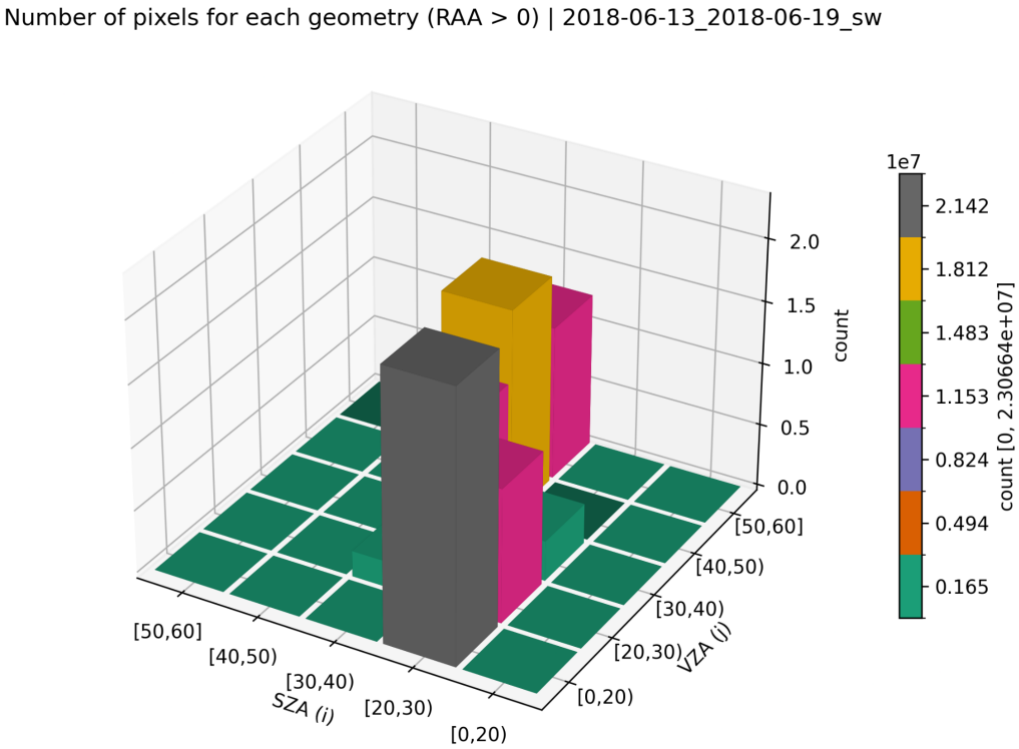

Figure 2.2.12. Number of OLCI measurements in the Sun/Observation subregions.

Figures 2.2.10 and 2.2.11 show periodic variations of the Sun/Observation geometry on the West and East from the Kilauea volcano. Taking into account the asymmetry in the aerosol plume and its geographical distribution (Figs. 2.2.2 to 2.2.7), the statistical analysis in each Sun/Observation subregions is performed in four geographical regions:

1. North-West (NW): 20°N < latitude < 25°N and longitude > 155°W
2. South-West (SW): 15°N < latitude <= 20°N, longitude > 155°W
3. North-East (NE): 20°N < latitude < 25°N, longitude < 155°W

4. South-East (SE): 15°N < latitude <= 20°N, longitude < 155°W

Beside the observation/illumination geometry, cloud reflectance depends strongly on the size of water droplets as well as optical thickness of the clouds in vertical and horizontal directions. Aerosol particles can serve as cloud condensation nuclear resulting in changing the size of the cloud droplets and, thus, affecting cloud reflectivity. To investigate MCB due to the aerosol effect, we used only “optically thick” (COD>7 (Cloud Optical Depth)) and “moderate” (3<COD<7) clouds in our analysis (cloud class “6” and “7” in orange and red color in Fig. 2.2.8).

Figure 2.2.13 and 2.2.14 show typical OLCI measurements and ACOM aerosol and cloud classes within the four geographical zones used in these studies.

Figure 2.2.13. OLCI orbits and measured TOA reflectance at 412nm.

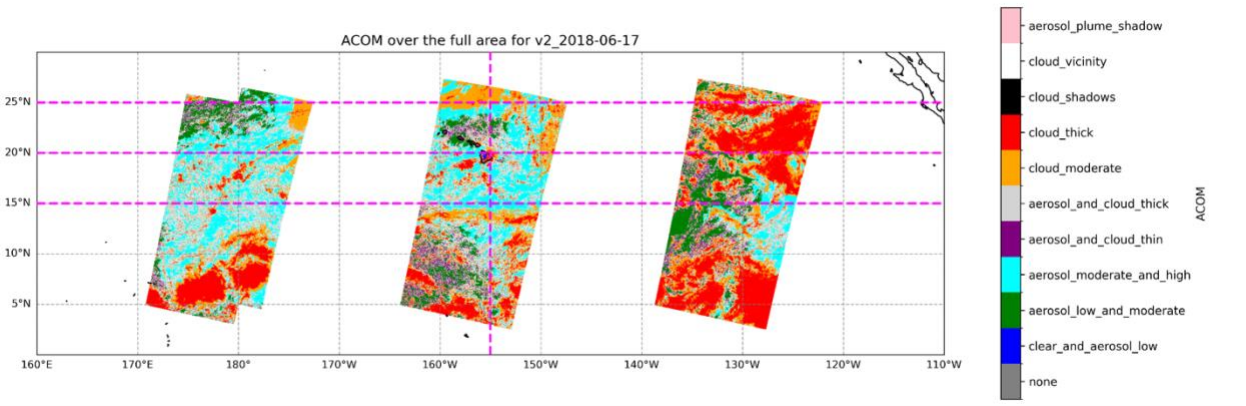

Figure 2.2.14. ACOM mask aerosol and cloud classes for OLCI measurements.

The analysis is based on statistical properties of the TOA reflectance (*I*) measured by OLCI at 412 and 865 nm as well as on the cloudy conditions (e.g., number of cloudy pixels). In particular, for each of the four geographical regions and the Probability Density Function (PDF) of I(412nm) and I(865nm) was built for pixels classified as “cloud thick”

and “moderate” by the ACOM mask. These PDFs were obtained as for each illumination/observation sub-regions (Fig.2.2.11), as for all illumination/observation subregions but separately for 4 geographical zones: NW, SW, NE, and SE. The following characteristics were considered: (i) average value of I(412nm) and I(865nm) for each illumination/observation subregions; (ii) average value of I(412nm) and I(865nm) for all subregions but for 4 zones; (iii) minimum and maximum value of I(412nm) and I(865nm); (iv) number of cloudy pixels in each subregion and geographical zones.

2.2.5 SO_2 emission analysis

Figure 2.2.15 shows TROPOMI SO_2 vertical column densities on 16–17 June 2018, at the peak of the eruption. Strong SO_2 enhancements are observed directly above Kīlauea, with clear westward advection of the plume on 17 June. These gas emissions provide the precursor for secondary sulfate aerosol formation. Let us also note that the SO_2 plume observed downwind of the volcano, spatially collocated with the high AOD values (Fig. 2.2.5).

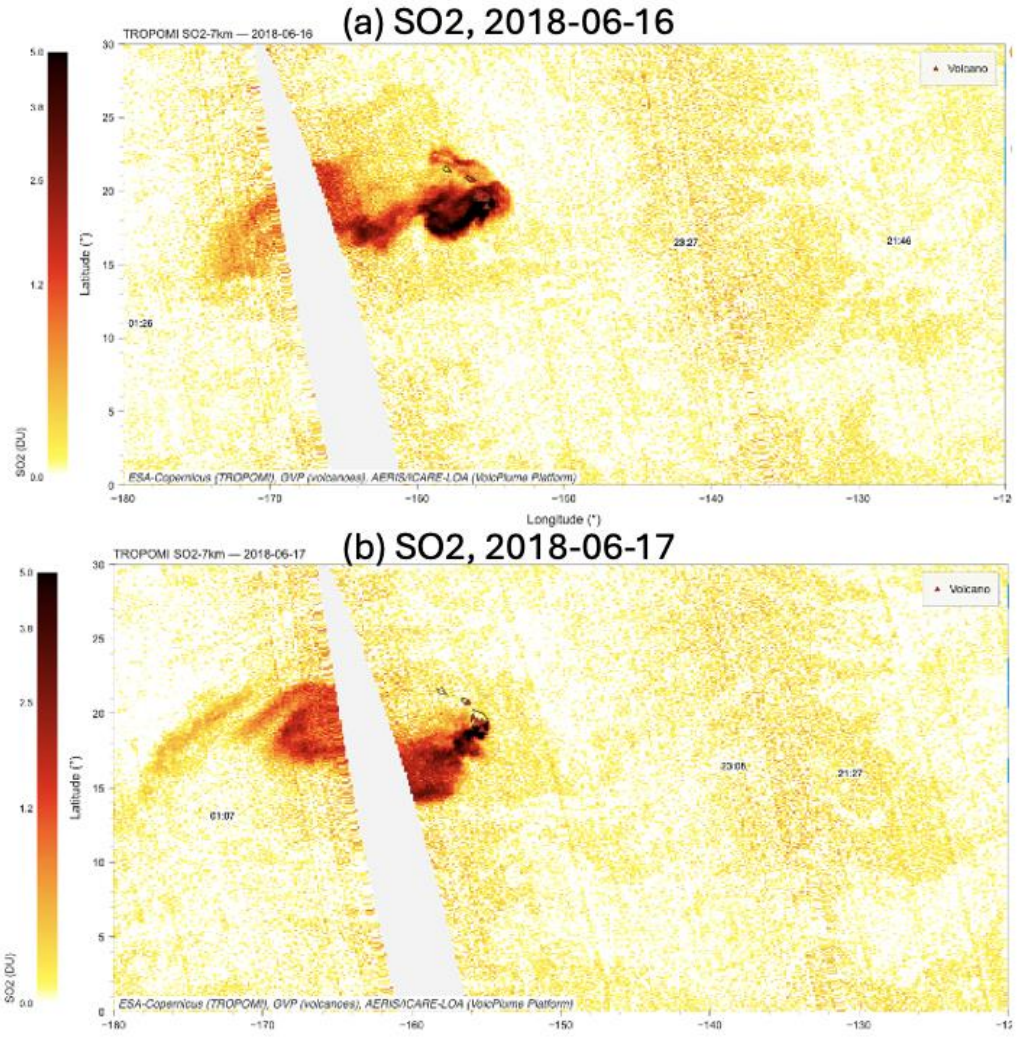

Figure 2.2.15. TROPOMI SO_2 vertical column density (7 km product) on (a) 16 June 2018 and (b) 17 June 2018, showing strong volcanic gas emissions from Kīlauea and plume transport westward.

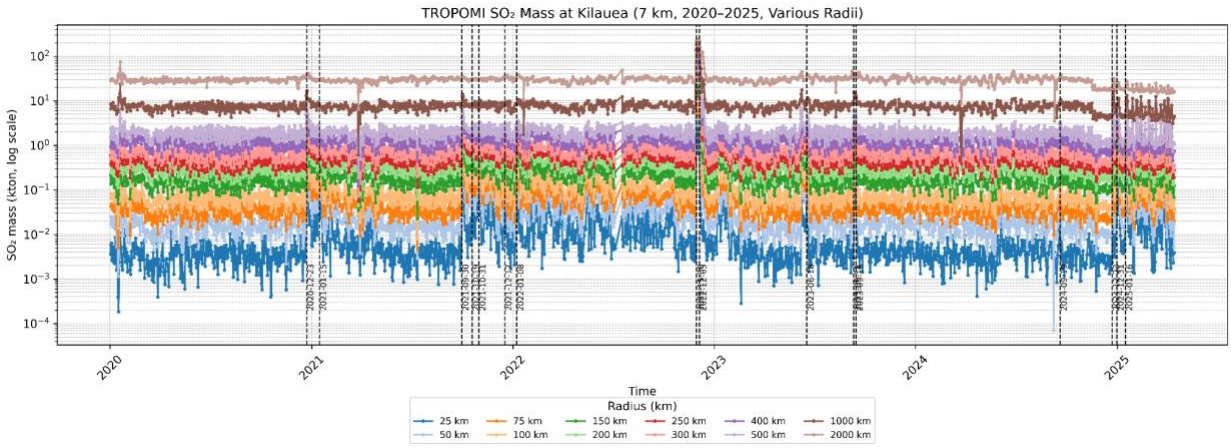

Figure 2.2.16. Time series of daily SO_2 mass derived from TROPOMI data over Kilauea (Hawaii) between 1 January 2020 and 15 April 2025, for circular areas ranging from 25 to 2000 km in radius. The *y*-axis is logarithmic, and vertical dashed lines indicate key eruptive events. This figure supports identification of eruption-related periods for further investigation of volcanic aerosols and their interactions with cloud properties.

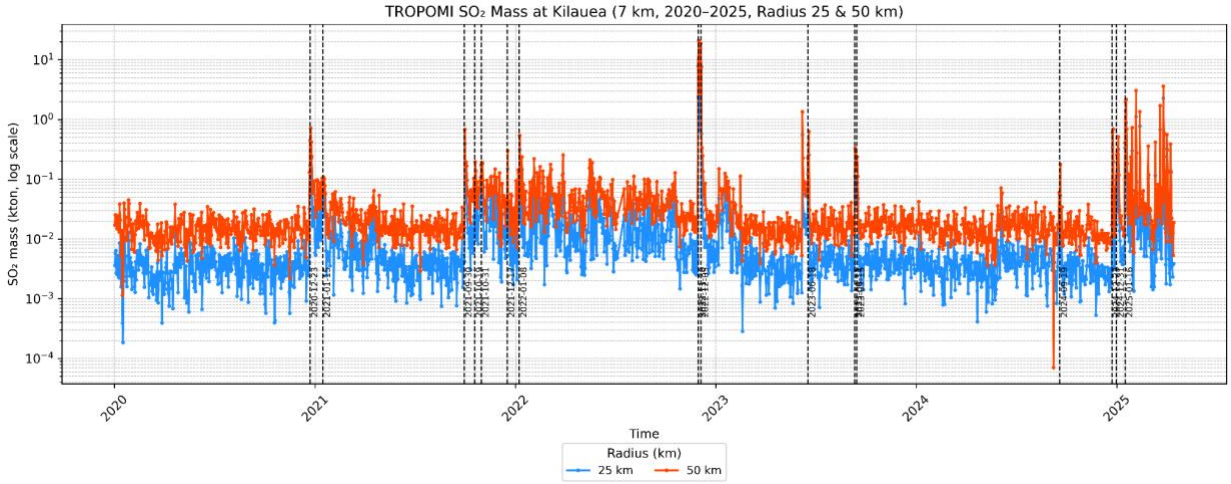

Figure 2.2.17. Same as Figure 2.2.16, but focused on the 25 km (blue) and 50 km (red) radii. These near-source time series allow clearer detection of high-intensity degassing episodes. This view is especially relevant for analyzing aerosol microphysics and cloud responses in the immediate vicinity of the volcano.

To better characterize the timing and intensity of SO_2 emissions from Kilauea volcano, we compiled and visualized five years of satellite retrievals from 1 January 2020 to 15 April 2025. The original dataset, provided by CNRS-LOA (Boichu et al.) via the VolcPlume platform, consisted of 13 folders, each covering five months of TROPOMI-based SO_2 mass time series at multiple distances from the volcanic vent (25 to 2000 km), along with SO_2 distribution maps for selected eruptive events.

To enable clearer identification of key eruptive periods and support selection of relevant case studies, we reconstructed a continuous time series for the full 5-year period. Two figures are presented: the first (Fig. 2.2.16) includes all radii from 25 to 2000 km, while the second (Fig. 2.2.17) focuses on the near-vent with 25 and 50 km radii for better visibility of small-scale degassing events. Both are plotted on a logarithmic scale, and known eruption dates (e.g., 2020-12-23, 2021-09-30, 2022-11-30, etc.) are marked with vertical dashed lines.

These visualizations help pinpoint high-SO_2 periods where targeted retrieval of cloud and aerosol properties may reveal volcanic aerosol-cloud interactions. The figure below (Fig. 2.2.18), showing the SO_2 column distribution on 11 September 2023, provides spatial context for one such eruptive event. A dense SO_2 plume can be seen extending southwest of Kilauea, illustrating the need to account for spatial transport in evaluating cloud and aerosol responses.

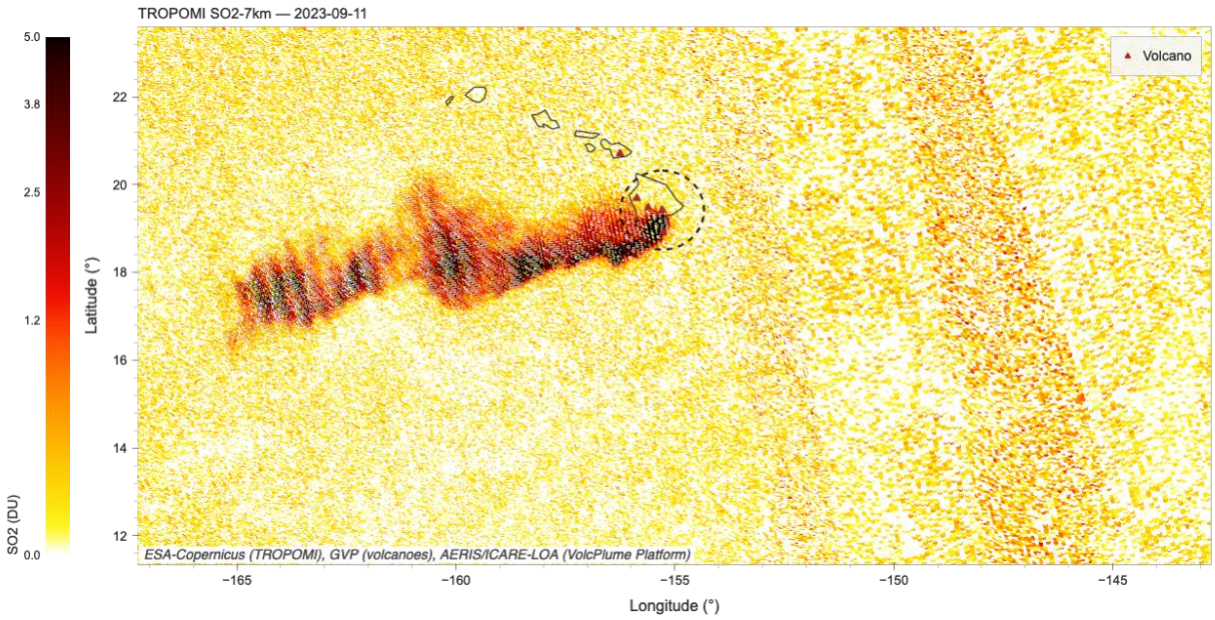

Figure 2.2.18. TROPOMI SO_2 column amount (7 km altitude product) over the Pacific Ocean region on 11 September 2023, showing a pronounced SO_2-rich plume originating from Kilauea. The dense SO_2 core extends west-southwest, consistent with degassing during the eruption identified in the time series. Data provided by CNRS/LOA using the VolcPlume web platform (Boichu and Mathurin, 2022).

While this section focused on case studies from June 2018 to demonstrate the capability of the SYREMIS/GRASP synergetic retrievals during the Kīlauea eruption, a broader temporal perspective is also valuable. Figures 2.2.16 to 2.2.18 show a time series of SO_2 over the Kīlauea region spanning multiple years. These long-term records capture several

eruptive events and provide a basis for systematic comparisons between different eruption phases and plume evolutions.

Such multi-year analyses will enable us to:

- assess the consistency of the synergetic retrievals across different eruptive episodes,
- quantify the variability of volcanic aerosol properties in time, and
- identify cases most relevant for Marine Cloud Brightening analogues.

In future work, these extended time series will be further explored to characterize the temporal evolution of volcanic aerosol–cloud interactions and to strengthen the use of volcanic eruptions as natural laboratories for assessing SRM strategies.

2.2.6 Cloud statistics analysis

According to aerosol and SO_2 retrieval results (Figs. 2.2.2 to 2.2.7, 2.2.18), the volcanic plume in 2018 is localized in the North-West and South-West parts of the considered Kilauea volcano area, whereas the North-East and South-East parts are not affected by volcanic eruption. Moreover, South-West contains most of the aerosol and SO_2 plume when compared with the North-West zone.

Figs. 2.2.19a, 2.2.19b, and 2.2.19c show an example of the weekly PDFs of the TOA reflectance at 865 nm for optically moderate clouds (ACOM=6, Cloud Optical Depth (COD) 3<COD<7) and for three years: June 2017, 2018 and 2019 (before, during and after volcano eruption). The following regularities can be noticed:

1. Considerable changes in statistical characteristics (e.g., PDF asymmetry, shape, mean and most probable values etc.) of the TOA reflectance at 865 nm for “moderate” cloud classes in NW and SW part in 2018 in comparison to 2017 and 2019.
2. The biggest changes in the TOA reflectance statistics are observed in SW zone in 20018, most affected by aerosol and SO_2 plume from Kilauea volcano.
3. NE and SE zones in 2018, which are not affected by volcano plume, show similar statistical characteristics of the TOA reflectance as in 2017 and 2019.
4. Years 2017 and 2019, which are not affected by the Kilauea volcano eruption, show similar statistical properties for each of the geographical zones.

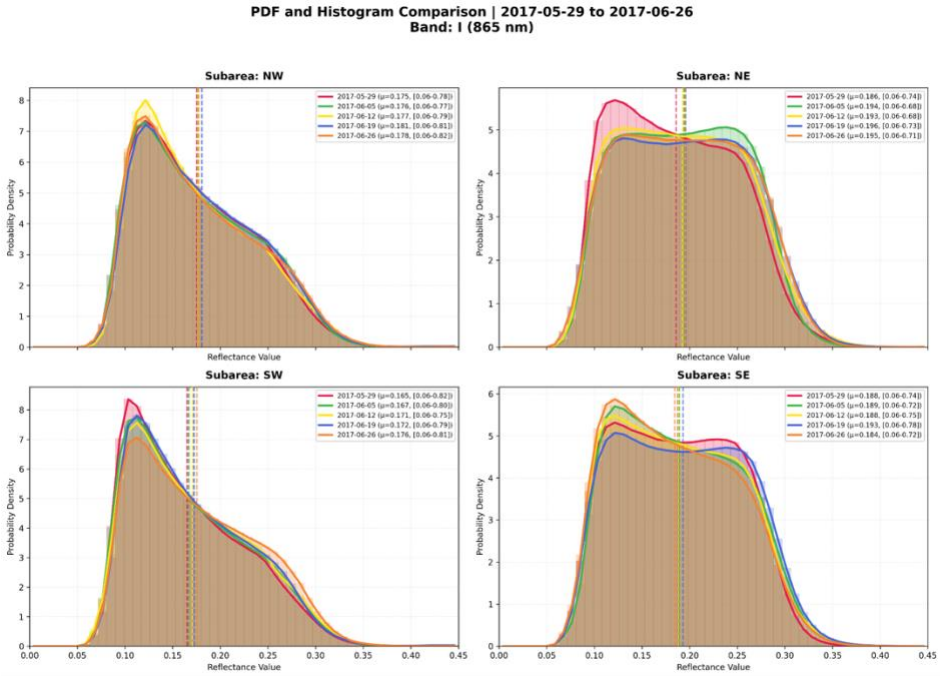

Figure 2.2.19a. Weekly PDFs of I(865nm) (TOA reflectance) for 4 geographical zones: NW, SW, NE, SE for “cloud moderate” (ACOM=6) classes in June 2017 (before volcano eruption).

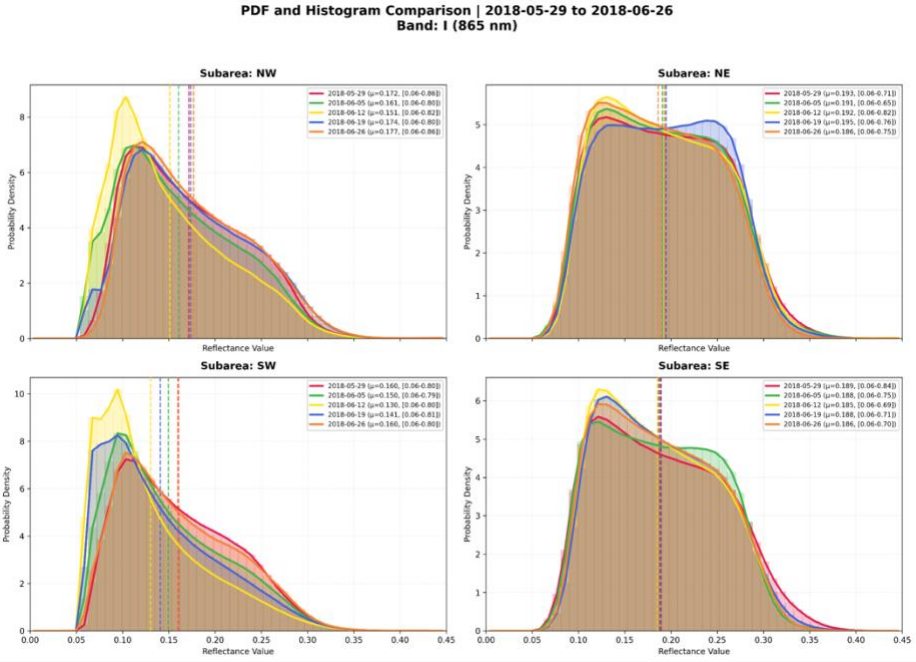

Figure 2.2.19b. Weekly PDFs of I(865nm) (TOA reflectance) for 4 geographical zones: NW, SW, NE, SE for “cloud moderate” (ACOM=6) classes in June 2018 (during volcano eruption).

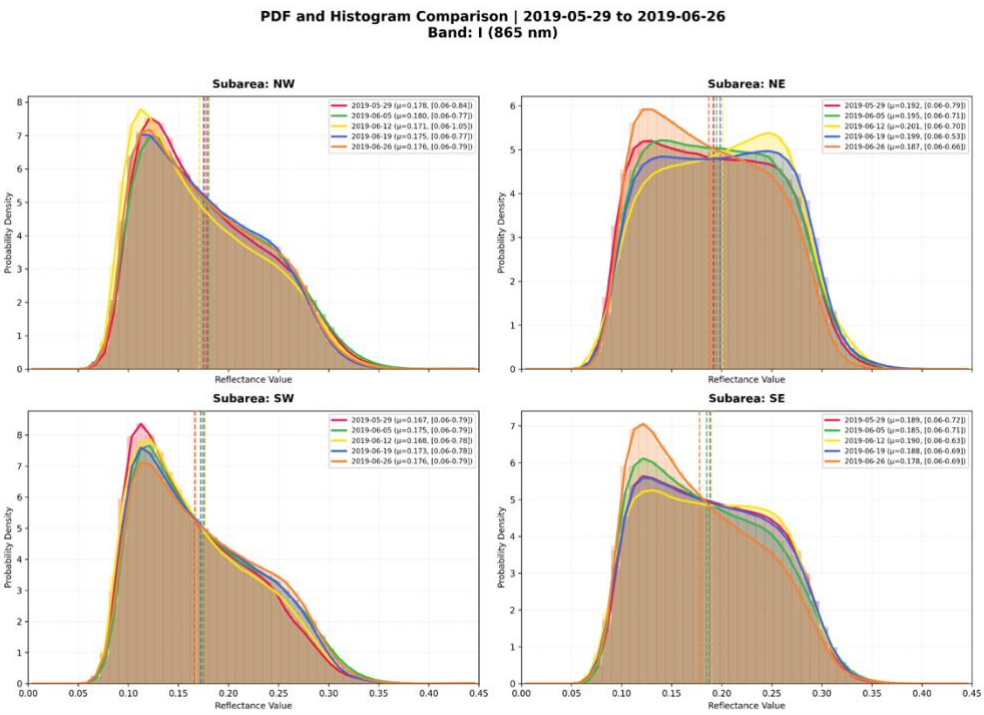

Figure 2.2.19c. Weekly PDFs of I(865nm) (TOA reflectance) for 4 geographical zones: NW, SW, NE, SE for “cloud moderate” (ACOM=6) classes in June 2019 (after volcano eruption).

The time series for the mean value of the TOA reflectance for thick and moderate cases from May to September 2018 is presented in Fig.2.2.20a. Similar to PDFs in Figs 2.2.19a-2.2.19c, the averaging was done over all SZA and VZA of OLCI observations within the specified period and separately for 4 geographical zones. For thick clouds, no noticeable changes in the reflectance properties are observed before (May 1 – May 15), during (May 15 – August 14) and after (August 15 – September 4) volcanic eruption event in 2018. For moderate clouds (3<COD<7, ACOM=6), one can observe considerable changes in cloud reflectivity. In particular,

(i) Considerable changes in cloud reflectivity at 865 nm in SW and NW zones, affected by volcano plume.

(ii) No significant changes in cloud reflectivity at 865 nm in SE and NE zones, which are not affected by volcano in 2018.

(iii) The biggest changes in the cloud reflectivity at 865 nm is observed in SW zone, which is the one most affected by volcano plume. Here, the mean cloud reflectance considerably decreased in June and July 2018 in comparison to the beginning of May (pre-volcanic period) and August-September (post-volcanic period), 2018: from ~0.18-0.17 to ~0.14 in mean reflectance value. Such cloud “dimming” effect is more pronounced at 865 nm than at 412 nm.

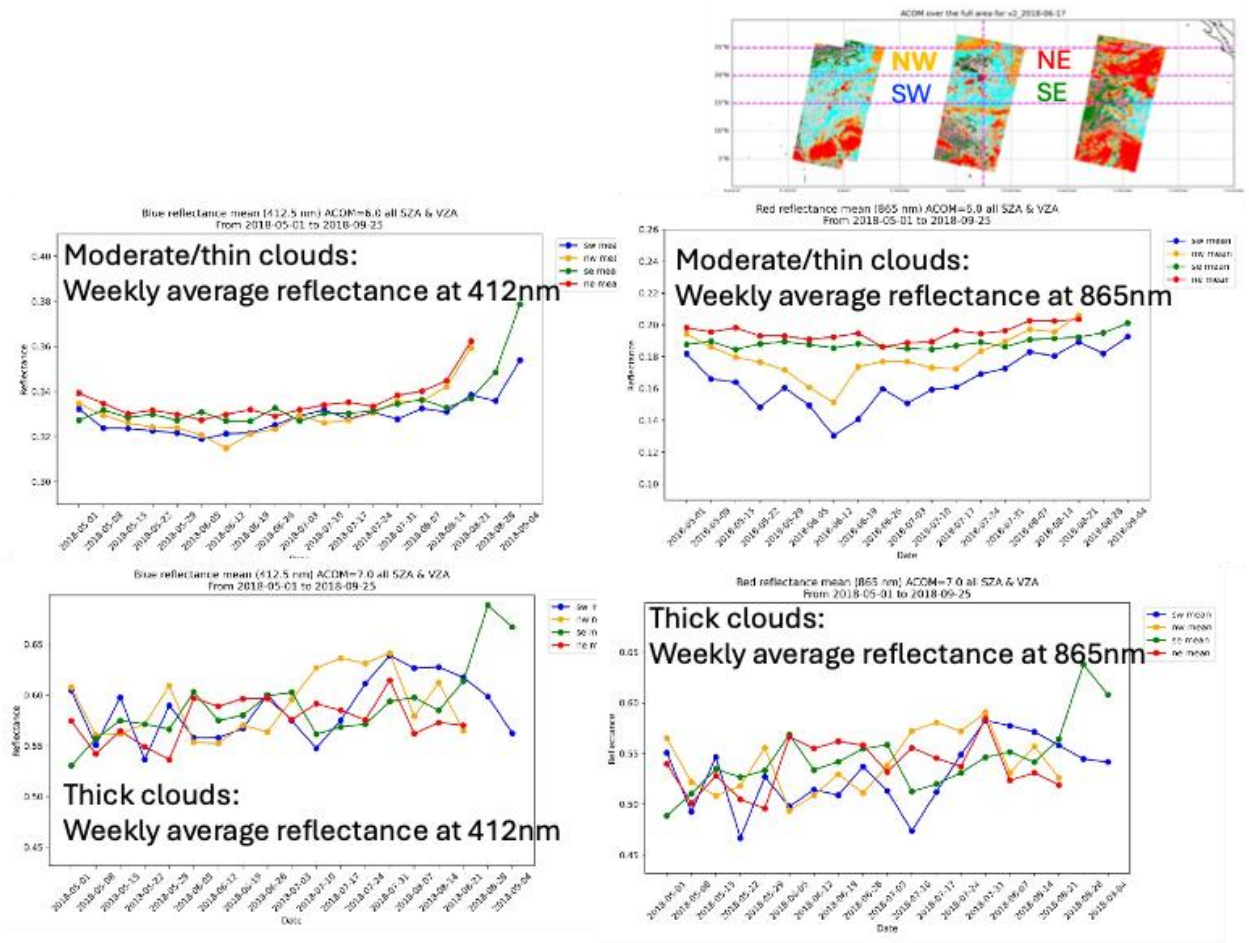

Figure 2.2.20a. Weakly mean value of TOA reflectance at 412 and 865 nm for thick (ACOM=7) and moderate (ACOM=6) clouds from May 1st to September 4th, 2018. The statistics in NW, SW, NE and SE geographical areas are marked in orange, blue, red and green colors, respectively.

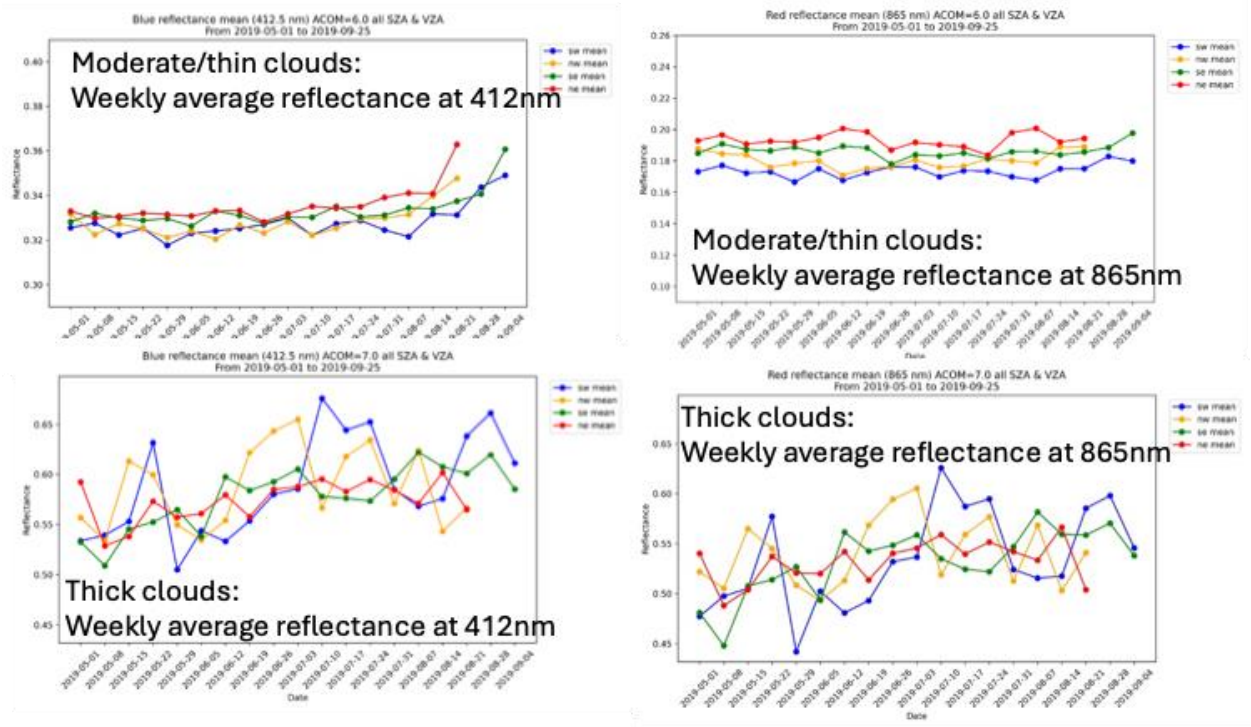

Figure 2.2.20b. Similar time series as in Fig.2.2.20a but for 2019.

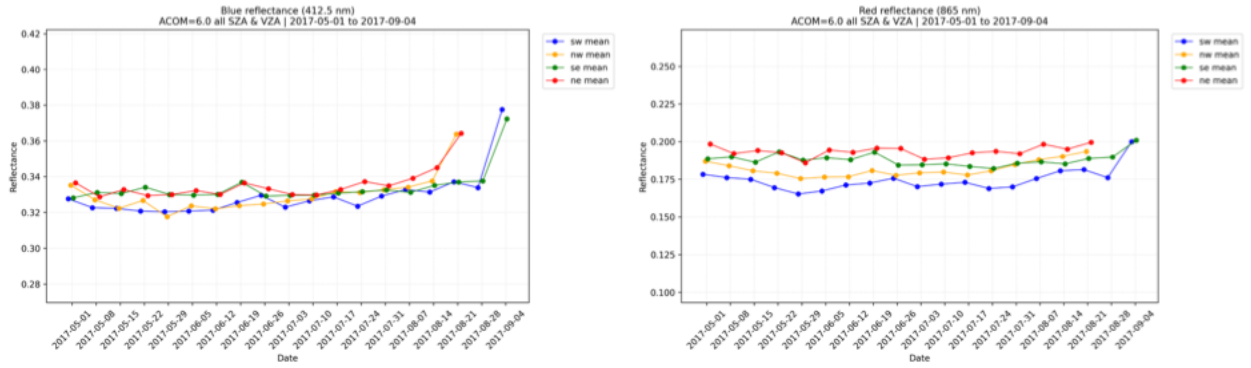

Figure 2.2.20c. Similar time series as in Fig.2.2.20b but for 2017 and ACOM=6 only (optically moderate clouds).

Similar statistical analysis performed for 2017 and 2019 years, which are not affected by the Kilauea volcano eruption, does not show any cloud “dimming” effect for any of the 4 considered zones (Fig.2.2.20b and 2.2.20c).

To better understand the observed “dimming” effect for the optically moderate clouds, the cloud statistics analysis was combined with aerosol and SO_2 retrieval results (Sections 2.2.3 and 2.2.5) as well as gas-to-particle transformation (SO_2 to SO_4 estimate) estimated from transport models.

2.2.7 MCB analysis for Kilauea volcano case

MCB analysis for the Kilauea volcano case is based on the synthesis of aerosol (Section 2.2.3), SO2 (Sections 2.2.5) retrieval datasets, and ACOM statistical results for clouds (Section 2.2.6). To account for gas-to-particle transformation and the secondary aerosol effect on cloud reflectivity properties, SO_2 to SO_4 estimates were included in the analyses from CAMS reanalysis.

Figures 2.2.21a and 2.2.21b show time series of the weakly mean aerosol properties (AOD at 412 and 865 nm, AE, SSA(440 nm)), derived from the SYREMIS/GRASP retrieval (Section 2.2.3) in 2018 and 2019. Similar to the weekly mean cloud reflectance in Fig.2.2.20a and Fig.2.2.20b, the results are presented for 4 geographical zones (NW, SW, NE, and SE). Fig.2.2.21b shows background aerosol properties over the Kilauea Pacific region. One can observe drastic changes in aerosol characteristics in NW and SW zones in 2018 due to volcano eruption, while the aerosol properties in NE and SE zones are quite stable and similar to those derived for a similar period in 2019. The maximum value of AOD at 412nm is observed in the SW zone in June and July 2018. In the middle of June, time series show domination of very small and nonadsorbing particles (AE>1.6 and total SSA(412 nm)>0.96), which corresponds to the domination of small SU particles.

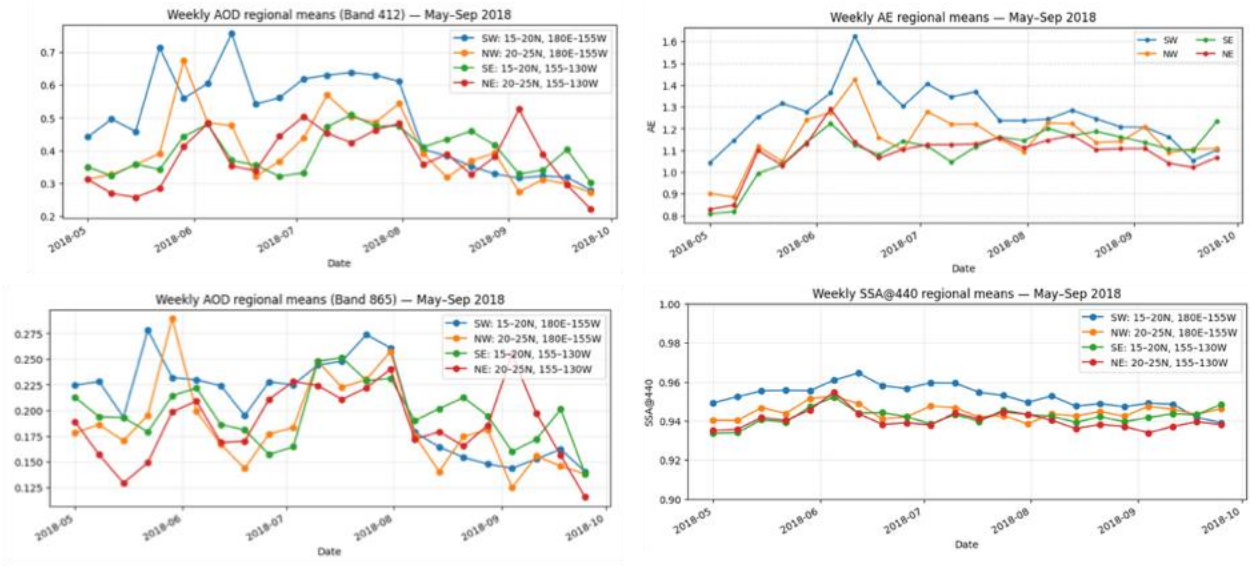

Figure 2.2.21a. Time series of the weekly mean aerosol properties (AOD(412nm), AOD(865nm), Angström Exponent (AE) and SSA(443nm) from May 1st to October, 2018. The statistics in NW, SW, NE and SE geographical areas are marked in orange, blue, red and green colors, respectively.

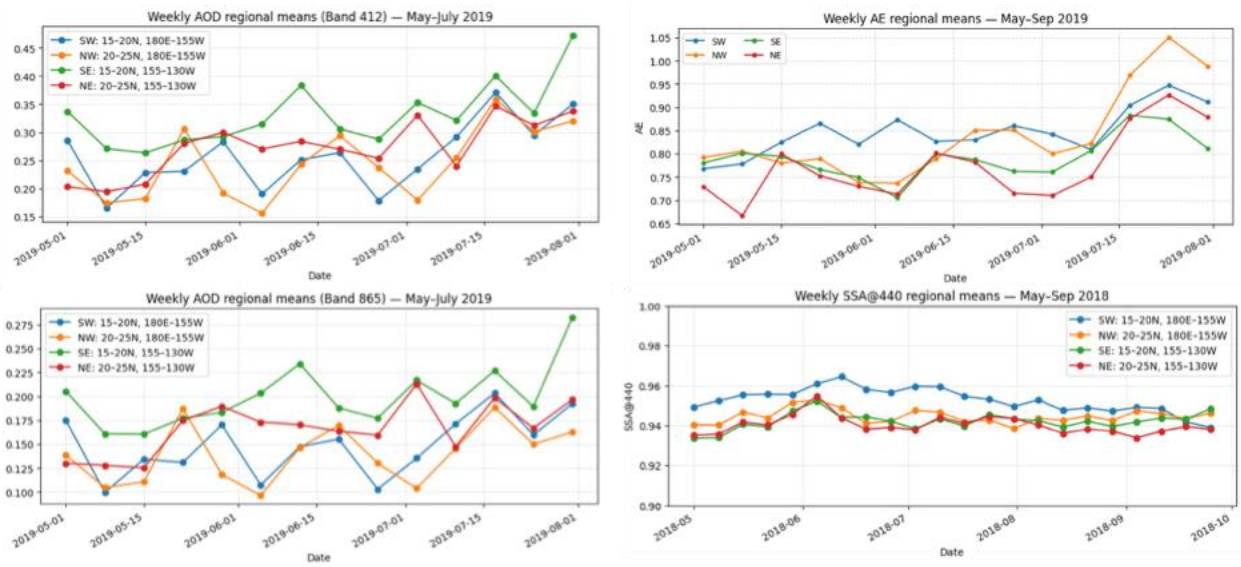

Figure 2.2.21b. Same as Fig.2.2.21a but for 2019.

As it was discussed in Section 2.2.3, SYREMIS/GRASP aerosol retrieval shows that aerosol loading in volcano plume increases with distance from volcano, which can be an indicator of gas-to-particles transformation (SO2 -> S04 evolution). These small secondary aerosol particles can serve as Cloud Condensation Nuclei (CCN), strongly affecting cloud formation as well as their physical and reflectivity (brightness) properties. The SYREMIS/GRASP synergetic retrieval provides aerosol typing (Litvinov at al., 2024, 2025), which can be used to derive CCN (Cloud Condensation Nuclear) proxy estimates. Figure 2.2.22 shows a weakly mean CCN proxy calculated from aerosol retrieval presented in Fig.2.2.21a. Together with CCN, weakly mean SO4 concentration estimates from CAMS reanalysis for 2018 May-September is presented in Fig.2.2.22. For SW-zone affected by volcano plume, one can observe remarkable correspondence in temporal dependence of both characteristics independently derived from the SYREMIS/GRASP synergetic remote sensing approach and CAMS model. In particular, both CCN and SO4 estimates in the SW-zone are very similar to those for other geographical zones at the beginning of May before the volcano eruption. After the eruption both characteristics increase in a very synchronous way. They reach maximum values in the middle of June 2018, show quite stable temporal dependence in July, and then start gradually decreasing in August, reaching background level again in September 2018.

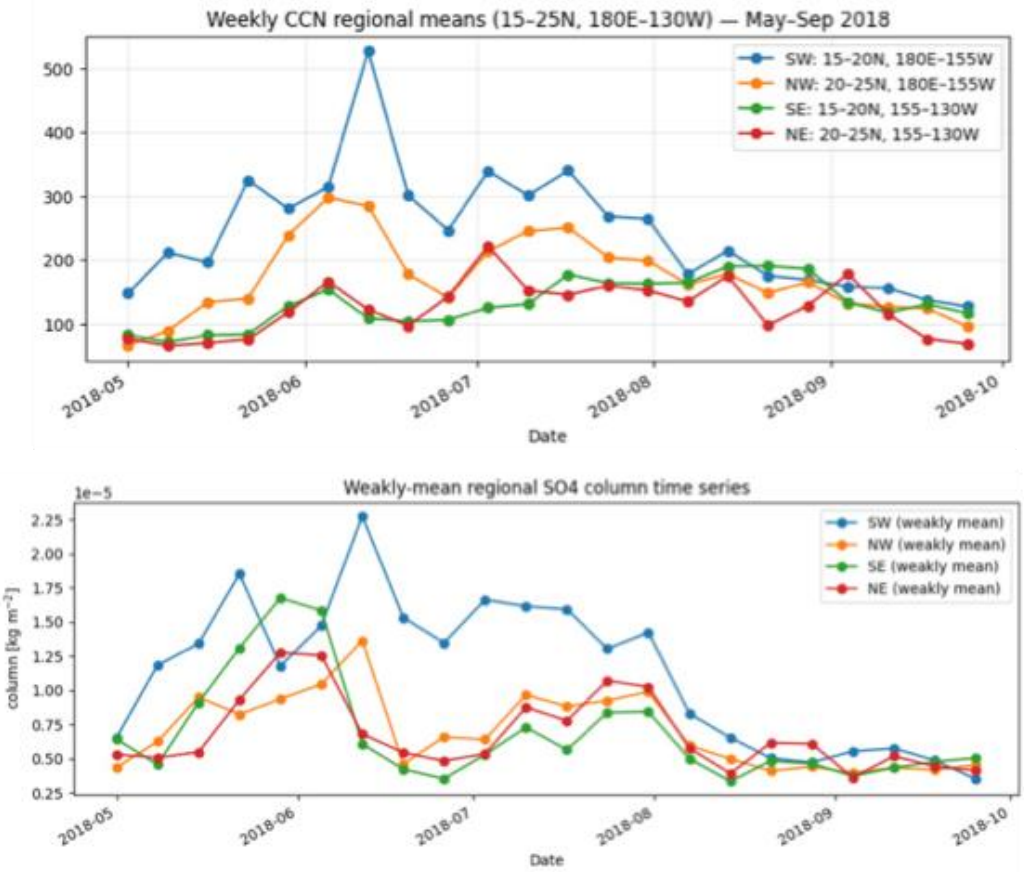

Figure 2.2.22. CCN estimates from SYREMIS/GRASP and CAMS SO_4 proxy for 2018.

Figure 2.2.23 combines the temporal time series for cloud reflectance and aerosol CCN proxies in 2018 and 2019 for the four geographical zones. Overall, the temporal dependence of the CCN and SO_4 estimates strongly correlates with the decreasing of the reflectivity (brightness) of the optically moderate clouds in the period from May to September 2018 in SW zone (Fig.2.2.20a). The effect is not observed for the 2017 and 2019 years, which are not affected by volcano plume and do not show considerable presence of the secondary SU aerosol formation (Fig.2.2.23). This allows us to conclude that the observed cloud “dimming” effect is most likely caused by the primary and secondary aerosol from the Kilauea volcano plume, which alternate the cloud formation and physical properties. The observed cloud “dimming” is opposite to cloud “brightening” effect usually expected from aerosol-cloud interaction.

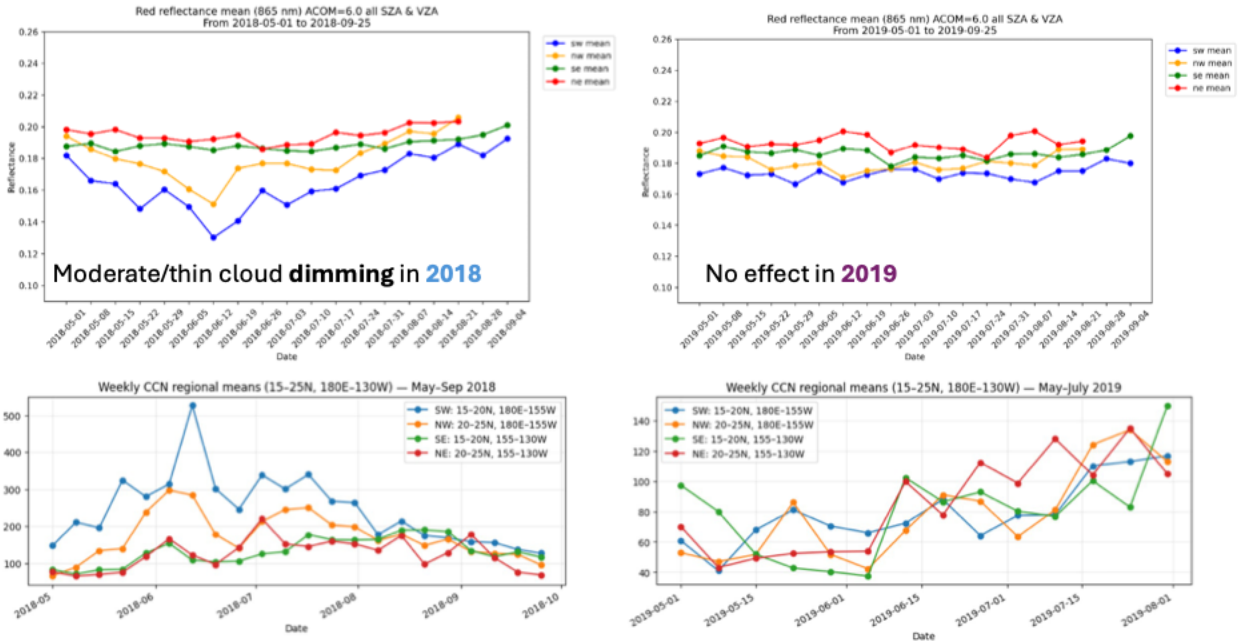

Figure 2.2.23. Time series of the weekly mean reflectance (for optically moderate clouds) and CCN estimates for 2018 (left) and 2019 (right) presented for four geographical zones.

Overall, cloud “dimming” means that less radiation is scattered back to space by clouds. This may result in a warming atmosphere in contrast to cloud "brightening" effect leading to cooling of the climate system. Nevertheless, the regional cooling or warming effect depends on a number of other parameters which should be accounted for together: the cloudy conditions, type of the aerosol and underlying surface, gas-to-particles transformation, and aerosol effect on cloud formation and cloud properties. The understanding of cloud “dimming" effect and its contribution to cooling/warming requires further natural analogues studies based on synthesis of the vast information from aerosol, gas and cloud remote sensing as well from regional transport models.

2.3 Cirrus and Mixed-phase Cloud Thinning (CCT-MCT) - WP2300/3300

2.3.1 Methods

In contrast to SAI and MCB, there are no obvious natural or anthropogenic analogues that can readily be used to constrain Earth System Model simulations for the purpose of CCT and MCT. However, there is observational evidence that industrial point sources of ice nucleating particles (INPs) can modify high-latitude mixed-phase clouds (Toll et al., 2024), giving a qualitative indication of how mixed-phase clouds could respond to INP perturbations. While this gives an indication of MCT viability, the sources are too localized for meaningful comparison with coarse ESM output. Similarly, there is observational evidence that cirrus cloud microphysical properties may respond to aircraft emissions (e.g., Urbanek et al., 2018), but quantitative evidence for the purpose of ESM evaluation is lacking. Earth observations can nevertheless be used to constrain ESMs when it comes to mixed-phase and cirrus cloud properties.

For MCT, which aims to modify cloud phase, it is critical that ESMs have a correct starting point. This can be ensured by evaluating the simulated cloud phase using active remote sensing, and specifically the supercooled liquid fraction (SLF) from CALIOP. CALIOP data can provide SLF information for both cloud top (dashed lines in Figure 2.3.1) and cloud bulk/interior (solid lines in Figure 2.3.1), following the approach of Hofer et al. (2024). Simulating an accurate cloud phase is particularly important in the extratropical winter hemispheres, where MCT could plausibly yield cooling through increased outgoing longwave radiation in response to optically thinner mixed-phase clouds. In STATISTICS, the NorESM model has been evaluated and constrained with CALIOP SLF data, to increase the likelihood of a realistic simulation of the mixed-phase cloud response to subsequent simulations with INP injections (at around 1 km). The seasonal variations in SLF in the northern hemisphere extratropics (N-ET, see top panel in Figure 2.3.1) give a tentative indication that SLF does indeed respond to INP perturbations, here due to seasonal variations in INP emissions.

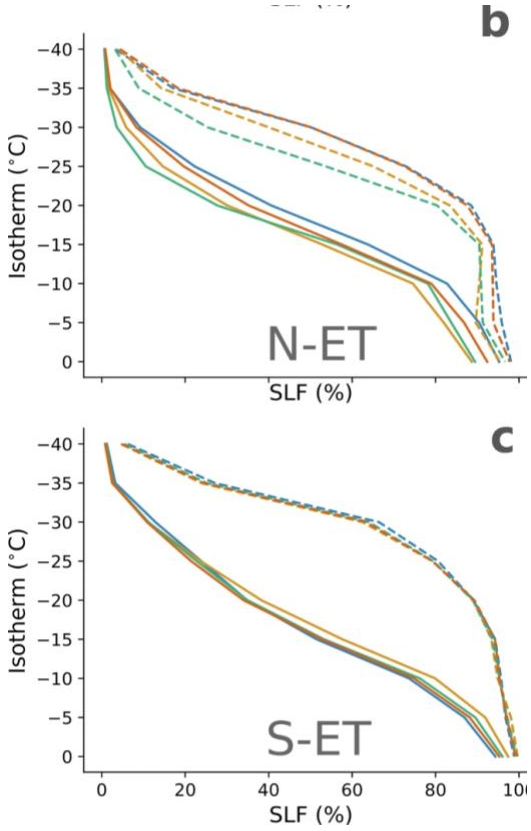

Figure 2.3.1. Vertical profile of the supercooled liquid fraction (SLF) shown against the local temperature for the northern hemisphere extratropics (N-ET) and southern hemisphere extratropics (S-ET). Dashed lines represent cloud top, solid lines represent cloud interior/bulk, for December - February (blue), March - May (yellow), June - August (green), September - November (red).

For CCT, the critical quantity to simulate accurately in ESMs is ice crystal number concentrations (ICNCs), which also give a clear indication of the ice crystal formation mechanism. An approximation indicative of homogeneous nucleation is ICNC larger than 100 L^{-1}. Using this approximation, we see from Figure 2.3.2 that the high latitudes appear to be dominated by homogeneous freezing, which is promising because this is a prerequisite for CCT viability. For an ESM simulation of CCT to be meaningful, the simulated cirrus clouds prior to INP injection must form by the correct ice crystal formation mechanism. Once we have confirmed this using ICNC retrievals (as in Mitchell et al. (2018), see Figure 2.3.2), we can be more confident that INP injections at cirrus level (at around 7 km) yield realistic estimates of CCT viability.

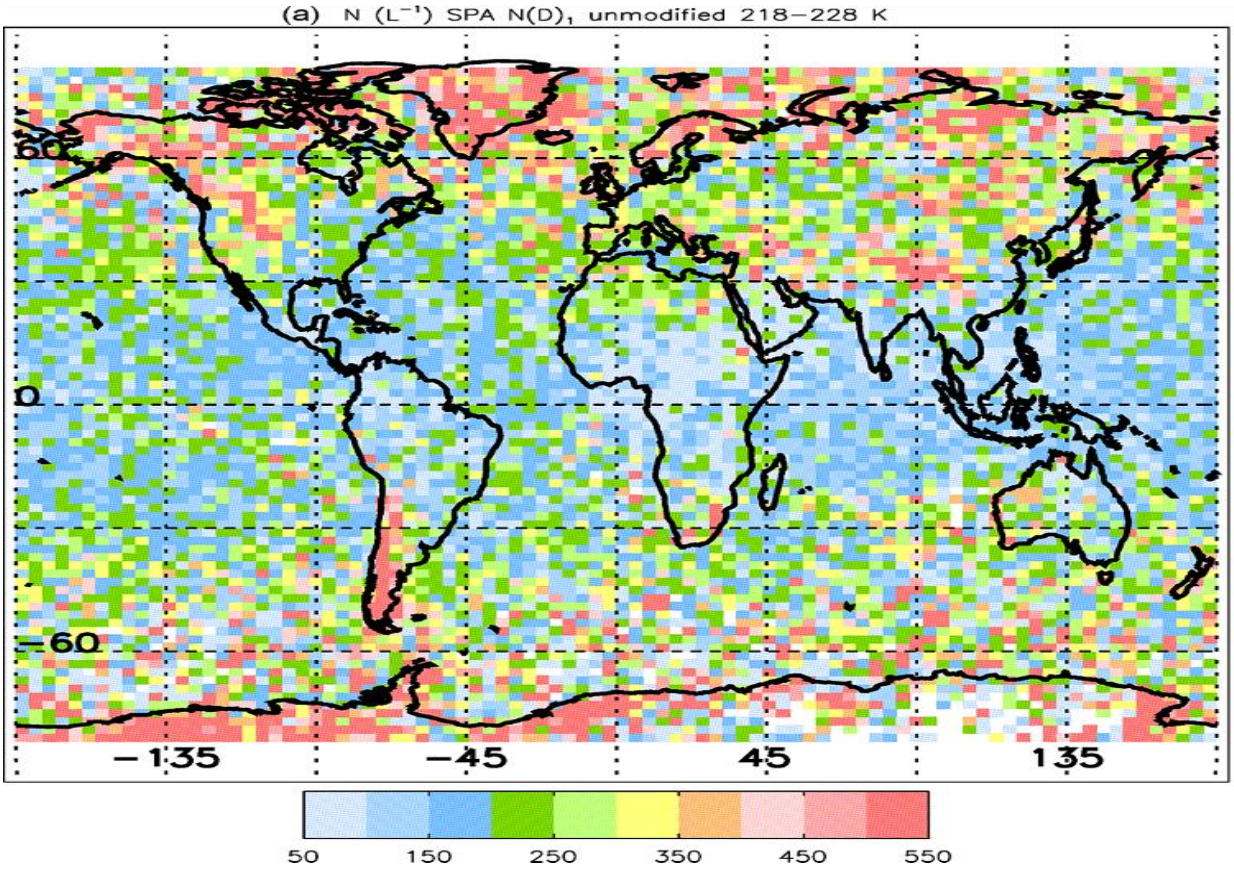

Figure 2.3.2. Geographical distribution of median ice-particle number concentration *N* (L^{-1}) during 2008 and 2013, where the layer representative temperature, *T*c, is between 218 and 228 K. The retrievals use the SPARTICUS *N*(*D*)1 unmodified formulation.

2.3.2 Experimental design

We use version 2.3 of the Norwegian Earth System Model (NorESM2.3; Seland et al., 2020) and run it in a fully-coupled configuration. That is, all model components are active and exchange information. The atmospheric component (CAM6-Nor) has 32 vertical levels, ranging between the Earth's surface and 3.6 hPa (ca. 40 km), and we use a nominal 1° latitude-longitude horizontal grid.

Our aim is to explore the impacts of seeding Arctic mixed-phase and cirrus clouds and subsequent impacts on surface climate in the Arctic. For this purpose, we inject mineral dust ($AlSiO_5$, which is effective as ice nucleating particles, INP) at 1 and 7 km above sea level (+/- 0.2 km) in two sets of simulations. The 1 km simulations target low level Arctic mixed-phase clouds, while the 7 km simulations target Arctic cirrus clouds. The emissions are uniformly spread throughout the area north of 70°N, excluding landmasses, and implemented for the six months period between October and March. In the simulations

presented in this report, we emit mineral dust at the rate of 10 kt/day as accumulation mode particles (initial median radius of 0.22 μm).

To account for different meteorologies and isolate the impacts of the dust seeding, we generate ensembles of independent pairs of simulations. Each pair consists of a control run, with no artificial dust emissions, and an experimental run, which includes artificial dust emissions. The difference between these two simulations reveals the impacts of the dust seeding. To generate independent ensemble members, we apply perturbations to the initial temperature field and let the model run for ten months before the start of the dust seeding implementation. Our initial ensembles consist of five members (but should ideally be expanded to ten in follow-up research), and for each member the initial temperature perturbation is different. Our simulations are transient and start in the year 2030, assuming the SSP2-4.5 scenario, and last for two winters (simulations should ideally be expanded to five years in follow-up research). From the ensembles of anomalies, we calculate means and estimate their significance (at 95%) using a two-tailed t-test.

We choose our emission rate (10 kt/day) as it leads to a large increase in the wintertime dust column burden in the Arctic (by up to a factor of five), while still staying in the range of the natural seasonal cycle as simulated in the model (emitting 10 kt/day results in a wintertime dust column burden approximately half the natural column burden during summer), see Figure 2.3.3.

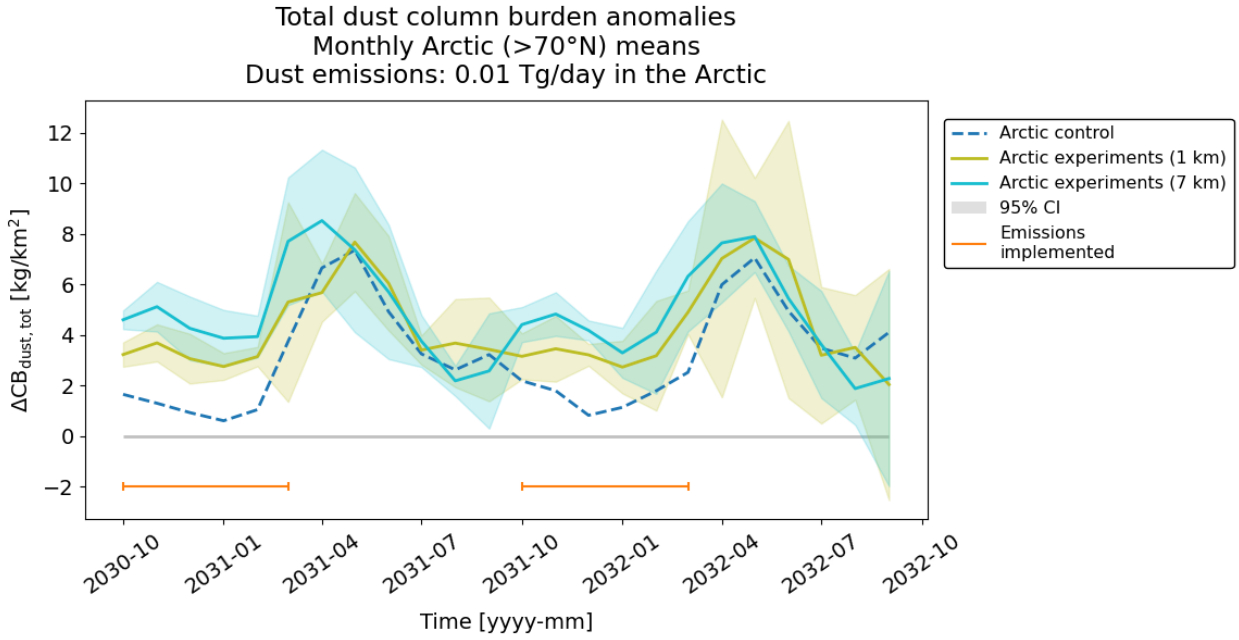

Figure 2.3.3: Monthly Arctic mean (north of 70°N, excluding land) dust column burden from the NorESM2.3 simulations. The dashed blue line indicates the control mean, and the olive green and cyan lines the 10 kt/day experiments at 1 and 7 km, respectively. The shaded regions indicate 95% confidence intervals based on a two-tailed t-test. The orange bars indicate the periods when the artificial dust emissions are implemented.

2.3.3 Results: Background conditions

Before looking into the cloud and climate responses to the artificial dust seeding, it will be useful to understand the Arctic background conditions as they appear in the NorESM2.3 control simulations. Figure 2.3.4 shows monthly vertical sections of background Arctic mean relative humidity (colors) and temperature (dashed contours). Looking at the vertical temperature profiles during winter, we see a prominent and strong inversion layer close to the surface. In this inversion layer, the relative humidity is consistently above 100%. This may indicate an aerosol limited regime, i.e. that the aerosol concentrations are so low that cloud formation and the subsequent relaxation of the relative humidity towards 100% is inhibited. Also worth noting is that at 7 km altitude, supersaturation is uncommon. The temperature at this altitude stays below -35°C, indicating pure ice clouds, which is desirable for CCT to be effective.

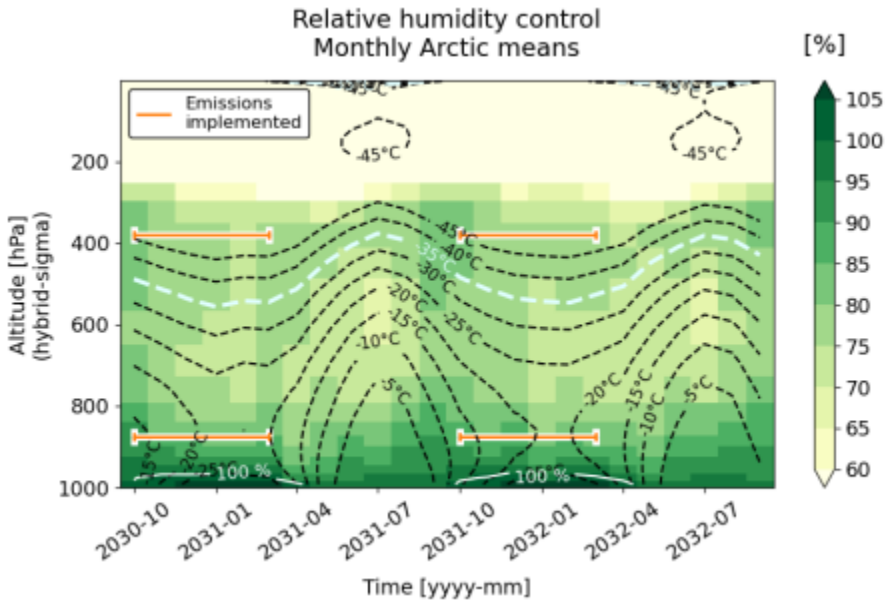

Figure 2.3.4. Monthly vertical sections of the Arctic mean (north of 70°N, excluding land) relative humidity from the NorESM2.3 control simulations (colors) and temperature (dashed contours). The orange bars indicate altitudes and periods of artificial dust emissions.

Figure 2.3.5 shows Arctic mean vertical sections of control dust concentrations along with the altitude and periods of artificial dust emissions (orange bars). Between altitudes of ca. 7 and 9 km (ca. 400 to 250 hPa) there is a considerable amount of dust. It originates at lower latitudes and is transported to the Arctic in the upper troposphere-lower stratosphere region. This dust layer is sustained throughout the year although it is much thicker during summer than winter. Note that during winter, this dust is constrained to higher altitudes. Conversely, the lower troposphere is very dust poor in the Arctic during winter.

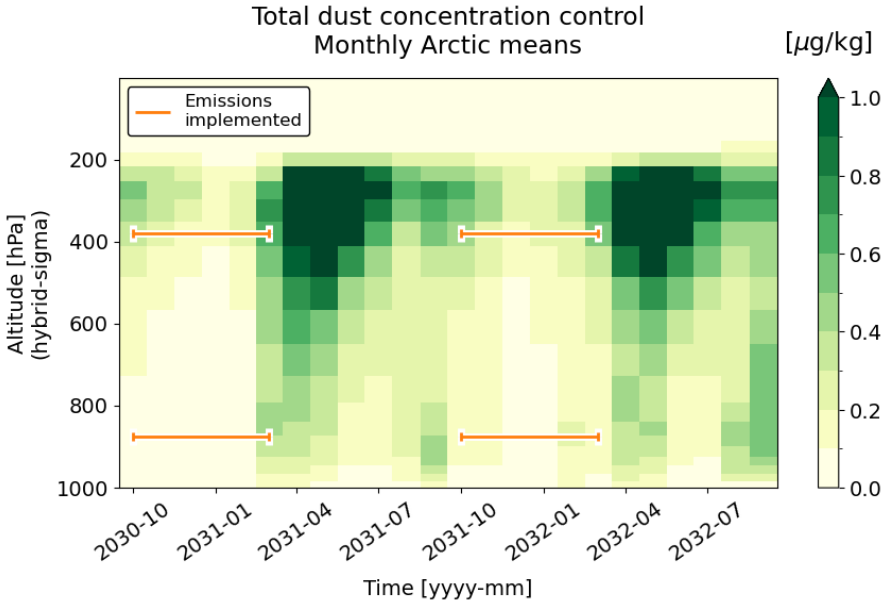

Figure 2.3.5: Monthly vertical sections of Arctic mean (north of 70°N, excluding land) dust concentrations from the NorESM2.3 control simulations. The orange bars indicate altitudes and periods of artificial dust emissions.

Let's turn our attention to the background clouds (Figure 2.3.6). As expected, Arctic clouds in the upper troposphere are ice clouds during all seasons. In the lower troposphere, we see mixed-phase clouds throughout the year, though ice clouds are more prominent during winter and liquid during summer. Note that in the wintertime surface inversion layer (Figure 2.3.4), we predominantly have ice clouds.

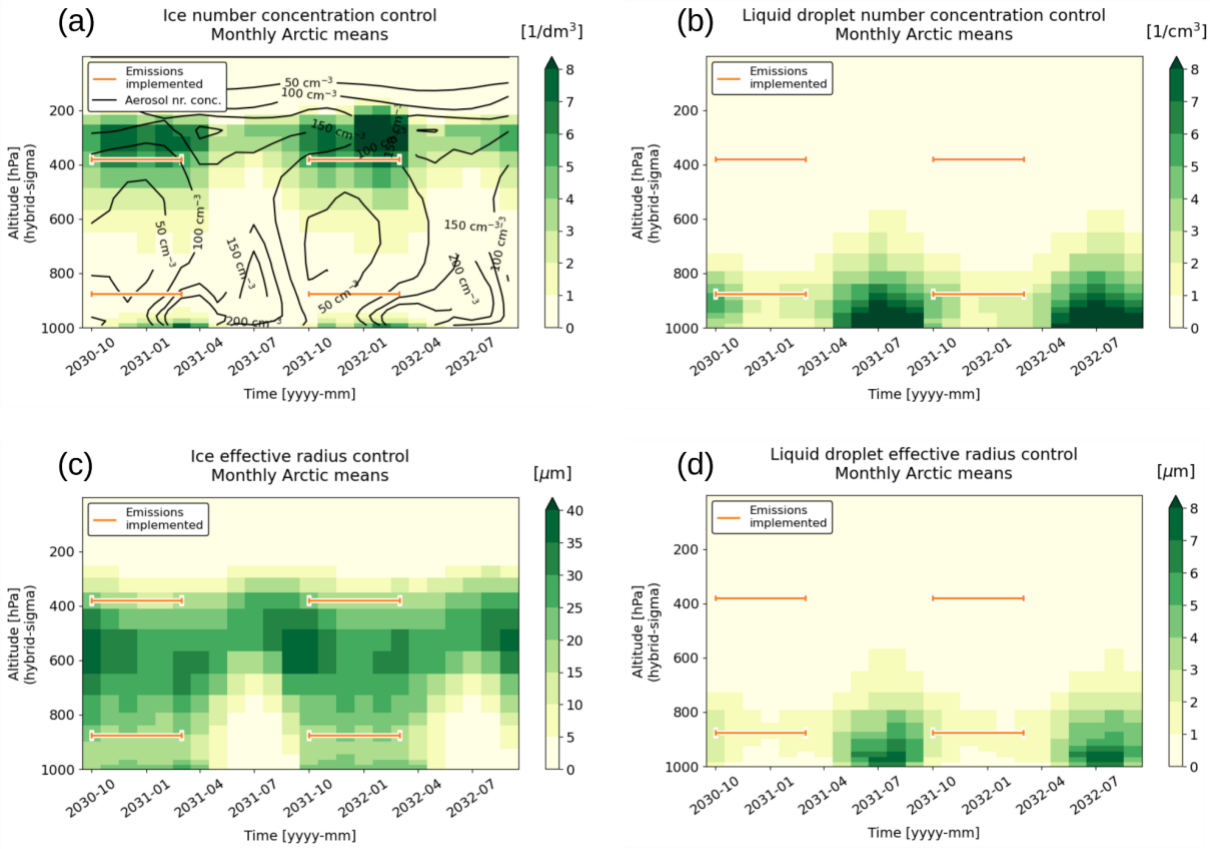

Figure 2.3.6: Monthly vertical sections of the Arctic mean (north of 70°N, excluding land) (a) ice crystal and (b) liquid droplet number concentrations, and (c) ice crystal and (d) liquid droplet effective radius from the NorESM2.3 control simulations. The orange bars indicate altitudes and periods of artificial dust emissions. The black contours in (a) indicate background total aerosol number concentration.

Sustained supersaturation (monthly mean RH>100%), relatively low ice number concentration and low liquid droplet number concentration indicate an aerosol limited cloud regime in the lowermost troposphere in the Arctic during winter. Seeding might therefore lead to increased cloud formation (more numerous and larger cloud particles, accompanied with increased water content and cloud cover) accompanied with a decrease in RH. If the seeding is strong enough to result in undersaturation (RH<100%), we might see a further increase in cloud particle number concentration but a decrease in cloud particle size. This could potentially lead to longer lifetimes of the clouds in the surface inversion layer. If the interpretation that cloud formation in the wintertime surface inversion layer is aerosol limited is correct, then seeding with mineral dust (INP's) should not lead to thinning of the mixed-phase clouds, but rather thickening. In the case of an

aerosol limited regime, the fact that saturation water vapour pressure is lower over ice than liquid water might be expected to be of secondary importance (of primary importance would be the high supersaturation) and not govern the mixed phase cloud response to mineral dust seeding. Also, in the supersaturated inversion layer, there is very little background liquid water, it is mostly ice.

Before considering the responses to the dust perturbations in our seeding experiments, we need to evaluate the control simulations with respect to (i) cloud phase for Arctic lower tropospheric clouds, and (ii) ice crystal number in the upper troposphere:

(i) Figure 2.3.7 demonstrates that NorESM2.3 captures many of the key features of mixed-phase clouds in the Arctic. Consistent with the satellite observations, the model simulates liquid cloud tops down to temperatures of about -20 degrees C. Thereafter, the SLF drops off rapidly with decreasing temperature in both the model and observations, albeit faster in the model, until they both reach complete cloud top glaciation at temperatures between -40 to -35 degrees C.
For the cloud interiors (“bulk”), the model and observations agree that they should be mixed-phase in the entire temperature range between -40 and 0 degrees C, but NorESM2.3 appears to maintains too much liquid relative to ice for the warmer mixed-phase cloud temperatures (above -20 degrees C). The model qualitatively reproduces the SLW contrast between cloud top and bulk, but it seems to be stronger in the observations. That being said, the model’s vertical resolution is coarser than that of the satellite retrievals, which could explain some of the discrepancies. All in all, NorESM2.3 appears to simulate Arctic mixed-phase quite realistically, which means that we can have some confidence in its simulation of Arctic mixed-phase clouds’ response to INP perturbations in the form of mineral dust injections. However, follow-up research could focus on achieving even better agreement between simulations and satellite observations, and from obtaining SLF from a second independent observational data set from EarthCARE (using ATLID, a spaceborne lidar comparable to CALIOP) in order to increase confidence in the observed phase.

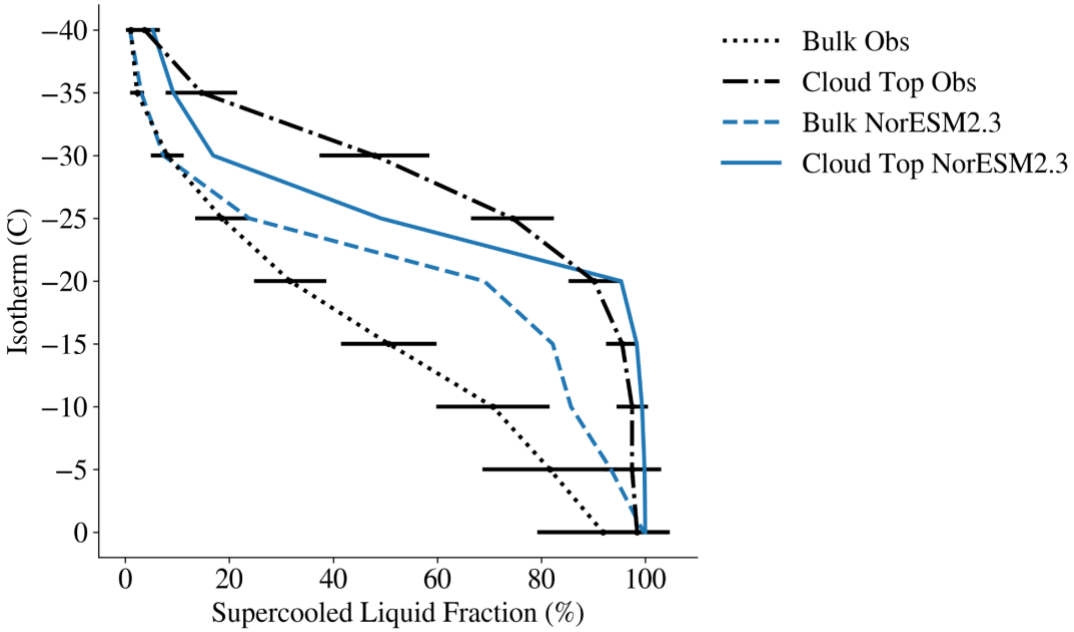

Figure 2.3.7: Cloud phase vs. temperature for Arctic mixed-phase cloud tops (north of 60°N) from CALIOP (dot-dashed line, “Cloud Top Obs”) and NorESM2.3 simulations (solid blue line), and for mixed-phase cloud bulks from CALIOP (dotted line, “Bulk Obs) and NorESM (blue dashed line).

(ii) Figure 2.3.8 shows ice crystal number concentrations from the control NorESM2.3 simulations. Here we follow Mitchell et al. (2018), see Figure 2.3.2 in this report, and plot the median ice crystal number concentration for gridboxes with air temperature between 218 and 228 K (-55 to -45°C). Similar to Mitchell et al.'s satellite retrievals (Figure 2.3.2), we see increased ice number concentration over mountainous regions in our NorESM2.3 simulations, especially in Asia. We also see an increase at the sub-polar latitudes compared to the sub-tropical latitudes, although it is not as pronounced as reported by Mitchell et al. Unlike the satellite retrievals, the NorESM2.3 simulations show ice crystal number concentration maxima in the tropics and, more importantly for this report, too low concentrations in the polar regions. As discussed above, the Arctic upper troposphere is relatively dust rich and supersaturation is uncommon in our NorESM2.3 simulations. This indicates that the simulated Arctic cirrus formation might primarily be through heterogeneous freezing, resulting in fewer but larger ice particles than if homogeneous freezing dominated. This discrepancy between our NorESM2.3 simulations and Mitchell et al. satellite retrievals might prove important for the results of our experiments (which revolve around seeding Arctic cirrus clouds with mineral dust) and needs to be better understood. Follow-up research in this direction would be highly beneficial and help better contextualize our results presented below.

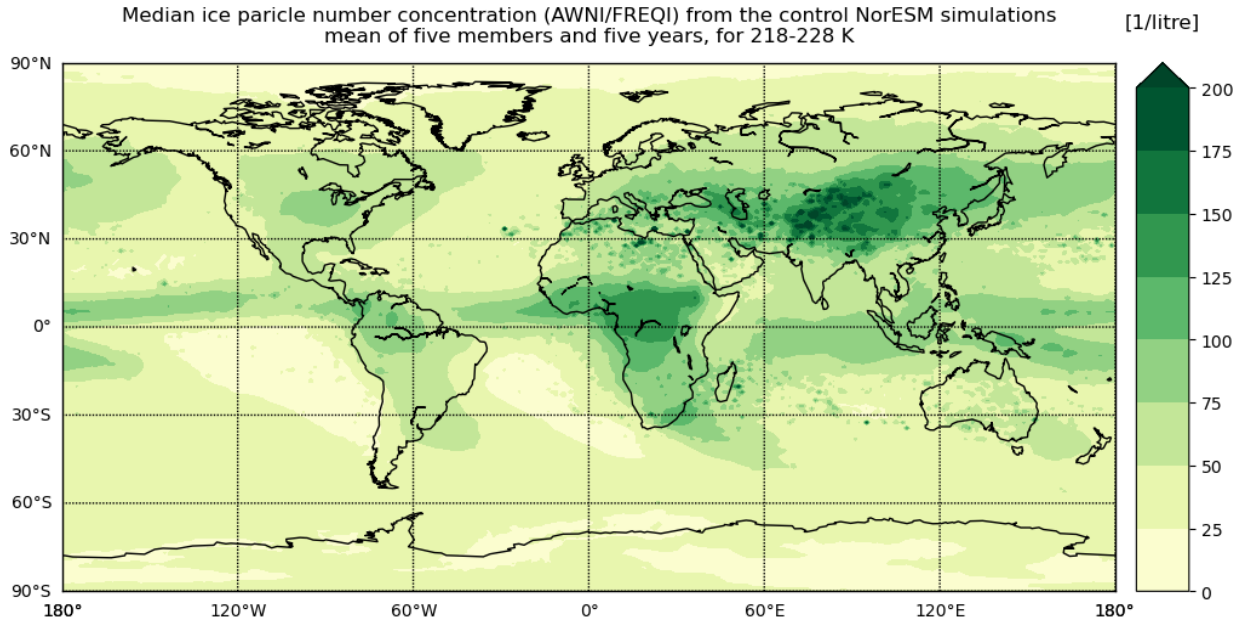

Figure 2.3.8: Ice crystal number concentration from the NorESM2.3 control simulations. Plotted here is the median concentration from a five-member ensemble mean for gridcells with air temperature between 218 and 288 K (see Figure 2.3.2 above).

2.3.4 Results: Anomalies

Since mineral dust mainly acts as INP, it does not directly stimulate liquid droplet formation. And since there is very little liquid water in the Arctic clouds throughout the atmospheric column during winter, additional INP's do not stimulate the growth of ice particles at the expense of liquid particles. The result is negligible liquid response to either seeding at 1 km or 7 km (Figure 2.3.7).

The idea behind cirrus cloud thinning is that by seeding ice nucleating particles in the cold upper troposphere, we would encourage cirrus formation through heterogeneous nucleation instead of homogeneous freezing. This should lead to larger ice particles which fall out quicker, reducing the lifetime of the cirrus clouds. However, as mentioned in the discussion of the simulated background conditions, it is unlikely that cirrus formation in the upper troposphere during the Arctic winter is aerosol limited. This is evident in Figures 2.3.8a and 2.3.8b where we see very limited cirrus cloud response to dust seeding at 7 km.

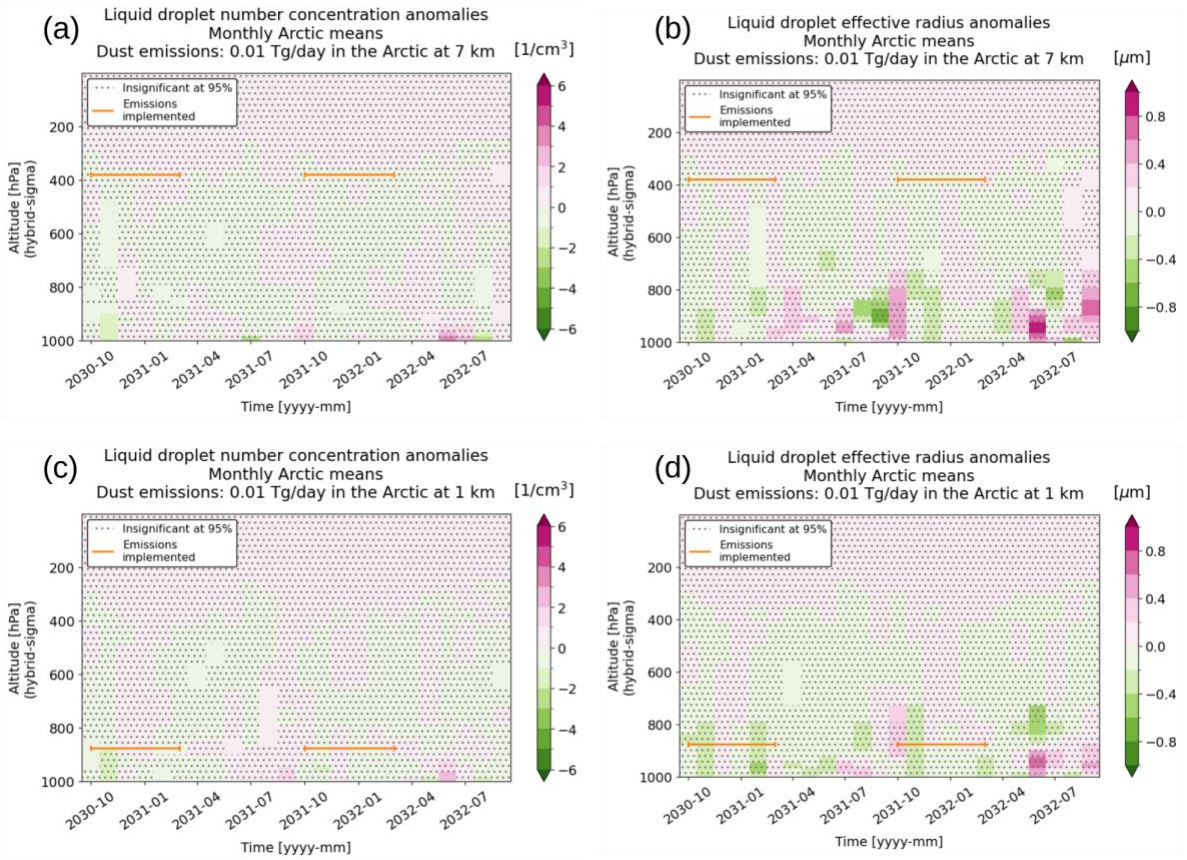

Figure 2.3.7: Monthly vertical sections of Arctic mean (north of 70°N, excluding land) liquid cloud droplet anomalies from the NorESM2.3 simulations. Panels (a) and (b) show liquid droplet number concentration and effective radius respectively for the 7 km seeding experiments, and (c) and (d) corresponding anomalies for the 1 km seeding experiments. Dotted regions indicate that anomalies are insignificantly different from zero at the 95% confidence level based on a two-tailed t-test.

Figure 2.3.8: Monthly vertical sections of Arctic mean (north of 70°N, excluding land) cloud ice crystal anomalies from the NorESM2.3 simulations. Panels (a) and (b) show ice number concentration and effective radius respectively for the 7 km seeding experiments, and (c) and (d) corresponding anomalies for the 1 km seeding experiments. Dotted

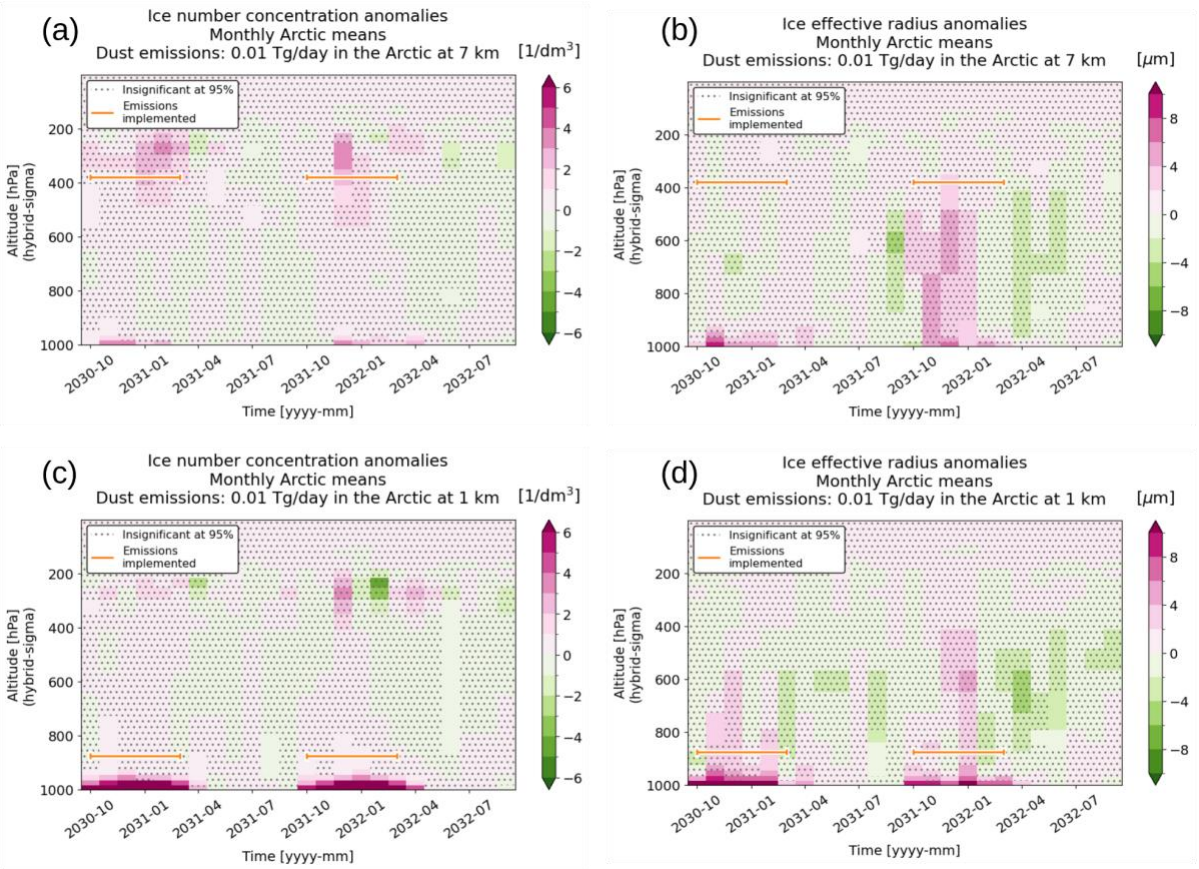

regions indicate that anomalies are insignificantly different from zero at the 95% confidence level based on a two-tailed t-test.

When seeding at 1 km, the model shows a strong significant increase in ice crystal number and size in the surface inversion layer (Figures 2.3.8c and 2.3.8d). This is accompanied by a significant drop in relative humidity (Figure 2.3.9c) and significantly increased cloud fraction (Figure 2.3.9d), indicating that the wintertime surface inversion layer is indeed aerosol limited and that adding aerosols stimulates the formation of more clouds.

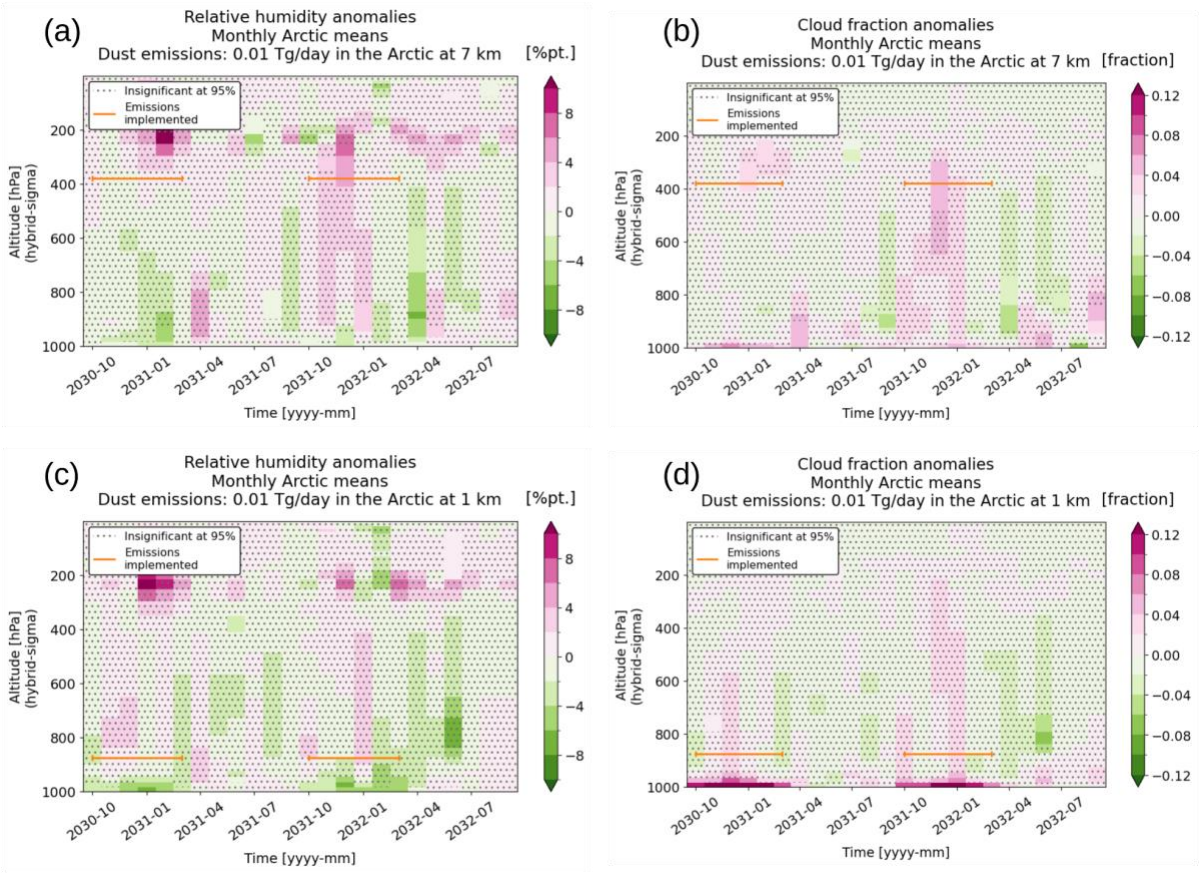

Figure 2.3.9: Monthly vertical sections of Arctic mean (north of 70°N, excluding land) relative humidity (a and c) and cloud fraction (b and d) anomalies from the NorESM2.3 simulations. The upper and lower panels respectively show results from the 7 km and 1 km seeding experiments. Dotted regions indicate that anomalies are insignificantly different from zero at the 95% confidence level based on a two-tailed t-test.

Based on the cloud response discussed above, we should expect negligible impacts on Arctic mean surface climate parameters in the 7 km experiments. This is indeed the case (see cyan lines in Figure 2.3.10). The increased low level ice cloud amount in the 1 km seeding experiment might, on the other hand, lead to surface warming during the seeding period through increased trapping of longwave (LW) radiation close to the surface. Downward LW flux anomalies at the surface are a good indicator of changes in the emissivity of low lying clouds, but here we see no robust response (Figure 2.3.10b). It follows that no robust surface air temperature response can be seen in the model results (Figure 2.3.10a) and sea ice remains mostly unaffected (Figure 2.3.10c). Note that although the ensemble mean temperature and radiation responses in Figure 2.3.10 are ambiguous, we do see a large spread between different ensemble members during periods of seeding, evident through the wide confidence intervals.

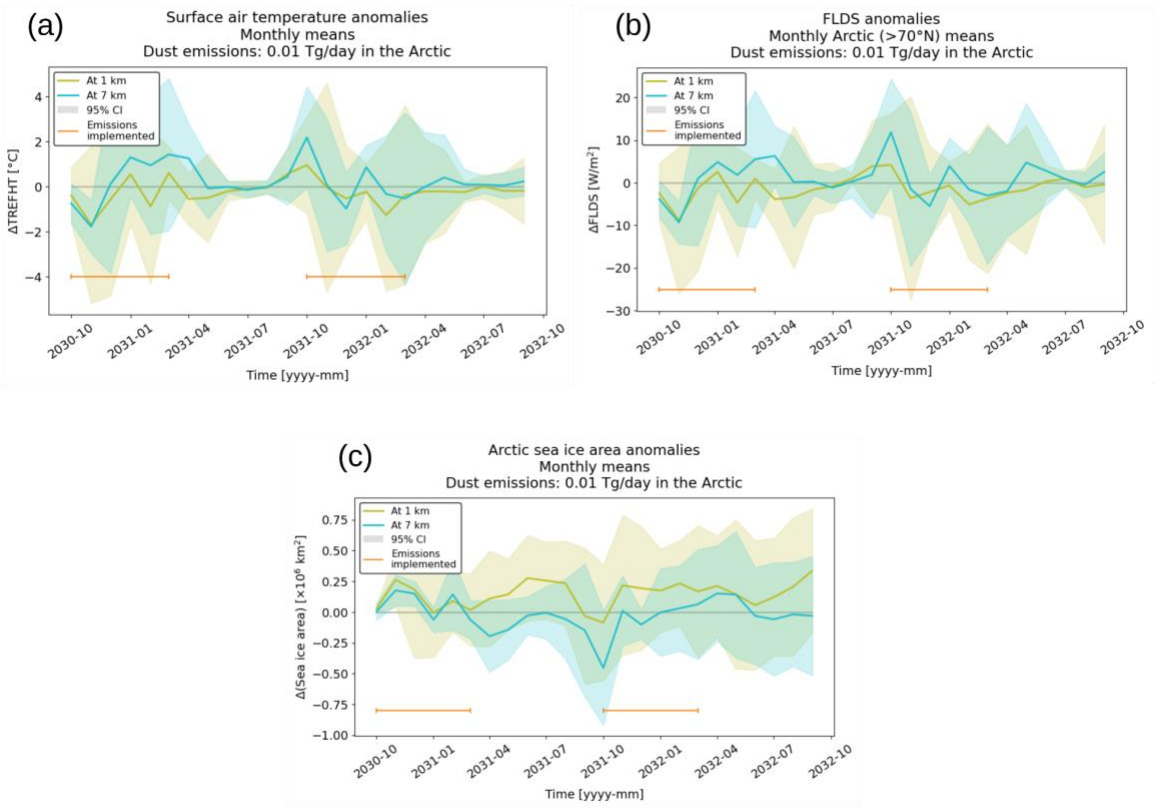

Figure 2.3.10: Monthly Arctic mean (north of 70°N, excluding land) anomalies for (a) surface air temperature, (b) longwave downward surface radiation (FLDS), and (c) sea ice area from the NorESM2.3 simulations. Shaded regions indicate 95% confidence intervals based on a two-tailed t-test.

2.3.5 Discussion

Our results indicate that the present day Arctic winter climate is not sensitive to moderate perturbations in INP levels. Hence climate intervention through seeding of ice or mixed-phase clouds by mineral dust (or similar aerosols which can function as INPs) might prove ineffective over the sea ice in the central Arctic. Our results indicate that mineral dust seeding in the Arctic upper troposphere during winter would lead to either no impacts on cirrus clouds or increased cirrus lifetime, leading to unaffected or more extensive cirrus clouds. Our results further indicate that seeding in the lowermost troposphere might stimulate more ice cloud formation in the surface inversion layer with no impacts on cloud liquid water, resulting in more low level clouds overall. This does, however, not lead to a clear temperature response in our simulations.

The results presented above are novel in the sense that (to our knowledge) no other ESM study of MCT or CCT has actually injected INPs into the Arctic troposphere and simulated their atmospheric life cycle. Instead, a common practice has been to assume a certain

uniform concentration of seeding particles, which is far from realistic. However, it must be noted that the results presented above are not yet entirely conclusive. Below follows a list of topics that should be expanded on in follow-up research:

- In order to better constrain the signal from the dust seeding experiments, we need more ensemble members. We currently have five but should ideally expand to ten.
- Our current simulations cover two winters but we need a longer period in order to detect potential emerging impacts. We would ideally like to extend our simulations to cover five consecutive winters.
- Comparisons of NorESM2.3 output with satellite retrievals of cloud phase (critical for MCT) and upper tropospheric ice crystal number (critical for CCT) show reasonable agreement. However, future work should ideally obtain these quantities also for a second observational data set (e.g. from EarthCARE retrievals). Additionally, small model adjustment could likely yield even better comparison between the simulations and observations.
- To reach firm conclusions about CCT and MCT viability in the Arctic, we should explore the impacts of different seeding rates. Based on the results presented above, we suggest adding simulations with considerably higher seeding rates.
- So far, our focus has been on the sea ice covered central Arctic during winter. As discussed above, the background atmospheric state is very important when it comes to the potential impacts of climate intervention through cloud seeding. Atmospheric conditions are very different between the sea ice in the central Arctic and over the open ocean off the sea ice edge, not least when it comes to clouds. A more regional analysis of our data would therefore be beneficial. In particular, the response in the sub-arctic region should be better explored.

2.4 Photovoltaic (PV) potential under SAI - WP2400/3400

2.4.1 Objectives

This WP aims to couple radiative flux perturbations induced by SAI with photovoltaic (PV) yield modelling, moving beyond standard PV performance indicators to assess their impact on electricity generation and to explore mitigation through optimized PV system design. Kumler et al. (2025) has synthesized previous literature on the possible effects of climate change and SRM on renewable energy resources (i.e., wind energy, solar energy, biomass energy, and hydropower). They have focused on the continental United States but offered a global perspective as well. Their framework is reproduced on Figure 2.4.1 identifying both direct and indirect impacts of SRM on renewables. However, they mostly identify relevant meteorological variables that may be affected and their projected qualitative changes. Previous studies on the impact of SAI on PV resources have used fairly simple models of PV production (Smith et al., 2017; Hou et al., 2021; Baur et al.,

2024; see also blog post[4]) and have not sought to optimize the tilt or the density of the PV panels to the new solar irradiance conditions.

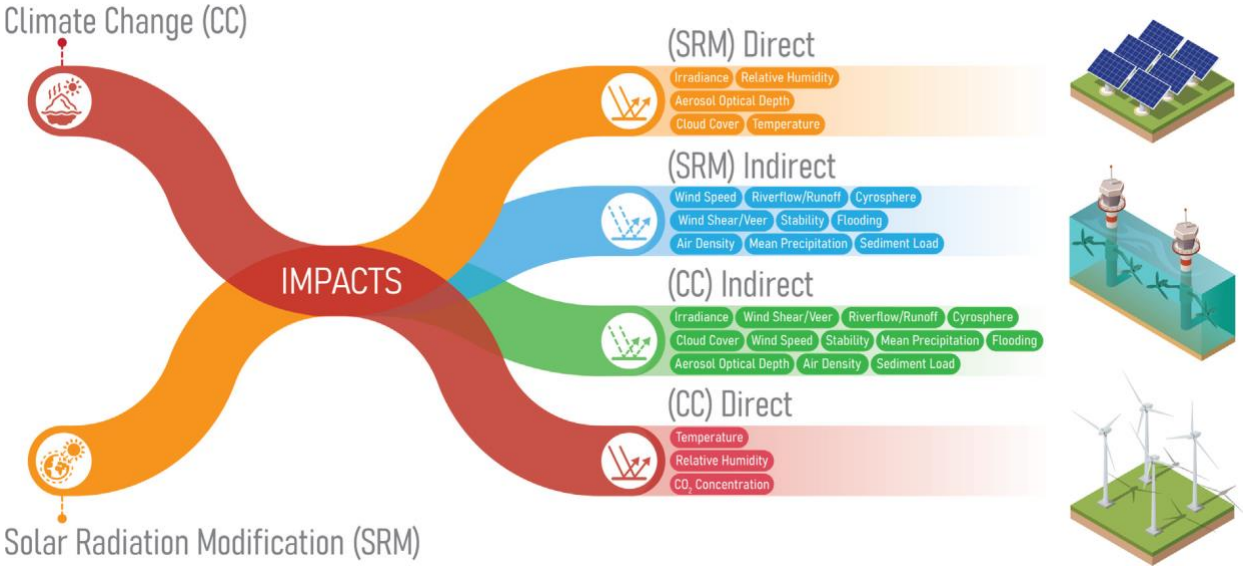

Figure 2.4.1: Pathways whereby SRM and climate change impacts renewables (including PV production). Reproduced from Kumler et al. (2025).

Detailed radiative transfer calculations are needed to better simulate the irradiance intercepted on a tilted or vertical surface and/or to convert global horizontal irradiance (GHI; see section 2.4.6 for the definition) to a flux on a tilted surface. Indeed, many PV calculations simply assume that the diffuse horizontal irradiance (DHI) is isotropic so that the diffuse irradiance intercepted by a tilted surface is approximated by DHI x (1 + cos β) / 2 where β is the tilt angle of the PV panel and DHI is the diffuse irradiance on a horizontal surface. Only a limited amount of data is available to validate such transformation according to the aerosol load (Raptis et al., 2017; Elias et al., 2024).

A further objective of WP2400 will be to mitigate the reduction in surface radiation by changing the tilt and density of PV panels at the surface. We will also investigate different designs of a PV farm (e.g., fixed panels and/or one-axis trackers) for a one-year time series of surface radiation. This work will initially be performed in clear-sky conditions or by assuming that SAI does not induce any change in cloudiness.

The primary objectives of WP2400 require to better document clear-sky solar radiation at the surface under SAI using **benchmark radiative transfer calculations**.

[4] https://srm360.org/article/sai-and-renewable-energy/

A secondary objective of this activity would be to contribute to WP2100/WP3100 by looking at the potential issue of a large heating rate found in some climate models in response to stratospheric sulphate aerosols. It will provide a benchmark which can be compared to stand-alone radiative transfer model calculations such as RRTM at a later stage.

2.4.2 Initial protocol for benchmark radiative transfer calculations

This will be performed through a small intercomparison study using a prescribed protocol that features a vertical profile of T and q from a mid-latitude summer (MLS), CAMS tropospheric aerosol profile, and an additional stratospheric aerosol layer with prescribed optical properties (e.g., aerosol size distribution, spheres, spectral refractive indices). The plan involves conducting simulations across a range of surface albedos and solar zenith angles (SZA). The spectral and directional radiation at the surface (radiances) resulting from these simulations must be documented. The possibility of extending the simulation period to a full year should also be explored, if technically feasible.

Protocol:

Vertical profiles (T, q, ozone and other gases, background aerosols) from CAMS
Mid-latitude summer, e.g., 1st July 2024, 12:00 UTC at latitude = 45°N, longitude = 0°
Clear-sky (no clouds). Optional: 1st Jan, 1st April, 1st October 2024.
Solar zenith angles for SW calculations: 0° to 80° by step of 10°
Surface for SW: Lambertian surface with albedo of 0.05 and 0.20 (no spectral variation)
Surface for LW: unit emissivity, surface temperature from CAMS
Simulations to be done with and without a stratospheric aerosol layer

- Lognormal aerosol size distribution
- Mode radius r_0 = 0.12 µm, geometric standard deviation σ_g = 1.60
- Liquid homogeneous spherical particles made of sulphuric acid (+H_2O)
- Density = 1.76 g.cm^{-3}
- Particle column concentration: 10^{10} and 10^{11} particles / m^2
- Vertical profile: centered around 19 km altitude (e.g., between 18 and 20 km)
- Complex refractive index from file refractive_index_H2SO4_RH75_300K.csv
  https://thredds-su.ipsl.fr/thredds/catalog/ipsl_thredds/oboucher/STATISTICS/catalog.html

Total number of cases (SW): 9 SZA x 2 albedos x 2 concentrations = 36 cases
Total number of cases (LW): 2 concentrations = 2 cases

Outputs (depending on model capability)
Stratospheric aerosol optical depth at 550 nm (and 10 µm)
Monochromatic surface and top-of-atmosphere radiance fields at 550 nm (Wm^{-2}sr^{-1}µm^{-1})
Broadband surface (direct and diffuse) and top-of-atmosphere fluxes (Wm^{-2})

Broadband surface diffuse flux (Wm^{-2}) on a tilted surface
If possible: vertical profile of heating rates (°C/day)

Participating radiative transfer (RT) models:
SW: libRadtran, GRASP
SW, LW: libRadtran, PMODWRC

2.4.3. GRASP Radiative Transfer calculations and CAMS Aerosol Modeling

The Generalized Retrieval of Aerosol and Surface Properties (GRASP) is a sophisticated and highly flexible numerical platform designed for the comprehensive retrieval of atmospheric and surface properties from various remote sensing observations, particularly in the solar spectral range. Developed and maintained by the GRASP-SAS community, the core of the GRASP system lies in its implementation of the radiative transfer (RT) equation using the computationally efficient Successive Order of Scattering (SOS) method (Dubovik et al., 2011, 2021). This technique allows GRASP to accurately calculate the propagation of radiation through an aerosol-laden atmosphere for a wide range of observational geometries and surface types. GRASP's advanced architecture enables it to perform both forward model calculations, i.e., simulating expected radiation fields given known atmospheric inputs, and inversions, which involves numerically optimizing the retrieval of numerous aerosol and surface parameters simultaneously from diverse measurements, such as those from spaceborne multi-angular, multi-spectral, and polarimetric instruments. Its robust mathematical core, coupled with its capability to handle complex aerosol microphysical properties (size distribution, shape, spectral refractive indices) and varying surface conditions, makes GRASP a widely used and validated tool in the atmospheric science community for aerosol remote sensing and broadband flux studies.

The implementation of the CAMS aerosol microphysical model (Bozzo et al., 2020) within the GRASP RT framework (cf., Derimian et al., 2016) is a critical step for accurately modeling broadband flux parameters. This is to provide a realistic, externally mixed, spectrally defined background atmosphere, upon which the fixed-property SAI aerosol layer is superimposed for the two-scenario comparison. The GRASP RT simulations leverage the CAMS reanalysis data, which uses the tropospheric aerosol scheme of the European Centre for Medium-Range Weather Forecasts (ECMWF) Integrated Forecasting System (IFS-AER, cycle 42R1) (Rémy et al., 2019; Bozzo et al., 2020). This scheme models the global atmospheric state and provides the necessary background aerosol concentrations for GRASP RT simulation. The gas profiles are based on the US standard 1976 atmospheric concentrations.

The CAMS scheme internally tracks the mass-mixing ratios of 11 prognostic aerosol species, which GRASP ingests as (vertically stratified) volume concentrations for RT calculations:

- **Dust:** 3 size bins (DU1, DU2, DU3)
- **Sea Salt:** 3 size bins (SS1, SS2, SS3)
- **Carbonaceous:** Hydrophobic Black Carbon (BC1), Hydrophilic Black Carbon (BC2), Hydrophobic Organic Matter (OM1), Hydrophilic Organic Matter (OM2)
- **Sulphate:** (SU)

Each of these species is defined by fixed microphysical properties within the GRASP RT simulation, ensuring consistency with the standard CAMS framework for aerosol transport and composition. This RT model treats the CAMS aerosol species as an **external mixture**. This means that each of the 11 aerosol species (e.g., DU1, SU) is considered to exist as a separate population of particles within the same atmospheric column. The total radiative effect is calculated by summing the contributions of light scattering and absorption from each individual, independently characterized particle type.

To ensure a stable and consistent radiative simulation, the refractive indices (both real and imaginary parts) for all 11 CAMS aerosol components are **fixed** for the simulations. These values are derived from a compilation of literature and standard datasets (e.g., Dubovik 2002; Hess 1998, Bozzo et al., 2020) and are **spectrally dependent**, as shown in Table A1. The refractive indices used here are more accurate, incorporating insights gained from satellite retrieval data, in contrast to those employed in the CAMS model's Cy42R1 version (used in reanalysis).

Each of the CAMS aerosol species is represented by a specific, fixed log-normal size distribution or by a set of modes that define the bins for species like dust and sea salt (Fig. 2.4.2). These size distributions dictate how the total columnar concentration of mass is distributed across different particle radii, which is crucial for determining scattering efficiency and phase functions in the GRASP RT calculation.

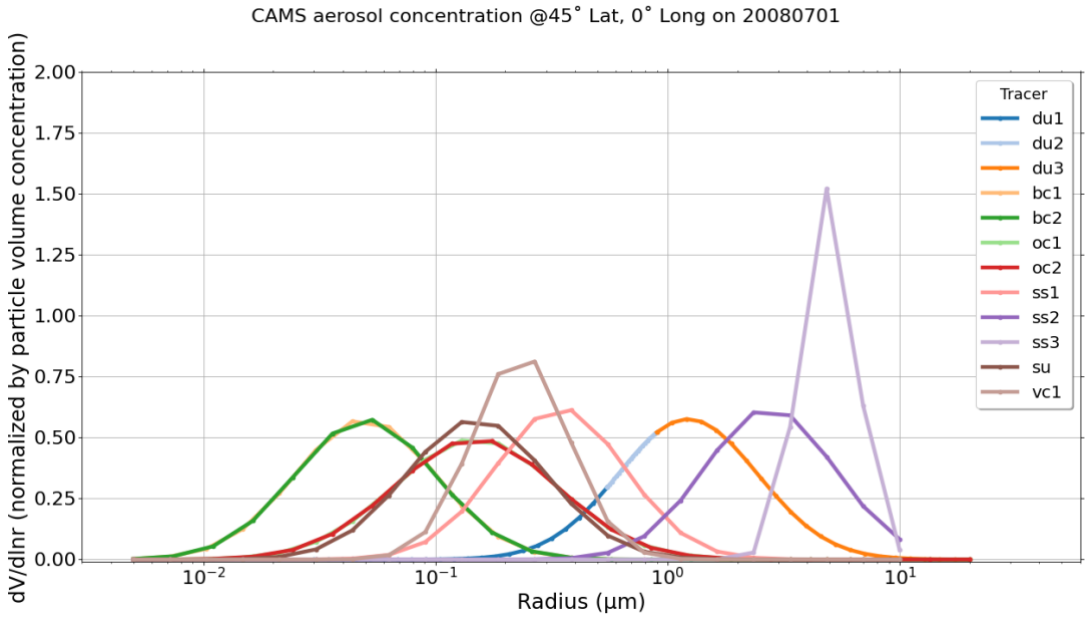

Figure 2.4.2: Dry aerosol species size distribution used in the GRASP RT model, derived from the bulk aerosol modeling scheme of ECMWF's CAMS transport model (Rémy et al., 2019; Bozzo et al., 2020). They are categorized as follows: DU1 [0.03–0.55 μm], DU2 [0.55–0.9 μm], DU3 [0.9–20 μm], BC1 (hydrophobic, [0.005–10.0 μm]), BC2 (hydrophilic, [0.005–20.0 μm]), OM1 (hydrophobic, [0.005–10.0 μm]), OM2 (hydrophilic, [0.005–20.0 μm]), SS1 [0.005–0.5 μm], SS2 [0.5–5.0 μm], SS3 [5.0–20.0 μm], and SU [0.005–10.0 μm]).

A key aspect of the CAMS aerosol modeling, particularly for the hydrophilic components (e.g., SU, BC2, OM2, and SS), is the dependence of their size and refractive index on ambient relative humidity (RH). In the CAMS model, aerosols undergo **hygroscopic growth**. This growth alters their light scattering and absorption properties, a change that is then accounted for in the GRASP RT model.

For the baseline GRASP simulations using the CAMS aerosol background (Scenario 1), the aerosol profiles are ingested from CAMS, where the vertical distribution of mass and size distribution are already taken from the CAMS RH values and hygroscopic growth scheme. For the SAI scenario (Scenario 2), which uses a synthetic SU profile, the protocol explicitly states that the SAI particles (SU) are modeled without subsequent hygroscopic growth despite being based on a 75% sulfuric acid assumption. This is a simplification to isolate the direct SAI radiative effect.

Aerosol Type	Mixing Assumption in GRASP	Size Distribution	Refractive Index	Hygroscopic Growth in SAI Component

CAMS (11 Species)	External	Fixed (Log-Normal/Bins)	Fixed (Table A1)	Implicit in CAMS input data
SAI (Sulfate)	External	Fixed (Log-Normal)	Fixed (Table A1)	**Not Considered** (Fixed properties)

Table 2.4.1: CAMS aerosol microphysics. This table serves as the basis for the estimation of broadband flux parameters.

The calculation of the total column Aerosol Optical Depth (AOD) is a complex process that integrates multiple interdependent aerosol properties and RT principles. This estimation fundamentally relies on the assumption of an external mixture for each distinct aerosol (chemical component) type present in the atmospheric column (Li et al., 2019). This external mixing rule simplifies the combined effect of multiple aerosols, such as DU, SS, SU, BC, and OM, on the light extinction process. To accurately model this mixture's radiative impact, several critical parameters specific to each aerosol component must be incorporated:

1. **Size Distribution:** The geometric properties of the aerosols, specifically their size distribution (as conceptually illustrated in Fig. 2.4.2), are crucial. This distribution dictates how efficiently an aerosol particle scatters and absorbs incoming radiation.
2. **Refractive Indices:** The refractive indices (as detailed in Table A1) define the intrinsic optical properties of the aerosols. The real part governs the scattering efficiency, while the imaginary part determines the absorption capacity.
3. **Vertical Distribution:** The concentration profile of the aerosol types throughout the atmospheric column is accounted for. This vertical distribution (ingested from CAMS) is essential because the atmospheric density and pressure—and thus the scattering environment ($< C_{v\,sc}^{(k)} >$ and $< C_{v\,ext}^{(k)} >$) —change significantly with altitude.
4. Tracer-Averaged Phase Function ($< P_k >$): Considering the vertical distribution, a tracer-averaged phase function (external mixture) must be calculated. The phase function describes the angular distribution of scattered light. This averaging ensures the representative optical properties reflect the true vertical stratification of the aerosol types.

These properties are then used to calculate a set of spectrally-dependent optical parameters for the entire column for a single pixel:

$$< P_k > = \frac{\int_{z_1}^{z_{l_{max}}} P_k(z\prime) C_{v\,sc}^{(k)}(z') c_v^{(k)}(z') dz'}{\int_{z_1}^{z_{l_{max}}} C_{v\,sc}^{(k)}(z') c_v^{(k)}(z') dz'} \qquad \text{(Eq. 2.4.1)}$$

$$< C_{v\,sc}^{(k)} > = \frac{\int_{z_1}^{z_{l_{max}}} C_{v\,sc}^{(k)}(z') c_v^{(k)}(z') dz'}{\int_{z_1}^{z_{l_{max}}} c_v^{(k)}(z') dz'}, \qquad \text{(Eq. 2.4.2)}$$

$$< C_{v\,ext}^{(k)} > = \frac{\int_{z_1}^{z_{lmax}} C_{v\,ext}^{(k)}(z') c_v^{(k)}(z') dz'}{\int_{z_1}^{z_{lmax}} c_v^{(k)}(z') dz'} \qquad \text{(Eq. 2.4.3)}$$

The following terms are defined with respect to aerosol type *k*:

- $< P_k >$ denotes the tracer-averaged phase matrix (for external mixture).
- $< C_{v\,sc}^{(k)} >$ denotes the scattering cross-section in total column volume concentration.
- $< C_{v\,ext}^{(k)} >$ denotes the total extinction cross-section in total column volume concentration.

The final estimation of the total column AOD ($\boldsymbol{\tau}(\lambda)$) is the integration of these extinction properties over the entire vertical column, serving as a dimensionless measure of the total aerosol load.

2.4.4 Uncertainties Associated with GRASP-based Broadband Flux

The uncertainties in the GRASP RT model's calculations of broadband flux originate from two primary areas, which are detailed in the table below.

Parameter Category	Specific Parameter	Description of Uncertainty Source	GRASP Implementation/Context
Aerosol Microphysics (CAMS Background)	Size Distribution & Effective Radius	Fixed (log-normal/binned) properties may not reflect the actual atmospheric variability and evolution of the aerosol sizes	Fixed properties derived from CAMS scheme; external mixture assumption.
	Complex & Real Refractive Indices	Fixed spectral indices are used, simplifying the intrinsic optical properties of particles, especially under varying environmental conditions	Values are fixed and spectrally dependent, interpolated from source data.
	Hygroscopic Growth	Explicit in CAMS input data, but the fixed-property assumption in GRASP RT post-ingestion may not capture dynamic size and refractive index changes	Considered explicitly as in CAMS model
	Vertical Distribution	Resolution and accuracy of the CAMS spatial (0.75°x0.75° resolution) and vertical stratification (25 layers from surface till 0.1 hPa) influences the calculated atmospheric path length and scattering environment	Vertical mass mixing ratio profiles are ingested from CAMS reanalysis

Parameter Category	Specific Parameter	Description of Uncertainty Source	GRASP Implementation/Context
	Total Column Values	Total column amount, ingested from CAMS, carries the reanalysis uncertainty, impacting the overall AOD and radiative effect	Based on CAMS data; SAI injection set to a fixed concentration (e.g., ~10^{11} particles/m^2).
	Gas absorption	US Standard atmosphere 1976	Fixed total column values
Radiative Transfer Limitations	Spectral Feature Interpolation	Aerosol optical properties are interpolated linearly between a limited number of spectral bands (e.g., in Table A1), potentially missing fine spectral structure	Broadband flux is calculated over 0.4 - 4.0 µm, relying on linearly interpolated optical properties
	Integration Range Truncation	Limitations in obtaining accurate optical properties for large particles (e.g., sea salt) and shortwave absorption/scattering leads to narrowing the spectral integration window (e.g., from 200 nm to 400 nm).	Theoretical range is 200 nm to 4.0 µm; practical range is often constrained here to 400 nm to 4.0 µm.

Table 2.4.2: This table presents a summary of potential uncertainties and their associated parameters.

2.4.5 GRASP RT simulation over Puynormand, France

The baseline RT simulation is conducted following the predefined protocol. Here, the focus is on a specific pixel located at Puynormand, France (45˚N, 0˚E), on July 1, 2008. This date and location are chosen for their clear-sky conditions and with minimal background aerosol loading, specifically an AOD at 550 nm of 0.092, as determined by CAMS reanalysis. The year 2008 is chosen to work with primarily because CAMS reanalysis data was readily available during the initial development phase.

RT simulations for the initial testing and development phase focus on assessing the sensitivity of net radiative forcing to SU aerosol injection heights. This assessment uses four distinct SU injection profiles—VC1 (5km), VC2 (7km), VC3 (15km), and VC4 (30km)—which are differentiated solely by their injection altitude above sea level (ASL). These simulations exclude calculations for diffused flux and tilted surfaces. Fig. 2.4.2 indicates the size distribution of the injected SU particles (e.g., VC1, light brown profile). In line with the protocol, hygroscopic growth is not considered, regardless of whether the injection height is in the troposphere or the stratosphere. The four chosen Gaussian injection profiles, as shown in Fig. 2.4.3, have a standard deviation of 2 km. Each synthetic Gaussian profile is designed to have a total column concentration 30 times greater than the background level (CAMS/SU: Fig. 2.4.3, in blue left panel), amounting to

approximately 4 X 10^{11} particles.m^{-2}. This specific number is selected to align with the concentration level stipulated in the protocol. Based on assumed values for the refractive index, density, and effective radius, these profiles collectively resulted in an AOD of 0.8383 at 555 nm, leading to a total column AOD of 0.9143 at the same wavelength. The RT simulations cover solar zenith angles (SZA) from 0° to 80° in 10° steps and apply two Lambertian surface parameters (spectrally flat). We calculate upward and downward broadband fluxes and derive net aerosol forcing (radiative effect) vertical profiles surface till 40 km ASL.

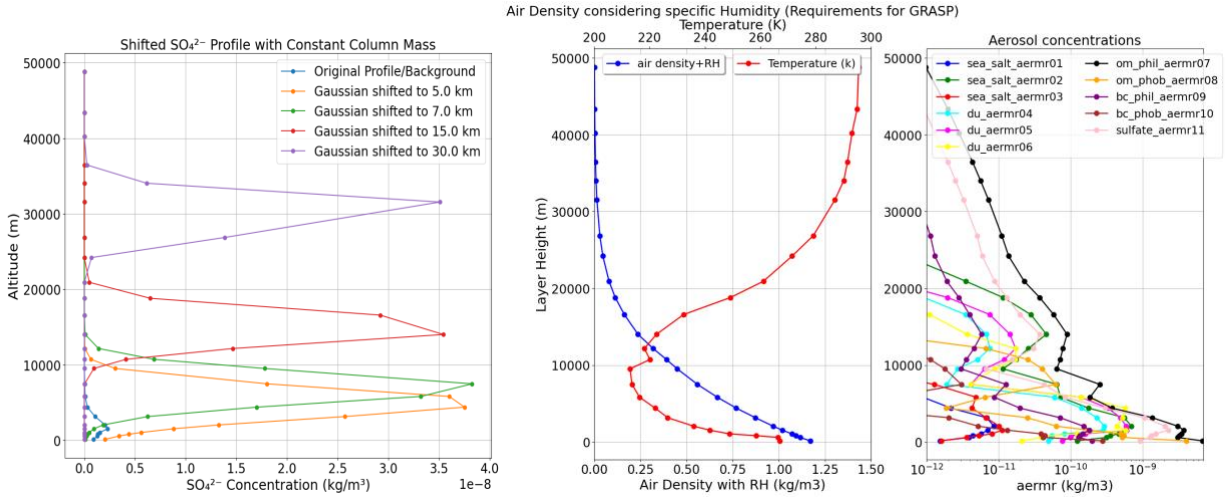

Figure 2.4.3: The background SU aerosol vertical profile (blue, left panel) from CAMS (Cy42R1) reanalysis data at the selected pixel on 2008-07-01. It also presents four synthetic sulphate aerosol profiles, each with a Gaussian peak at 5 km (orange), 7 km (green), 15 km (red), and 30 km (violet). The middle and right panels show the vertical profiles of air density, temperature, and other background aerosol concentrations, respectively.

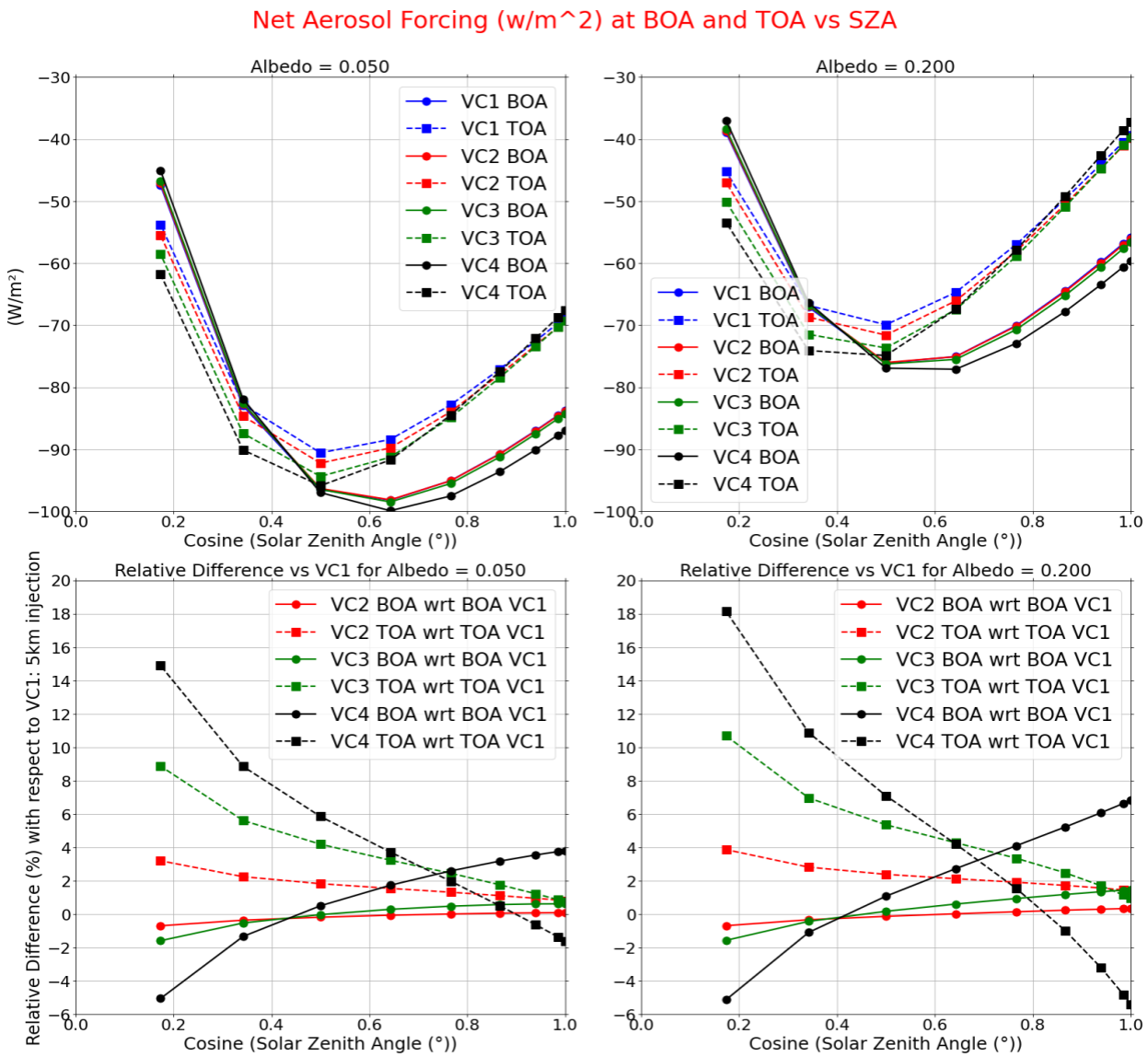

Figure 2.4.4: Net aerosol forcing at the bottom (BOA, solid lines) and top (TOA, dotted lines) of the atmosphere, shown for nine solar zenith angles. The lower panels show relative percentage changes at BOA and TOA, using the 5 km injection profile as reference. The *x*-axis represents the cosine of the SZA.

Fig 2.4.4 illustrates the instantaneous net aerosol radiative effect (W.m^{-2}) at the bottom of the atmosphere (BOA), which is defined as the difference between downwelling and upwelling fluxes with and without aerosols. Similarly, the net aerosol forcing at the top of the atmosphere (TOA) represents the difference in fluxes between aerosol-laden and clean atmospheric conditions (Derimian et al., 2016). The simulation retains background aerosol vertical concentrations (11 species) from the CAMS reanalysis, alongside synthetic SU injections. The key findings shown in Fig. 2.4.4 are:

- **BOA Fluxes:** Aerosol injections confined to the troposphere (VC1 and VC2) affect BOA fluxes by approximately 2% across the scenarios. In contrast, SAI can at least double the influence on surface-level flux. The SZA also plays a role in the effect observed.
- **TOA Forcing:** A direct relationship is observed: a higher aerosol injection layer ASL results in a stronger cooling effect at the TOA.

In conclusion, at this stage of the study, we investigated the impact of aerosol injections at various altitudes on surface broadband radiation, with significant implications for the solar energy sector.

Modelled as hydrophobic SU aerosols, tropospheric injections at a 7 km altitude demonstrates a measurable change in surface broadband radiation, showing up to a 2% variation when compared to an injection at 5 km. This difference, although seemingly small, holds considerable importance for solar energy production. PV panels and concentrating solar power systems rely directly on the amount of incident solar radiation (insolation); even minor variations in the sunlight reaching the surface can critically affect panel efficiency and, consequently, the overall energy yield. A persistent 2% reduction or increase in insolation could necessitate a re-evaluation of installed capacity and financial projections for solar farms.

In contrast to the tropospheric findings, stratospheric injections—specifically modelled at 15 km and 30 km—show a much greater variability in surface level radiation. The magnitude and nature of these radiative changes are found to be complex, highly influenced by three key factors:

- **Injection Height:** The altitude of the SU aerosol layer significantly determines its persistence, dispersion, and optical properties, leading to different scattering and absorption effects on incoming solar radiation.
- **Surface Type (Albedo):** The reflectivity of the surface (e.g., ocean, forest, desert, snow cover) plays a crucial role. For instance, high-albedo surfaces like snow or desert interact differently with scattered light than low-albedo surfaces like water, leading to localized variations in the net surface radiation balance.
- **Solar Zenith Angle (SZA):** The SZA, which describes the angle of the sun in the sky, modulates the path length of solar radiation through the aerosol layer. At high SZAs (early morning or late afternoon), the longer path length can amplify the dimming or scattering effects of the aerosols, increasing the overall variability observed at the surface.

This evidence strongly suggests that the altitude chosen for SRM or geoengineering efforts—particularly the injection of SU aerosols—plays a critical, non-linear role in dictating the resulting surface flux values, and thus the performance and output of solar

power generation systems.

2.4.6 Detailed Methodology and Dataset Description for broadband flux modeling

This section details the development and scope of the dataset used for modeling Global Horizontal Irradiance (GHI), Direct Horizontal Irradiance (DirHI), and Diffuse Horizontal Irradiance (DHI). Additionally, it includes a rigorous inter-comparison of **two RT models** with distinct architectures (GRASP and libRadtran). As discussed in section 2.4.1, here the goal is to provide a robust input for subsequent PV energy yield simulations.

The derived solar irradiance data (GHI, DirHI, DHI) will serve as the primary and foundational input for advanced, industry-standard PV energy modeling software and algorithms. This modeling step is crucial as it moves beyond simple irradiance metrics to calculate physical energy output. Specifically, the modeling process will involve:

1. **System Design Parameters:** Defining a representative set of PV system configurations, including panel tilt (VZA) and orientation (RAA) optimized for the SIRTA location's latitude.
2. **Performance Calculation:** Using the time-series irradiance data to simulate the hourly energy generation (kWh) of the defined PV systems under both the 'Baseline' and 'With SAI' scenarios.
3. **Comparative Yield Analysis:** The culmination of this effort is the accurate estimation and direct comparison of the potential annual energy yield and performance ratio of solar power installations.

I. Geographic and Temporal Scope

- **Location:** All calculations and data points are specifically generated for the **SIRTA** (Site Instrumental de Recherche par Télédétection Atmosphérique) station, located near Paris, France. This station serves as the ground truth location for the atmospheric and irradiance modeling.
- **Time Period:** The analysis covers the entire calendar year of **2024**.
- **Day Selection:** To focus the computational effort on periods most relevant for maximum solar energy potential, a selective sampling strategy is followed. For each month in 2024, only **two** distinct "clear sky" days are chosen (Table A2). This clear-sky selection ensures that the primary variations observed are due to aerosol and SAI effects, minimizing the influence of cloud cover.

II. Atmospheric Input Data

- **Aerosol Concentration:** The essential atmospheric background is established using aerosol concentration data ingested from the CAMS reanalysis datasets.

- **Temporal Resolution of Aerosols:** To capture the diurnal variability in aerosol loading, the CAMS data is used at a **3-hourly resolution** (this also represents the data availability resolution). The estimation of GHI, DirHI, and DHI is constrained by a SZA range of 10° to 80°. This range is used to avoid inaccuracies, such as those caused by a spherical atmosphere at very high SZA. Moreover, at such high latitudes, the SZA consistently remains above 30˚ during the day, never dropping below that value. The libRadtran runs are performed **hourly** by interpolating the CAMS/AERONET input.

III. Modeling Tools

The broadband flux parameters essential for this WP are derived using two different, independently developed RT models. These RT models are: GRASP, which uses the successive order of scattering method (Dubovik et al., 2011, 2021), and libRadtran (Library for Radiative Transfer), which uses the discrete ordinate method for radiative transfer (Mayer and Killing, 2005; Emde et al., 2016). This two-pronged approach involved collaboration between two separate research entities: GRASP Earth, a specialized private research institute responsible for the GRASP RT model and aerosol remote sensing, and PMOD/WRC (Physikalisch-Meteorologisches Observatorium Davos/World Radiation Center), which uses the libRadtran model.

GRASP's core application is the sophisticated retrieval of aerosol and surface properties from satellite data, focusing specifically on the **solar irradiance ranges** (shortwave radiation).

In contrast, the libRadtran radiative transfer model, is a versatile and open-source tool primarily designed for comprehensive solar and terrestrial flux evaluation purposes. A key distinction is that libRadtran covers both the **solar (shortwave)** and the **thermal (longwave) irradiance ranges**, allowing for a complete assessment of the Earth's radiation budget. In short, the program is a library of RT routines to calculate spectral irradiance in the UV and visible parts of the spectrum. It is a versatile tool providing a variety of options to set up and modify an atmosphere with molecules, aerosol particles, water and ice clouds. One of such setups is used here to mimic the SAI scenarios. LibRadtran also provides a program to calculate Mie scattering of aerosol particles. This option is used to calculate the optical properties of the sulfuric acid as SAI from the refractive indices, lognormal size distribution and effective radius as outlined above. In addition, we have used a tool ('angres') included in LibRadtran for calculating irradiance for tilted surfaces (i.e. PV panels), which takes a precalculated radiance field and integrates it over a given angular area using any angular response.

LibRadtran simulations employed almost the same CAMS (or AERONET) atmospheric inputs and solar geometry setup but with monthly climatological values for single scattering albedo (SSA) and asymmetry parameters (gg) taken from AEROCOM (MACCv2) **instead of** CAMS for these properties. The model comparison serves as a crucial cross-validation between two structurally different RT codes (**Successive Order of Scattering vs. Discrete Ordinate Method**). While GRASP's foundational purpose is aerosol remote sensing, LibRadtran's is the broader calculation of atmospheric radiative transfer and radiation fluxes. The usage of these two structurally different, yet highly validated, models provide a critical cross-check and adds significant confidence to the derived broadband flux parameters.

IV. Irradiance Parameters

The primary objective of the RT modeling is to estimate accurately the three key solar irradiance components:

1. **Global Horizontal Irradiance (GHI):** It represents the total amount of shortwave radiation received from the sun above a surface positioned horizontally to the ground. GHI is the integrated sum of radiant energy coming from the entire sky dome, which fundamentally comprises two components: the direct radiation component and the diffuse radiation component.
2. **Direct Horizontal Irradiance (DirHI):** It is defined as the downward direct flux per unit area for a surface positioned horizontally to the ground. It represents the component of solar radiation that travels directly from the sun to the Earth's surface after being scattered or absorbed by the atmosphere.
3. **Diffuse Horizontal Irradiance (DHI):** It is often referred to as Diffuse Irradiance, is the radiation that reaches the horizontal surface scattered by atmospheric constituents such as aerosols, clouds, and gas molecules. It comes from all directions in the sky, excluding the direct solar disk.

The fundamental physical relationship connecting these three components is known as the **closure equation**, which expresses the total irradiance on a horizontal surface as the sum of the direct and diffuse components:

$$GHI = DirHI + DHI \qquad \text{(Eq. 2.4.4)}$$

These parameters are calculated by comparing two distinct scenarios (see section 2.4.1)—baseline (no SAI) and SAI—for 24 selected clear-sky days (as detailed in Table A2). This analysis includes varying the panel tilt from 10° to 40° and considering three positioning modes: East-facing, West-facing, and South-facing.

2.4.7 Broadband flux estimation over SIRTA station using GRASP RT model

GRASP model's geometry and settings:

At this stage, the current implementation of the GRAST RT model includes the capability to calculate both DirHI and DHI on various tilted surfaces. The orientation of these tilted surfaces is defined by the relative azimuth angle (RAA) and viewing zenith angle (VZA). This specific adaptation of the GRASP model incorporates the geometrical representation and orientation of the PV panels, as illustrated in Fig. 2.4.5, into its simulation settings.

- Viewing Zenith Angle (VZA) corresponds to the **tilting** of the PV panel.
- Relative Azimuth Angle (RAA), measured from North, signifies the **orientation** or facing direction of the PV panels. For example, panels facing South have an RAA of 180˚, and panels facing East have an RAA of 90˚.
- Surface Layer Height = Measurement height = 156 m (above mean sea level) for SIRTA station, Paris (Lat: 48.713 ˚N, Long: 2.208˚ E)
- Lambertian Surface: two types, one with albedo 0.05 and another with 0.20 (spectrally flat)
- Solar Zenith Angle (SZA): 10˚ <= SZA <= 80˚
- Solar Spectrum range; 0.4 – 4.0 µm

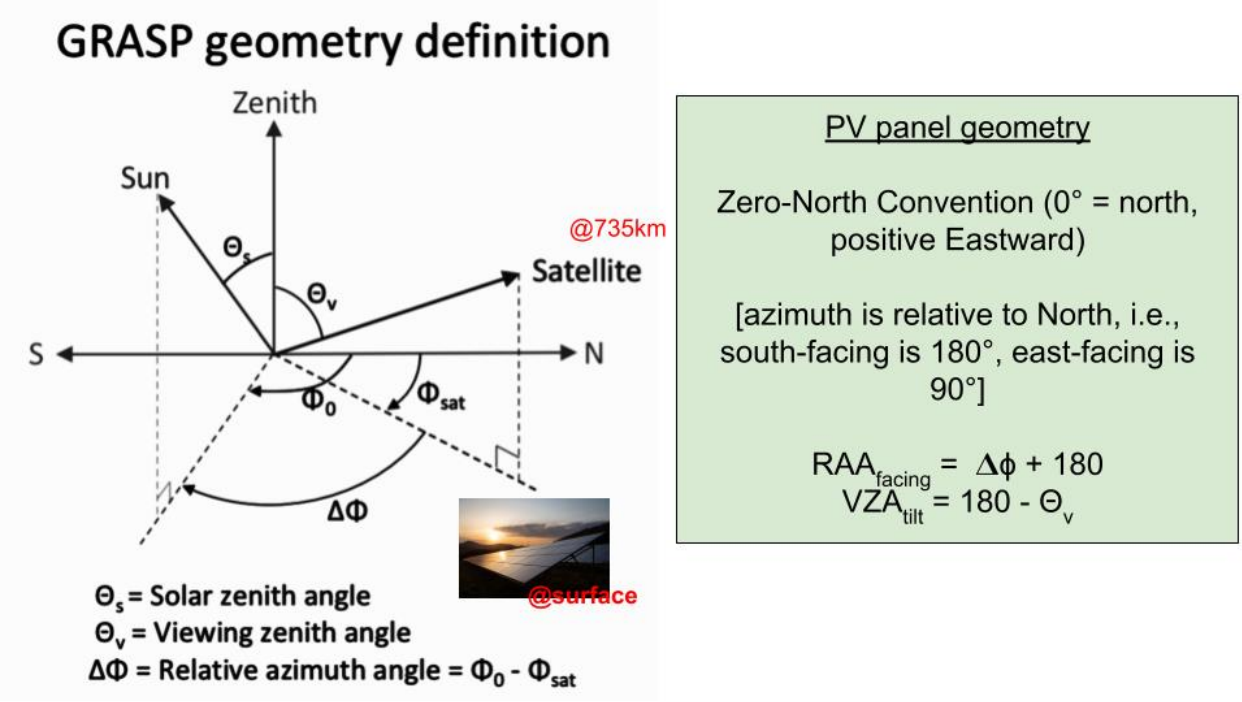

Figure: 2.4.5: The RT simulation geometry as adapted within the GRASP model. The satellite's position in the standard geometry is modified to represent the PV panels.

Stratospheric Aerosol Injection (SAI)

Following the work package's protocol, the aerosol type selected for SAI is sulfuric acid (H_2SO_4). Its physical and chemical properties are based on the description by Hummel et al. (1988). Although its real and complex refractive indices are derived from 75% sulfuric acid droplets (25% water) at 215° K, the particles are not permitted to undergo hygroscopic growth, regardless of the injection altitude. For the SAI simulations, approximately 10^{11} particles are injected per square meter. The SAI injection is modeled using a Gaussian profile (see section 2.4.5). Specifically, libRadtran's model centered this profile at 19 km above mean sea level (ASL) with a standard deviation of 1.5 km. In contrast, GRASP models the profile with a peak at 15 km ASL and a standard deviation of 2 km. Despite these differences, the resulting aerosol concentration and optical properties are consistent and produce an AOD_{SAI} at 550 nm of 0.07.

The parameters for the number size distribution are a mode radius of 0.12 μm and a geometrical standard deviation of 1.60 (unitless). Using the Hatch-Choate equation, the effective radius of the SAI particles was calculated to be 0.2085 μm. The effective radius is defined as the ratio of the distribution's third moment (volume) to its second moment (area). The moment-based equation is given by:

$$r_{eff} = \frac{\int r^3\, n(r)\, dr}{\int r^2\, n(r)\, dr} \qquad \text{(Eq. 2.4.5)}$$

2.4.8 LibRadtran model simulations over SIRTA station and Validation

The libRadtran model was validated by comparing it with the ground-based measurements at the SIRTA site. In Figure 2.4.6, the global (GHI), direct (DirHI) and diffuse (DHI) horizontal irradiance is plotted as a function of time on June 7th 2024. We have employed two different tropospheric background reanalysis inputs to test the robustness of the model and validate the reanalysis data. The dotted line represents the model run with AERONET data (specifically AOD550, ångström coefficients and total water content), whereas the solid line stands for a model run using CAMS input. The SIRTA ground-based measurement data is shown by the dashed lines.

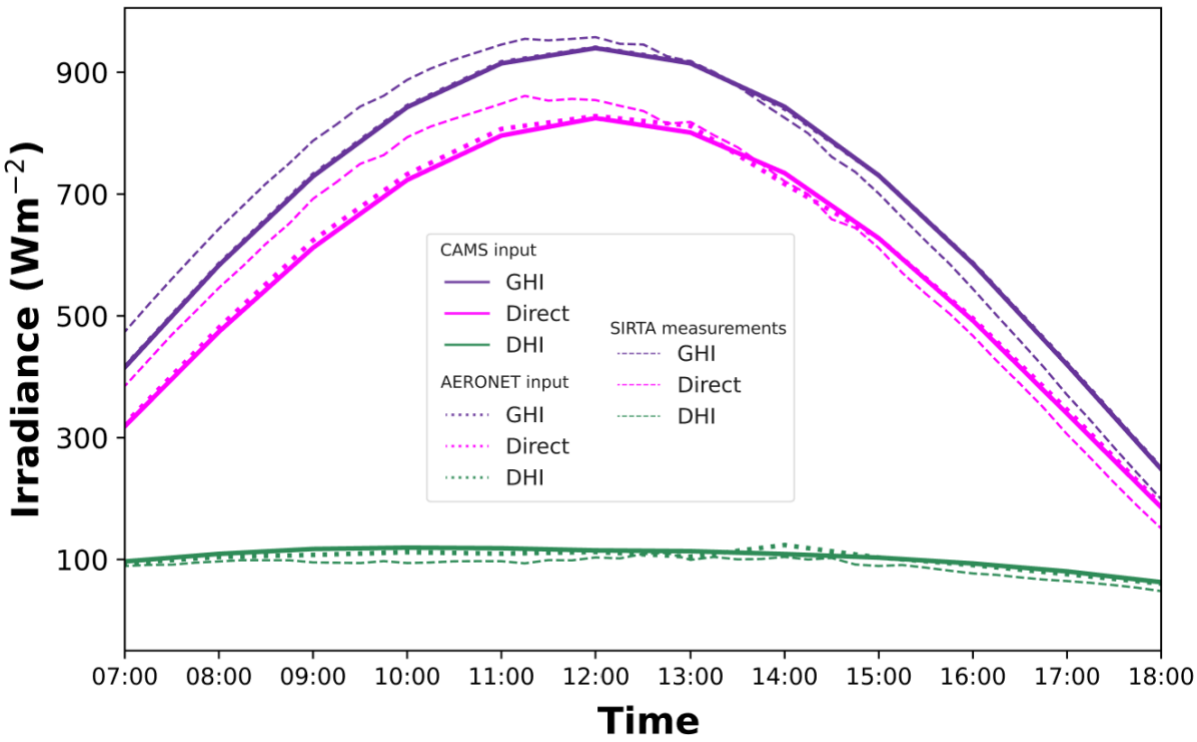

Figure 2.4.6. Global (GHI in violet), direct (DirHI in magenta) and diffuse (DHI in green) horizontal irradiance for June 7th 2024 at SIRTA station. Two different tropospheric background input parameters were applied for the libRadtran model runs (CAMS with solid lines and AERONET with dotted lines). The ground-based pyranometer measurements are depicted with shaded lines.

The data agrees very well for the diffuse component of the irradiance (DHI in green) for both reanalysis model runs and the ground-based measurements at the SIRTA site. It only slightly differs throughout the day and equals approximately 100 Wm^{-2}. In addition, both reanalysis runs show the same output for the direct component (magenta) and hence, the global (GHI in violet). Some discrepancies can be found in the morning (07 - 12h) when the libRadtran simulation underestimates the DirHI compared to the measurement by about 60 Wm^{-2} and in the evening (15 - 18h) when the model simulates slightly overestimates it by 10 to 20 Wm^{-2}. As GHI is comprised of both DirHI and DHI (see Eqn. 2.4.4), the same pattern can be observed there. This can also be seen when simulating the other 23 days, but the difference gets smaller towards higher SZA values (Northern hemispheric winter). The data are not shown here for readability.

2.4.9 Influence of SAI on horizontal irradiances within libRadtran

In this section, we discuss the change in irradiance if applying the SAI scenario of sulfuric acid with an AOD550 equal 0.07 as outlined above. Figure 2.4.7 shows again the diurnal cycle of irradiances on June 7th, but now with and without modeling the SAI layer. The triangles depict the simulations without SAI and hence the same data as in Figure 2.4.6,

whereas the irradiance values modelled including the SAI layer are shown with filled circles.

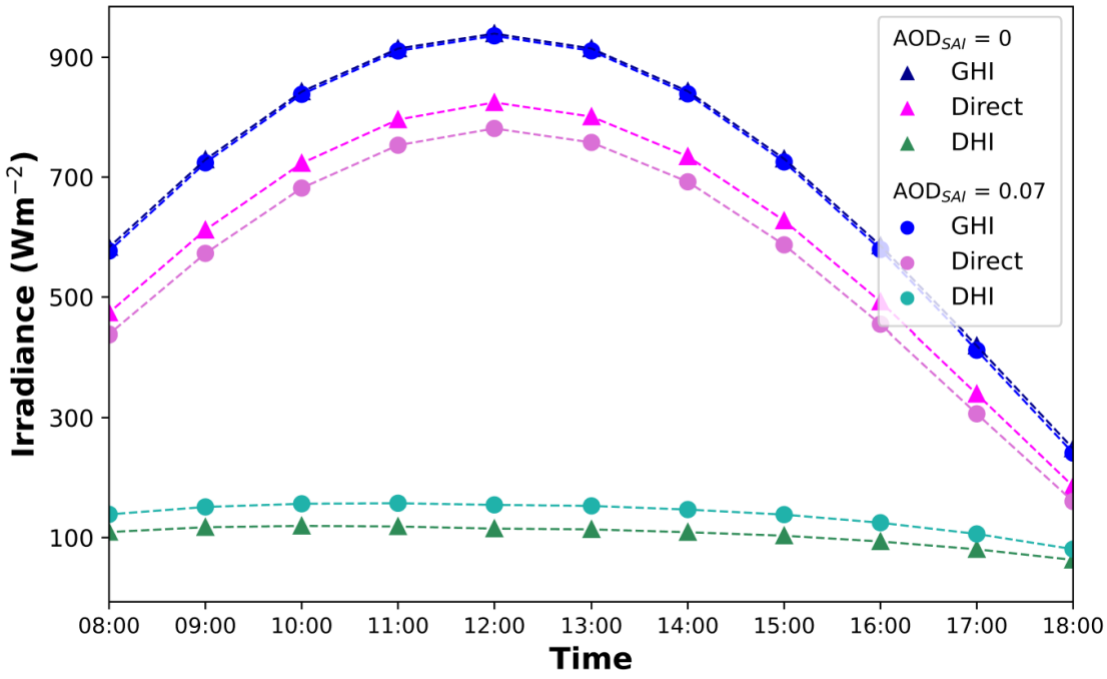

Figure 2.4.7. Global (GHI), direct (DirHI) and diffuse (DHI) horizontal irradiance (color-coded) modelled for June 7th 2024 with an AOD$_{SAI}$ = 0.07 (circles) and without the SAI scenario (triangles).

In summary, the difference in GHI between a SAI scenario (AOD$_{SAI}$ = 0.07) and its reference is very small and accounts for 5 to 8 Wm^{-2} on average. As expected, one can observe a bigger change in the direct and diffuse component. The DirHI becomes lower with a sulfuric acid layer in the stratosphere due to attenuation effects. However, interestingly, this decrease is almost balanced out by an increase in the DHI compared to the reference case. We elaborate more on the resulting differences in the next section while taking into account tilted surfaces.

2.4.10 Influence of SAI on Tilted Irradiance within libRadtran

The potential of PV panels also highly depends on their orientation towards the Sun and their tilting. To evaluate this, we have simulated various tilt angles as outlined above as a function of diurnal cycles (SZAs). In Figure 2.4.10, we highlight three different cases including a clear-sky day in January, April and June (same color code as in previous Figures). We calculated the percentage differences for all three irradiance components between the SAI and reference scenarios. The azimuthal orientation of the panels is South for all the data shown here.

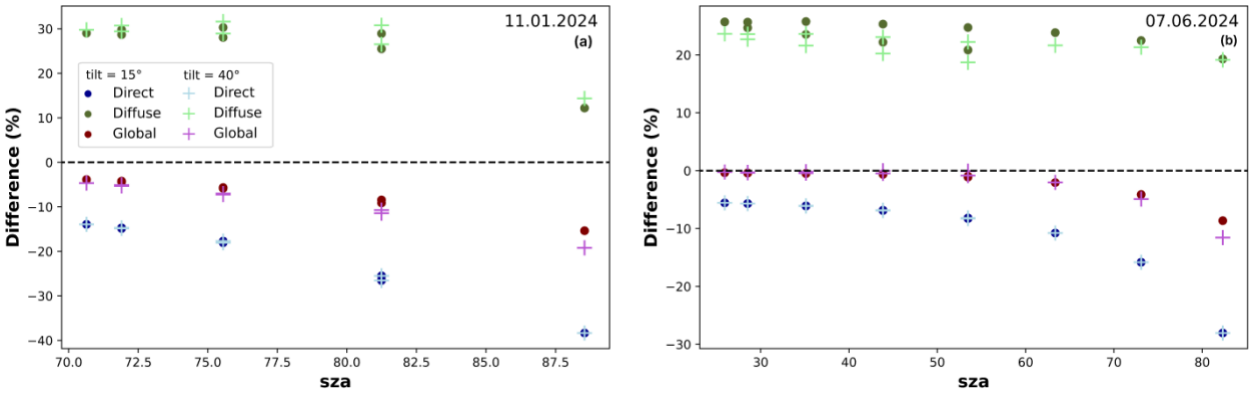

Figure 2.4.8. The percentage differences between the SAI and reference scenarios of global (GHI), direct (DirHI) and diffuse (DHI) irradiances (color-coded) modelled for January 11th (a) and June 7th (b) 2024 intercepted by a tilted surface for two tilt angles (15°, circles and 40°, pluses) with an orientation to the South.

As already discussed above, the global component differs only marginally (-0.1 to -1%) for both tilt angles (15° and 40°) at sza < 60°. However, the difference gets bigger (up to -20%) towards higher SZA, which can be observed for all days in the evenings and for January 11th (a) throughout the whole day. The tilt angles seem not to have a big impact on the percentage differences as the difference of the direct component stays constant. The difference in the diffuse component, however, is lower in the simulation for a 40° tilt on June 7th (b), but higher when modeling the January day (a). So, in general, the global irradiance is not decreasing substantially if applying SAI with an AOD550 of 0.07. It will be very valuable to see the influence of the PV panel technologies and hence, energy output when applying the PV energy model on the tilted irradiance data.

2.4.11 Inter-comparison of Irradiances (GRASP vs. libRadtran vs. Observations)

To ensure the robustness of the irradiance dataset used for the subsequent PV energy modeling, we compare the **GRASP** and **libRadtran** model results for DirHI, GHI, and DHI between themselves and with:

1. **SIRTA** measurements: we use ground-based, high-precision pyranometer and pyrheliometer measurements from the SIRTA station near Paris. These observations provide the "ground truth" reference.
2. **SARAH-3** Dataset: we use the Surface Solar Radiation Data Set - Heliosat (SARAH-3), which provides long-term, high-quality, satellite-derived solar radiation products across the globe.

Shared Data

The shared dataset details the findings of the two RT models, in accordance with the aforementioned methodology and atmospheric inputs. The principal objective is the quantification of the three primary broadband flux components—DirHI, GHI, and DHI—at the **SIRTA** station under both baseline (absence of SAI) and SAI scenarios. The results yielded by the GRASP simulation are subsequently subjected to a comparative analysis against independent simulations performed by the libRadtran model. Furthermore, these outcomes are rigorously validated against available ground-based pyranometer measurements sourced from the SIRTA station and the SARAH-3 global satellite-derived dataset.

In this section, we outline the two model outputs for June 7th.

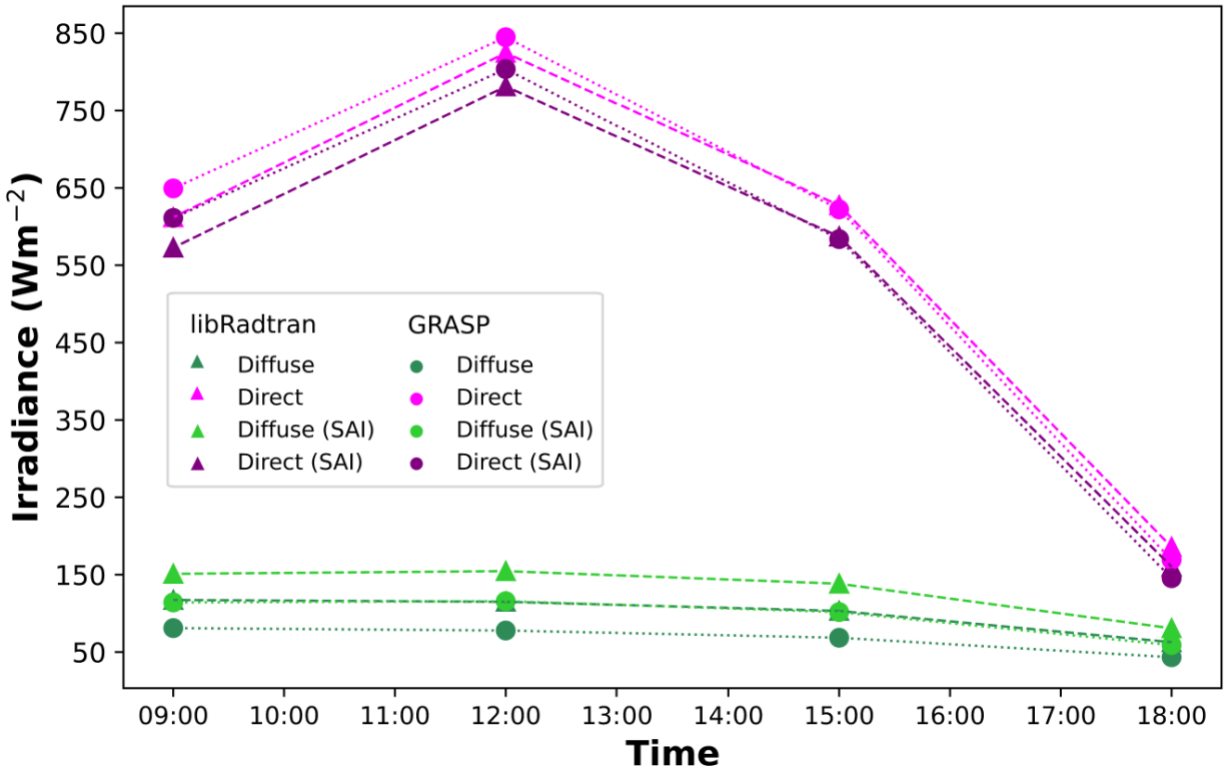

Figure 2.4.10. LibRadtran (triangles) and GRASP (circles) model comparison for June 7th, 2024 showing the diffuse (DHI) and direct (DirHI) horizontal irradiance components for with and without SAI scenarios. The libRadtran results are simulated with a Lambertian surface with an albedo of 0.15, whereas GRASP used an albedo of 0.20.

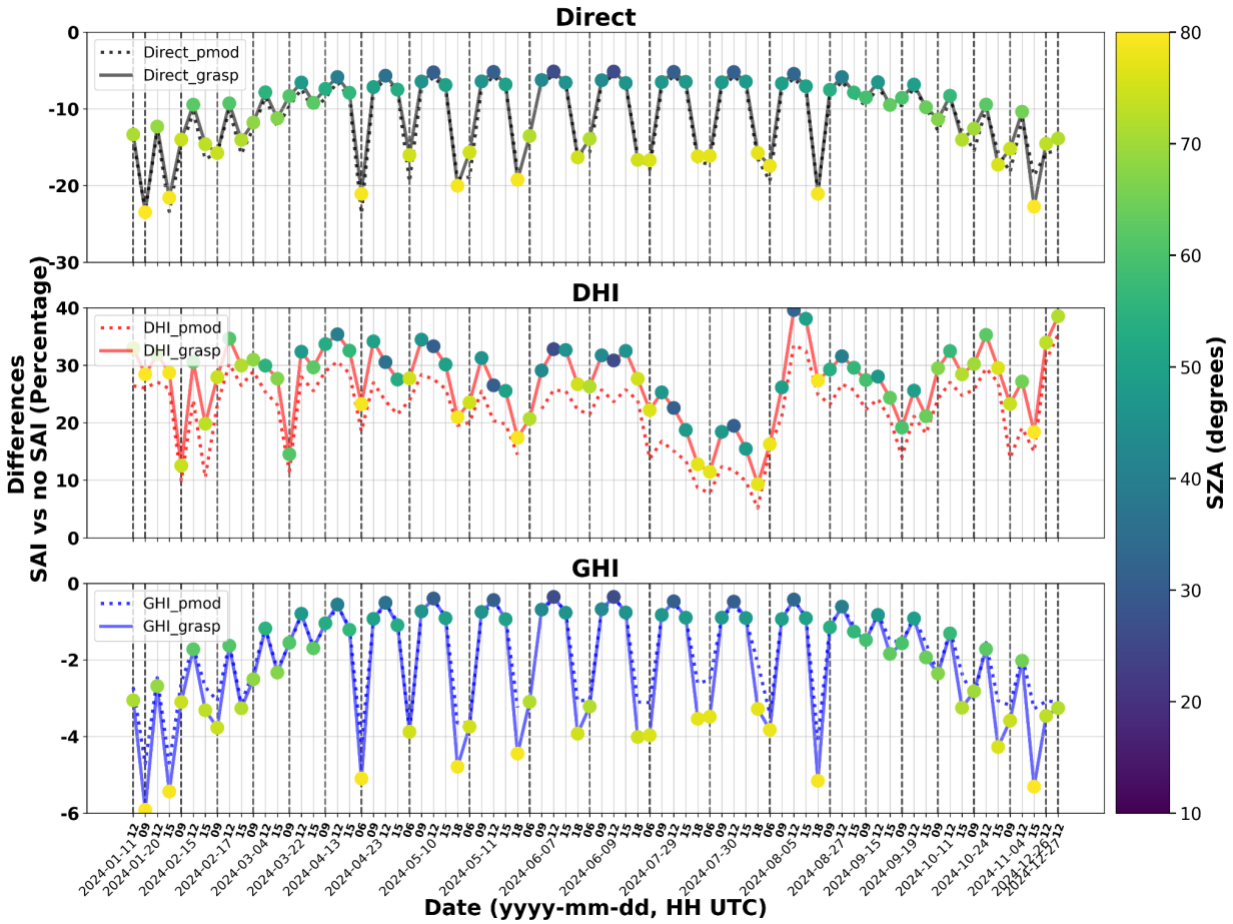

Figure 2.4.11. A comparison between the libRadtran (dots) and GRASP (solid line) simulations for 24 selected days throughout 2024. The plots show the percentage differences between SAI and non-SAI scenarios, calculated relative to the SAI scenarios, for three broadband flux parameters over a horizontal plane: DirHI (1st row), DHI (2nd row), and GHI (3rd row). The scatter plots indicate the SZA values at the SIRTA station.

Figure 2.4.10 illustrates the 3-hourly irradiance data for June 7th, 2024, modeled using libRadtran and GRASP. Generally, the GRASP model projects a **higher direct irradiance** and a **lower diffuse irradiance** compared to libRadtran. A significant difference is observed in the DHI, which is approximately 30-40 Wm^{-2} lower in GRASP at noon, with smaller differences throughout the rest of the day. The peak DirHI modeled by libRadtran is 824 Wm^{-2}, while the GRASP model yields 845 Wm^{-2}. The observed discrepancies, that is a slightly greater DirHI and a lower DHI reaching the surface in the GRASP model. The bigger deviation in the DHI component is intuitive as the absolute irradiances for the DHI component are generally much lower compared to the DirHI component. The optical properties and aerosol particle concentration, hence the AOD, for the SAI layer is identical in both models. Hence, we argue that the disparity is mainly due to the not totally identical total column aerosol optical properties derived from CAMS

reanalysis for the tropospheric aerosol and gas phase composition. Specifically, in libRadtran the input for the asymmetry coefficient and single scattering albedo was taken from AEROCOM climatology and hence, a monthly average is used in comparison to CAMS reanalysis. Also, the columnar ozone concentration was set to constant at a value of 300 DU. In the GRASP model, all 11 types of aerosols' size distribution, vertical distribution of mass mixing ratio, and hygroscopic growth are taken from CAMS reanalysis (see section 2.4.3), without any ingestion of AEROCOM datasets. Moreover, the two RT models differ in their treatment of spectral range and resolution. GRASP RT simulations estimate broadband flux parameters across a wider range, from 200 nm to 4.0 µm, using 209 spectral bins (though in this case study, the range is limited to 400 nm to 4.0 µm). In contrast, libRadtran simulation covers a range of spectrum, from 300 nm to 2.5 µm, but uses a much higher spectral resolution of **1 nm**. Better spectral resolution more accurately captures the real and complex refractive indices of each aerosol type across this spectrum range. Therefore, further investigation through sensitivity analysis is necessary (see section 2.4.13) to clearly understand the differences in broadband flux values at the surface. So, in summary, we like to emphasize that the focus of this work lies on the qualitative difference between SAI and non SAI scenarios on the surface irradiance (shown in Fig. 2.4.11) and as mentioned, a detailed model validation would surpass the scope of this work package.

2.4.12 Outlook with libRadtran

Early in the project phase, the idea of testing other SAI material investigated in literature on the impact of surface irradiance emerged at PMOD/WRC in collaboration with Timofei Sukhodolov. Hence, we have calculated mie scattering properties for diamond, calcite and alumina particles within libRadtran. The size distributions, refractive indices and number concentrations were taken from Vattioni et al. (2024). Preliminary results are shown for June 7th, 2024 at the SIRTA site in Figure 2.4.12. The reference scenario (SO_2) depicts the SAI scenario of sulfuric acid discussed above. In short, the data reveals the largest change of irradiance between the solid particles and sulfuric acid, whereas the difference of irradiance among the solid particles is less. In the next step, we will study these other scenarios in more detail as we aim to build a model including Mie calculations as a function of atmospheric layers compared to only using one at 19 km. This approach can then also be used for the sulfuric acid case proposed in the STATISTICS project.

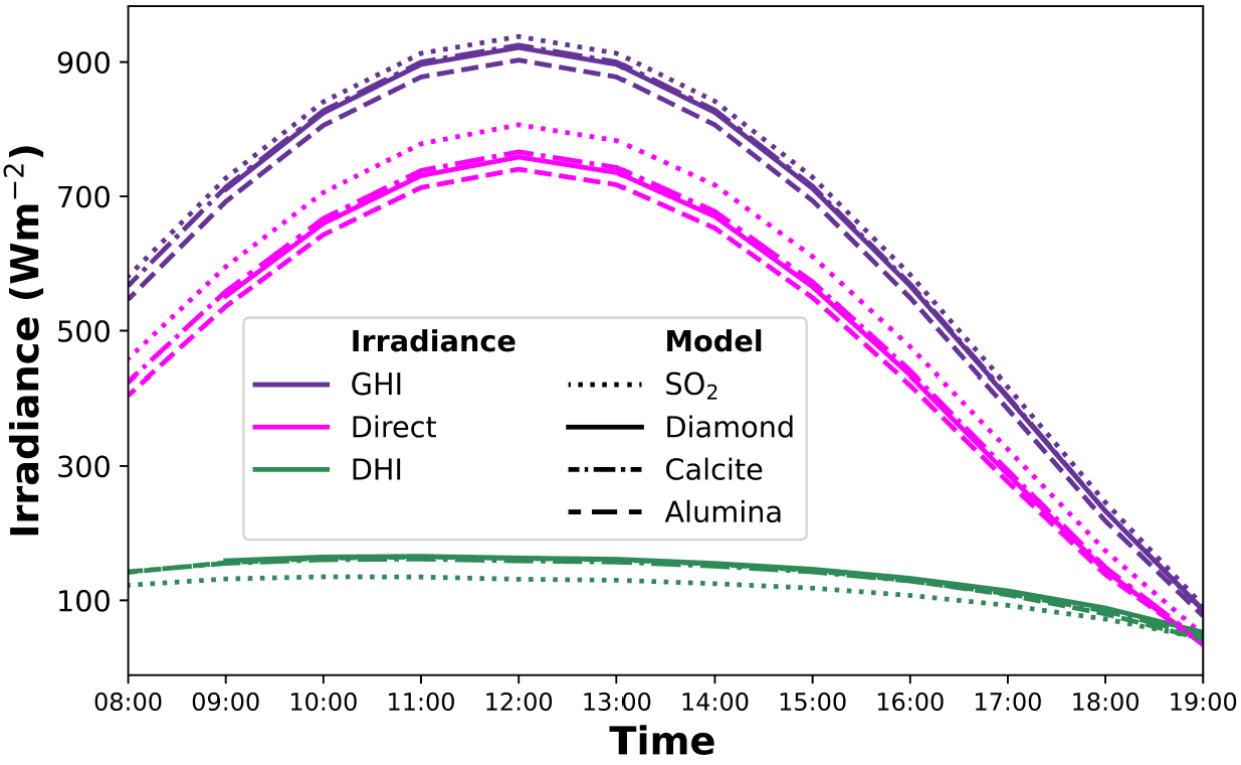

Figure 2.4.12. LibRadtran model results of global (GHI in violet), direct (DirHI in magenta) and diffuse (DHI in green) horizontal irradiances for June 7th, 2024 for the SIRTA station. Different SAI scenarios (sulfate, diamond, calcite and alumina particles) are shown with different lines.

Having more detailed layering, it will also be possible within libRadtran to derive the heating rates in each atmospheric layer induced by injecting aerosol particles into the stratosphere. This could help to understand the trade-off between lowering Earth's temperature by applying SAI and its effect on PV energy production. In addition, with libRadtran we can also calculate and analyze SAI direct radiative impacts on global air quality by quantifying the photolysis rates of O_3 and NO_2.

2.4.13 Outlook with GRASP

We aim to further investigate the notable discrepancies, primarily concerning DHI, observed between the SARAH-3 satellite product, in-situ measurements from the SIRTA station, and simulations performed using the GRASP RT model. Initial simulations, conducted by ingesting the **CAMS aerosol mass mixing ratio vertical profiles** into the GRASP RT model, consistently demonstrated an underestimation of DHI values compared to the available ground truth data (SIRTA measurements). This underestimation persists despite the ingestion of the exact CAMS aerosol size distribution (Bozzo et al., 2020), hygroscopic growth, and the use of accurate real and complex refractive indices for the 11 aerosol types, informed by insights derived from AERONET

and GRASP aerosol property retrievals. Detailed analysis reveals that AOD at 550 nm (AOD550) provided by CAMS is higher than the corresponding value estimated by the GRASP RT model (RT_1), as noted in Fig. 2.4.13, based on a case study from 2024-06-07. Consequently, a sensitivity test is carried out where the CAMS aerosol mass mixing ratio is adjusted for all 11 species by using a scaling factor (i.e., ratio of CAMS AOD550/GRASP AOD550) and subsequently ingested into the GRASP RT model (RT_2), with the explicit objective of matching the AOD550 reported by CAMS (Fig. 2.4.13). This adjustment yields improvements in the simulated DHI values when compared against the available measurements. Given that this case study involves very low AOD550 values (~ 0.1), we propose, in future work, to extend these investigations across the entirety of 2024. This comprehensive analysis will also facilitate a more accurate characterization of aerosol microphysical properties of all chemical components through the usage of broadband flux values measured at the SIRTA station. A critical finding from this exercise is the necessity, in future work protocols, to **exercise caution** when using the CAMS aerosol mass mixing ratio vertical profiles. The incorporation of CAMS AOD550 is instead considered preferable at present, particularly given that the CAMS forecasts are corrected through the assimilation of satellite-derived AOD values at 550 nm, thereby precluding direct corrections to the mass mixing ratios.

Future work will use the complete 24-day clear-sky dataset from 2024 to systematically broaden this investigation across all seasons. By consistently constraining the GRASP RT simulations using the AOD550 derived from CAMS (in contrast to the CAMS mass mixing ratio profiles), the objective is to establish a more robust, empirically-tuned baseline for the DHI, GHI, and DirHI fields. This thorough validation process is essential for two principal reasons: first, it will enable the isolation and quantification of systematic differences among the two RT models driven by CAMS reanalysis, satellite products (SARAH-3), and in-situ ground measurements (SIRTA) across a diverse range of atmospheric conditions. Second, achieving reasonable alignment with SIRTA measurements will not only augment the credibility of the GRASP-derived baseline scenario (in the absence of SAI) but will also subsequently enhance the precision of the SAI impact quantification in the final PV yield simulations, given the pronounced sensitivity of PV systems to DHI and DirHI. This methodological approach effectively uses the measured broadband fluxes as an additional constraint on the total aerosol optical load, thereby indirectly refining the overall quality of the CAMS background aerosol input.

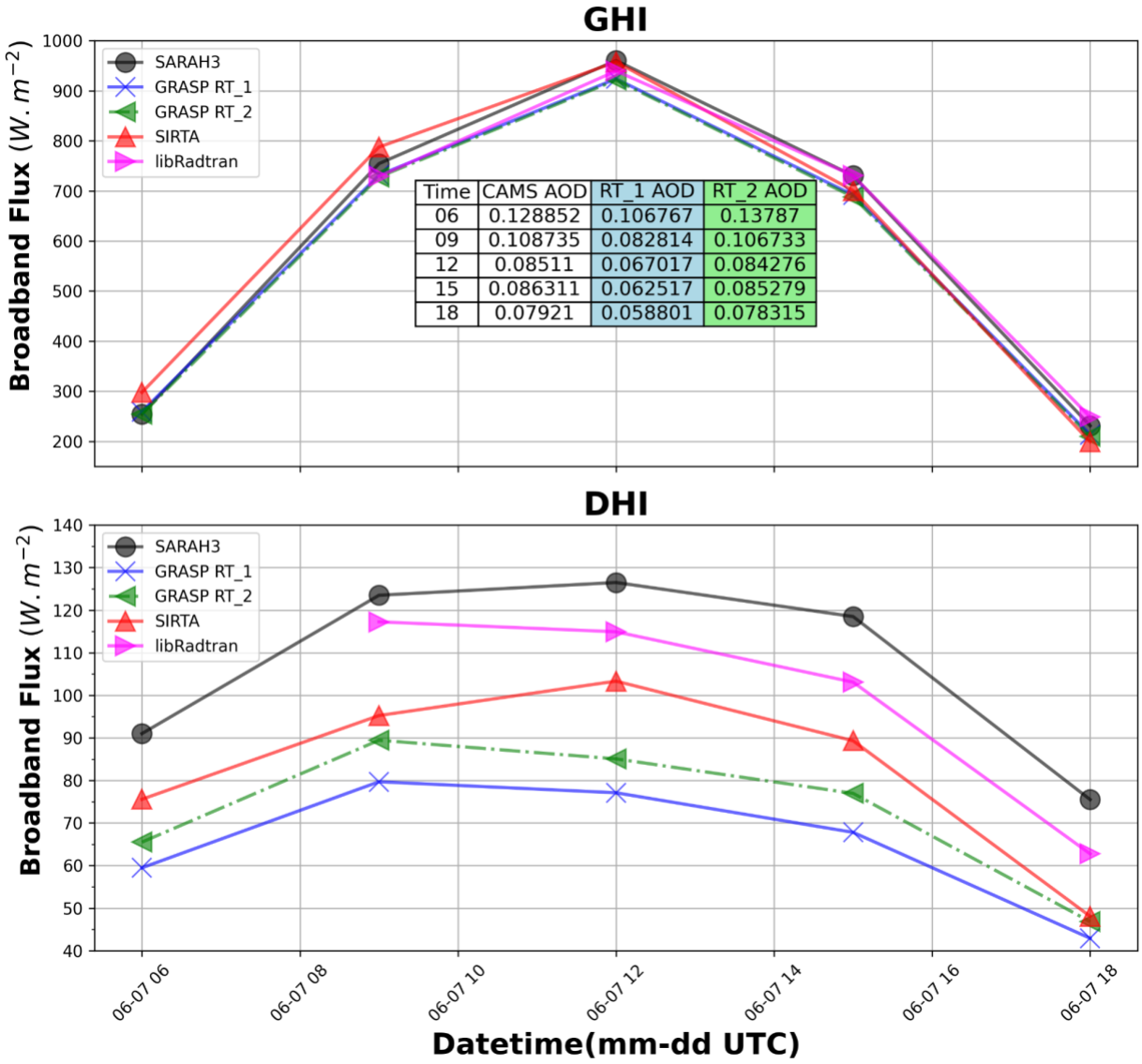

Figure 2.4.13. An inter-comparison of GHI (top panel) and DHI (bottom panel) from four sources on June 7, 2024: the SARAH-3 dataset, SIRTA ground-based instruments, libRadtran, and GRASP RT simulations (RT_1 and RT_2). LibRadtran and GRASP simulations both exclude SAI and assume a Lambertian surface, however with different albedos: 0.15 for libRadtran and 0.20 for GRASP. GRASP **RT_1:** the scenario where CAMS aerosol mass mixing ratios are used directly. **RT_2:** the scenario where the GRASP RT simulation is adjusted using a scaling factor to match the CAMS AOD@550nm (tabulated) by modifying the aerosol mass concentrations.

2.4.14 Detailed impact assessment of SAI on PV yield and energy modeling

The core objective of this WP is to bridge the gap between atmospheric science data and practical solar energy engineering. In the previous sections we have computed a high-temporal-resolution dataset for GHI, DirHI, and DHI values as a basis for rigorous PV performance analysis. This dataset is generated for two distinct scenarios: the 'Baseline' scenario, representing natural atmospheric conditions without SAI, and the 'with SAI' scenario, which incorporates the calculated radiative transfer effects of the proposed SAI intervention.

As these exact computations are expensive, and as a first step, we have fitted the relative change in DirHI and GHI as a function of solar zenith angle using SZA, cosine of SZA and sine of SZA as predictors (Figure 2.4.14). We see that the fit works very well for the DirHI but less well for the GHI because the SZA dependence of this quantity depends more on the background aerosols than for the DirHI. We then use a “pseudo-warming” approach (or in this case a “pseudo-radiation change” approach) by applying this change on actual observational data. This approach has the advantage of relying on observed rather than modelled data for the baseline. Specifically, we use the SARAH-3 satellite products of surface fluxes (Pfeifroth et al., 2024). As a downside, we have to assume that other aspects of the climate, such as cloudiness, do not change with SAI. This approach should thus be understood to represent the impact of SAI on DirHI and DHI, everything else being equal.

The analysis is conducted for the SIRTA atmospheric observatory located in the Paris region (48°N), introduced previously. The baseline simulation corresponds to the year 2024 and relies on hourly surface radiation data from the SARAH-3 (Pfeifroth et al., 2024) data including GHI and DirHI irradiances. DHI is then obtained by difference. This configuration defines the present-day reference against which perturbations are evaluated. An idealized SAI perturbation is constructed diagnostically from the 2024 reference year. As stated above, the objective is to isolate the radiative impact while avoiding dynamical feedback. We simulate the change in GHI and DirHI using a fit to the libRadtan calculations performed by PMOD/WRC. Again, the DHI is obtained by difference (see Eqn. 2.4.4) and all irradiances remain positive by construction. This setup represents a simplified radiative perturbation framework, designed to emulate the enhanced diffuse fraction expected under increased stratospheric aerosol loading, without introducing changes in atmospheric dynamics or cloudiness.

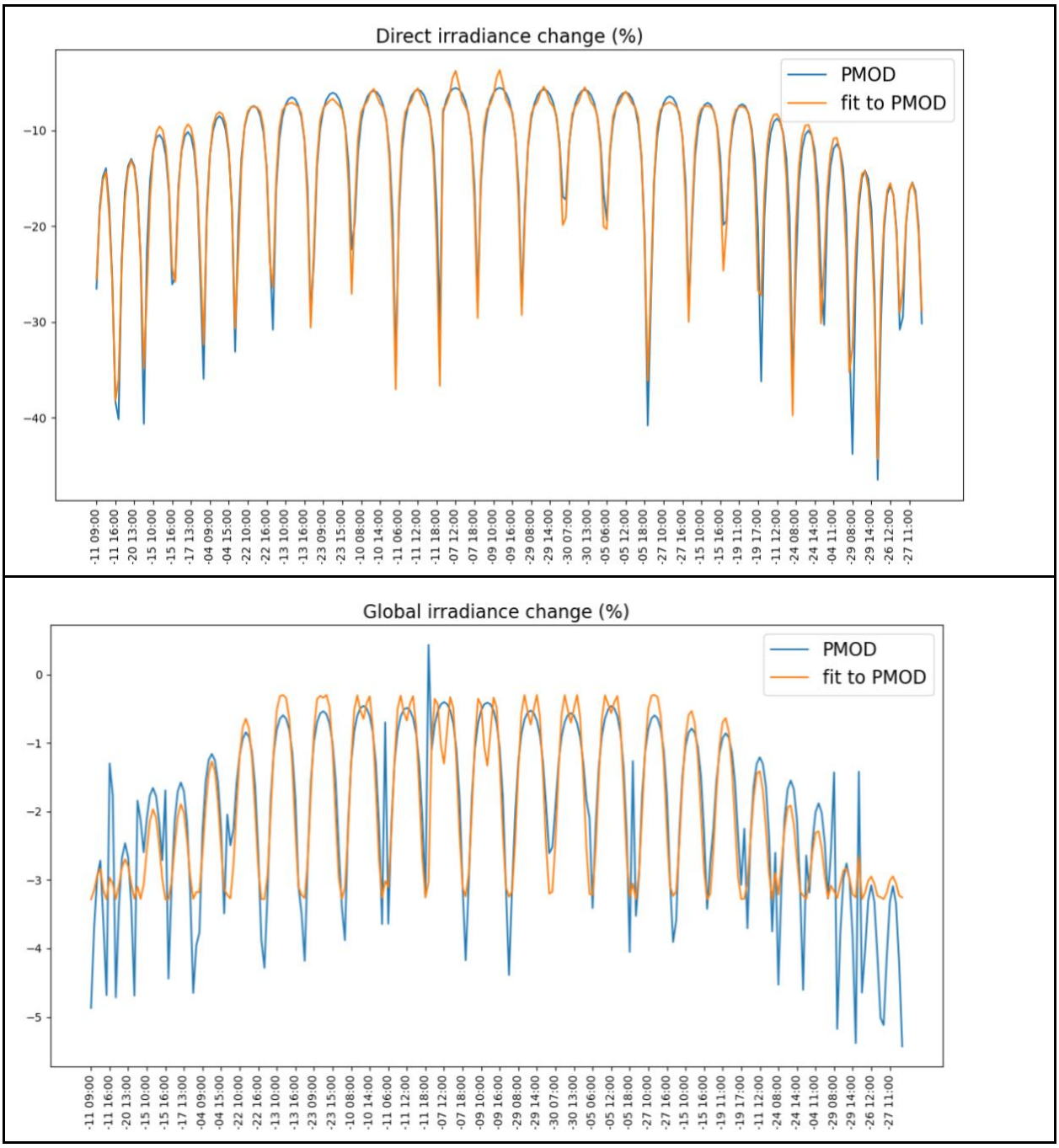

Figure 2.4.14. Fit to the libRadtran (PMOD) data presented in Fig. 2.4.11 for the direct (DirHI) and global (GHI) horizontal irradiance (% change for the SAI scenario relative to the reference scenario).

We then use a PV performance model, explicitly accounting for shading effects across PV panel rows, enabling a realistic estimation of power output under site-specific geometrical constraints. Three representative PV system layouts are examined, differing in geometry and tracking strategy: south-facing fixed-tilt arrays (characterized by their ground cover ratio and tilt angle), east-west oriented arrays with low, symmetric tilts

(characterized by their ground cover ratio and tilt angle), and horizontal-axis (single-tracker) arrays that follow the Sun but with backtracking technology to avoid inter-row shading in the morning and evening (characterized by their ground cover ratio). The ground cover ratio (GCR) is the ratio of panel width to row-to-row pitch.

The first layout is simple but can experience inter-row shading depending on spacing and tilt. The second layout reduces midday peak production and enhances morning and afternoon generation. The third layout maximises production.

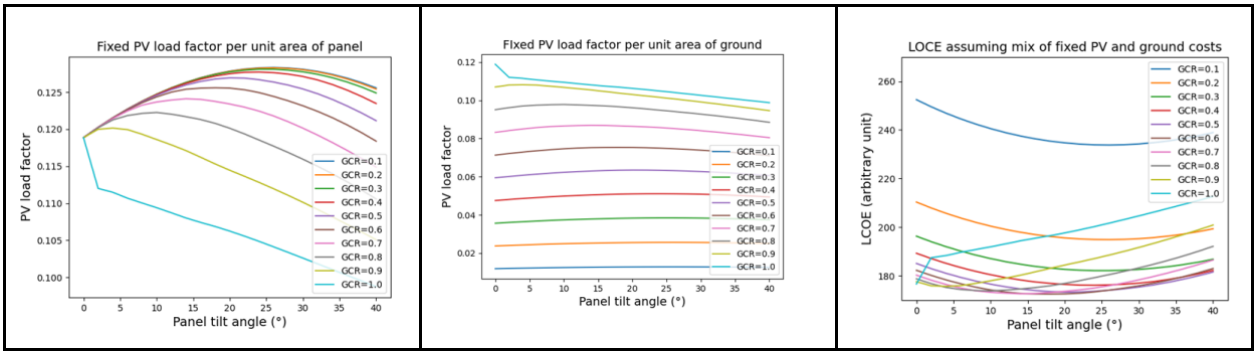

Figure 2.4.15. PV load factors per unit area of panel (left), per unit area of surface (middle) and levelized cost of energy (LCOE) in arbitrary units assuming a mix of PV and ground surface costs for south-facing fixed-tilt panels.

Figure 2.4.15 shows how the PV load factors and an arbitrary levelized cost of energy varies as a function of GCR and tilt angle for south-facing fixed-tilt panels. The economic optimum GCR and tilt are found to be 0.6-0.7 and 20°, typical of mid-latitudes PV fields. Similar computations are performed for the other two layouts (not shown).

Layout	Ref. sce.	Optimum	SAI sce.	Optimum	Diff.
Fixed panels	172.54	b=18° GCR=0.59	175.80	b=18° GCR=0.60	1.89%
E-W panels	92.56	b=1° GCR=1	93.73	b=1° GCR=1	1.26%
Hor-Axis panels	87.39	GCR=0.59	89.77	GCR=0.62	2.72%

Table 2.4.3. Optimal LCOE for the three layouts for the reference and the SAI scenarios. LCOE are in arbitrary units, the three different rows should not be compared.

Table 2.4.3 shows the optimal LCOEs for the two scenarios with GCR and tilt slightly re-optimized for the SAI scenario to account for less DirHI and more DHI. The decrease in LCOE due to SAI is limited to 1.26% for East-West panels (a layout that favors diffuse radiation), 1.89% for south-facing fixed panels and 2.72% for horizontal-axis single-

tracker panels. There is an additional 0.1% loss of performance if the layouts of fixed and single-tracker panels are not re-optimized.

This analysis is a first step to estimate the change in PV panel performance due to changes in the “quality” of solar radiation. It is interesting that the more sophisticated the system, the larger the loss in performance due to SAI. However, the estimated losses are relatively small compared to the performance improvements due to evolution in the technology over the years (e.g. better panels, better tracking technology). Also, it should be noted that we ignore changes in PV panel performance due to reduction in the warming levels expected from SAI.

2.5 Detectability - WP2500/3500

2.5.1 Methods

The SAI natural analogue studies (volcanic eruptions) of WP2100 provide crucial information on the atmospheric state during such possible interventions and possible means of observations of these actions and their impacts. Nevertheless, SAI can occur in such a way that initial detection of SO_2 injections and impacts on the aerosol layer and the stratospheric composition is more difficult than a typical moderate volcanic eruption, due to the progressively increasing intensity of the injections, starting from very small SO2 amounts. Thus, detectability studies are conducted, in this project, to assess the potential for observing SAI signals in the climate system with new observing systems, even in very early stages of the SAI deployment.

This WP addresses, in particular, two future concept instruments:

1) A high-spectral-resolution limb emission (infrared) instrument, based on the CAIRT (Changing-Atmosphere Infra-Red Tomography explorer) instrument concept; CAIRT was a candidate of the European Space Agency’s Earth Explorer 11 call but was not finally selected for funding.
2) A new-generation space-LiDAR system called LUCE from the Agenzia Spatialle Italiana (ASI) and NASA, originally conceived in the development of the AOS Atmosphere Observing System from an international consortium including NASA and the Centre Nationale des Etudes Spatiales (CNES). The LUCE LiDAR is under design presently, with expected launch in 2035 (Di Girolamo et al., Dec 2025, EarthCARE Workshop in Tokyo).

For the CAIRT instrument, one case study has been selected based on an SAI scenario associated with the GeoMIP (Geoengineering Model Intercomparison Project) project (also called, in the following, the pseudo-reality - PR). In particular, in this study we use the Geo SSP5-34-OS 2.0 scenario. This is based on a baseline obtained with the SSP5-

34-OS experiment (a fossil-energy-intensive economy with a relatively optimistic trend for global societal development, see O'Neill et al. (2016) for more details). On top of the SSP5-34-OS baseline, the Geo SSP5-34-OS 2.0 scenario adds SAI as stratospheric sulphur injections optimised, in terms of spatiotemporal and vertical injection rates and progression, to limit the global temperature increase to 2.0°C above 1850–1900 conditions (more details in Tilmes et al. (2020)). The optimised SO2 injections are realised, with different intensities, at 15 and 30°N and 15 and 30°S latitudes. These scenarios are generated with the WACCM (Whole Atmosphere Community Climate Model) model coupled with a three-mode aerosol module. The first study realised in this context aims at testing the capabilities of CAIRT or a CAIRT-like instrument to detect the extremely small amounts of the individual SO_2 injections. To test this on an extreme case, we study here the very first individual SO_2 injection in the SSP5-34-OS 2.0 scenario, which occurs in January 2034. Then we study SA (sulphate aerosols) formation in the first year (2034) following this SO_2 injection phase. To test the detectability of the small initial SO2 injections and the formed stratospheric aerosols in this first phase of SAI for the Geo SSP5-34-OS 2.0 scenario, we generate CAIRT PO (pseudo-observations) using a realistic CAIRT simulator, developed during CAIRT Phase A studies. The processing chain of the CAIRT PO (SO_2 and SA), synthetised in the scheme of Fig. 2.5.1, is based on two steps. First, we project the Geo SSP5-34-OS 2.0 PR on the CAIRT retrieval grid, using a spatial interpolator as the CAIRT scene generator. Based on the CAIRT observation geometry developed during the CAIRT Phase 0 Scientific and Requirement Consolidation studies (SciReC), about 15 daily tracks were simulated along track and on a vertical grid, with 5 positions each across track. Second, the spatially resampled data set is fed to the so-called FL2S simulator, i.e. a simplified retrieval scheme for CAIRT developed during CAIRT's Phase A Performance and Requirement Consolidation studies (PerReC) (Höpfner et al., 2025). During this step, the impact of the vertical smoothing and noise and systematic errors on the CAIRT synthetic observation were simulated. This processing chain is applied to SO_2 and stratospheric aerosol PR datasets (each with its own averaging kernels, measurement and systematic errors from Phase A studies).

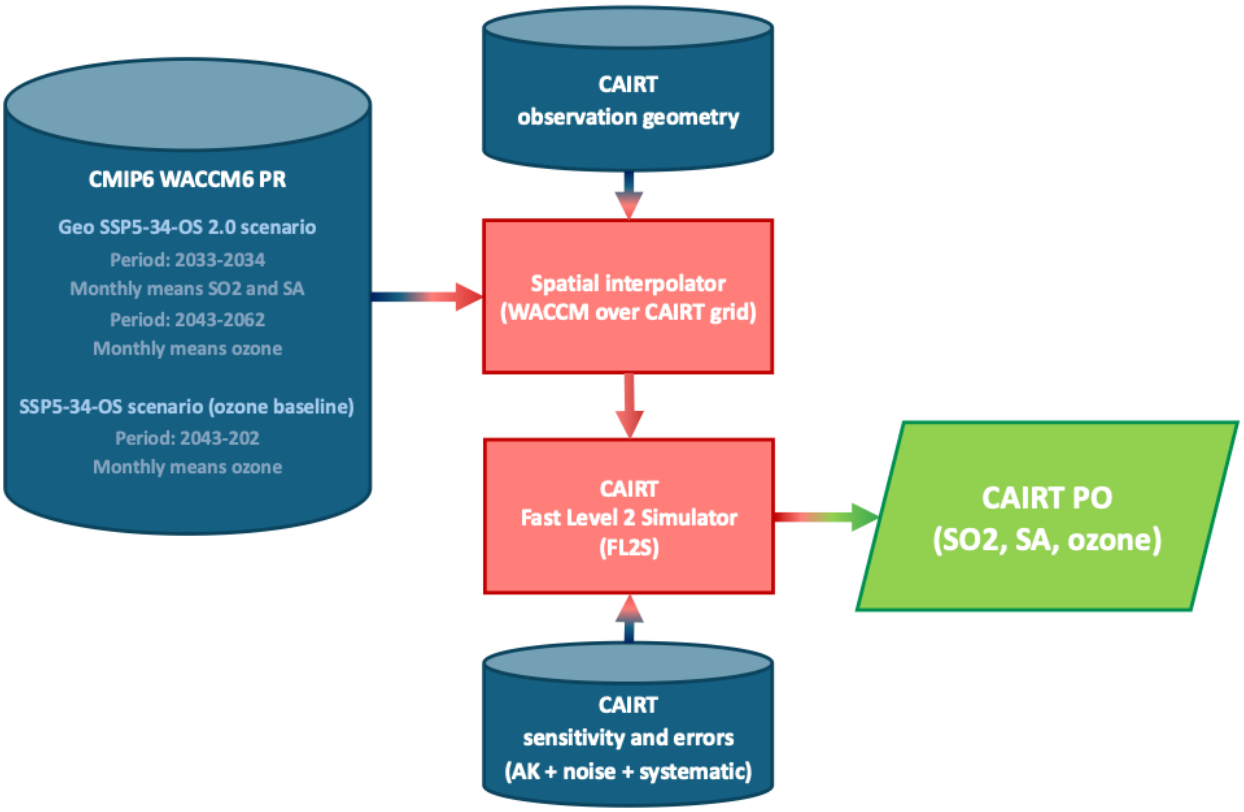

Figure 2.5.1. Schematic of the CAIRT PO simulator used in this impact study.

For the LUCE LiDAR instrument, case studies for volcanic-analogue stratospheric injection PR are realised. This is based on the setup of LUCE conceived within the Observing System Simulation Experiment developed in the framework of the AOS Aerosol French project (Cuesta et al., EGU 2025) funded by CNES. The LUCE space LiDAR observations are simulated with the forward radiative transfer code integrated in the GRASP environment (developed by GRASP-SAS and LOA laboratories). Standard characteristics of sulfate aerosol layers located in the lower stratosphere with several abundances are considered. The pseudo-observation simulator generates lidar signals according to the LUCE's instrumental configuration: three wavelengths (355, 532 and 1064 nm) both for attenuated backscatter and depolarization ratios (tests with only 2 wavelengths for this last channel are performed). We add typical random instrumental noise to these signals, according to an instrumental simulator developed by NASA within the international AOS project (Trepte et al., 2024). Finally, we apply a full inversion scheme based on the innovative type-discriminated aerosol vertical profiling approach named AEROTYPro/GRASP (Qayyum et al., 2025). This allows the quantification of the vertical profile of aerosol concentration for multiple aerosol types simultaneously located in the atmospheric column and therefore the capacity for this instrument to detect and quantify SAIs, as stratospheric aerosols.

2.5.2 Results

For the CAIRT studies, very encouraging results were found for both the initial detection of the SO_2 injections in the selected SAI scenario and the tracking of the formed sulphate aerosol plume. Figure 2.5.2a shows the global map of the average CAIRT SO_2 PO for February 2034, at 25 km altitude. Both the spatial location of the SAG injection, at 15°N and 15°S, and the first dispersion and chemical sink, for this first SAG action in the Geo SSP5-34-OS 2.0 PR scenario, are clearly visible with CAIRT PO. Figure 2.5.2 b-c show the average vertical SO_2 profile PR and CAIRT PO, for February 2034, for the selected CAIRT orbit individuated in Fig. 2.5.2a. The latitude location of the two SO_2 injections for this initial stage in the PR scenario, as well as their altitude (15°N and S, at 25-30 km altitude) can be clearly observed with CAIRT PO. Dynamical features of the SO_2 plume, e.g. the descent in altitude and transport towards higher latitudes for the Northern Hemispheric SO_2 injections, are also detected by CAIRT (time series results not shown here). The total SO_2 mass values intercepted by this specific CAIRT orbits in Fig. 2.5.2 is 0.5 t (injection at 15°S) and 3.4 t (injection at 15°N), respectively. These injections are characteristic of “near-term” to “mid-term” experiments, i.e. scenarios considered feasible even with presently existing technology and relatively low cost. These injections are thus millions of times smaller than moderate-to-large volcanic eruptions (Raikoke eruption, 2019: ~1.5 Mt, Mount Pinatubo eruption, 1991: ~20 Mt). Our study shows that CAIRT would be capable of detecting such deliberate releases, even those as small as a few tonnes. In particular, CAIRT would be able to determine geographical location, altitude, and magnitude (CAIRT POs: 0.4 and 3.1 t, for the two injection points) of the injection, though possibly with a small bias (around 10% and 25% underestimation of the larger and smaller injection, respectively). CAIRT would therefore provide a unique capability to detect and quantitatively assess unilateral and/or illegal SAG interventions within just a few days of the injection. The injected SO_2 is then converted to solar-radiation-reflecting SA particles, with timescales of a few weeks-to-months. In addition to detecting SO_2, CAIRT can track the temporal evolution of the resulting SA layer as it spreads toward higher latitudes through meridional dispersion, as well as monitor changes in its vertical distribution over time (results not shown here).

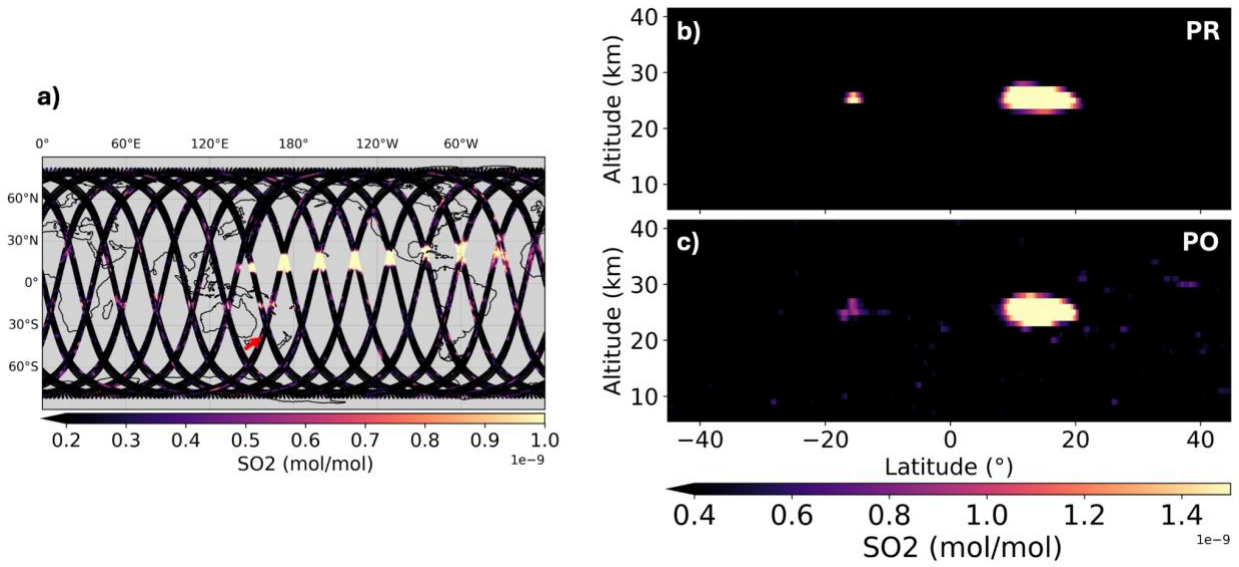

Figure 2.5.2: (a) CAIRT PO of the SO_2 concentration for February 2034, at 25 km altitude. (b-c) Average PR (panel b) and CAIRT PO (panel c) of the SO_2 vertical profiles, for the orbit individuated with a red arrow in panel a.

In the framework of the LUCE LiDAR study case, a new aerosol type representing sulfate aerosols in the lower stratosphere, with characteristics typical of SAI scenarios, is introduced into the GRASP framework. This aerosol is defined by a lognormal size distribution with a modal radius of 0.2 μm and a geometric width of 1.7, and by a complex refractive index taken from Hummel et al. (1988). Using the tailored LUCE full retrieval simulator, the corresponding aerosol optical properties and associated lidar signals are then simulated to assess their detectability and retrieval performance. First simulations indicate that sulfate aerosols exhibit moderately spectrally variable lidar ratios, while showing—as expected—a single scattering albedo close to unity and a measurable spectral dependence of the backscatter coefficient (see Figure 2.5.3). Current activities focus on the quantitative retrieval of aerosol-type concentration profiles using the newly developed AEROTYPro/GRASP approach (Qayyum et al., 2026, in revision, Remote Sensing of Environment). This includes the adaptation of retrieval constraints and first-guess assumptions to ensure robustness for stratospheric sulfate conditions. Next steps will involve a comprehensive sensitivity analysis to key sulfate aerosol properties, in particular variations in particle size distribution and aerosol acidity, in order to quantify their impact on optical properties, lidar observables, and retrieval performance.

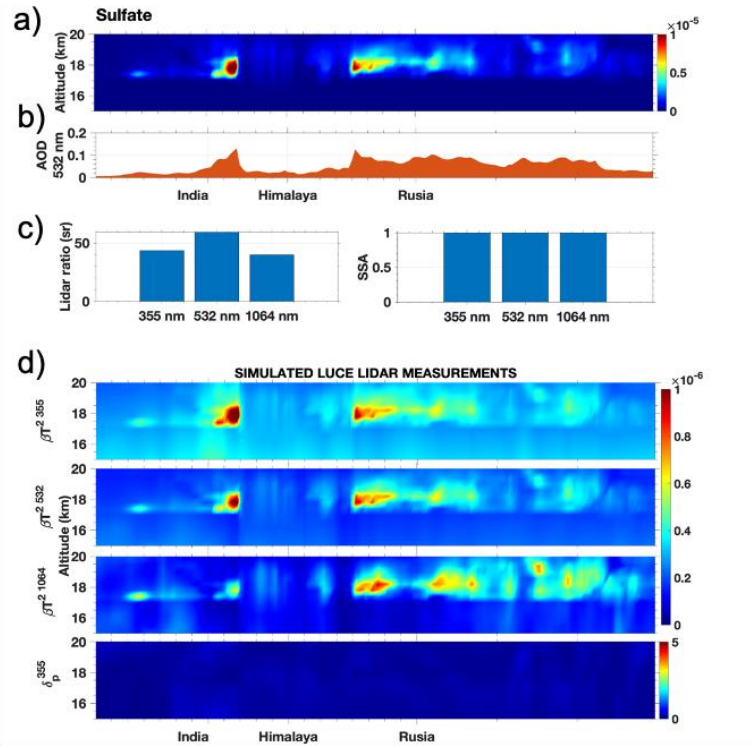

Figure 2.5.3: Example of transect of a simulated sulfate aerosol layer in the lower stratosphere simulated with typical SAI characteristics in terms of (a) vertical profiles of volume mixing ratios and (b) aerosol optical depth at 532 nm and (c) associated lidar ratios and single scattering albedo at the 3 wavelengths. (d) Simulated LUCE lidar measurements of attenuated backscatter (depolarization is shown only for 1 wavelength)

2.5.3 Technical gaps and limitations

Despite the strength of satellite observations, presently there are gaps and limitations to available observational datasets and the current global observing system:

- Lack of stratospheric aerosol profiling instruments: there is currently no continuous, high-resolution global monitoring of stratospheric aerosols, especially in the upper stratosphere, the stratosphere and over the poles.
- Low AOD detection and lack of measurements of absorption properties: the detection of localized low AOD (e.g. as expected from SRM injections) would be difficult due to the variability in aerosol background conditions. This point and the previous one are particularly pressing after the non-selection of CAIRT. In addition, accurate satellite absorption and scattering properties (e.g., single scattering albedo and phase function) is limited, thus limiting further exploitation of satellite observations for the optical and radiative characterisation of stratospheric aerosols.

- Low temporal resolution: there is a lack of high-frequency (hourly or sub-hourly) monitoring from polar satellites, especially over the oceans. Geostationary satellites for air quality, i.e. with a high spectral resolution, are still emerging.
- Low spatial density of ground-based solar networks especially in Africa and parts of Asia.
- Few ground-based radiation sites in remote regions or developing countries.
- Uncertainties in trace gas high resolution detection. Source attribution models are under-developed for putative small-scale or covert SRM activities.
- Insufficient ground-based coverage for satellite validation in key areas. Validation and calibration of satellite data in these regions are poor, increasing uncertainty in global detection.
- Limitations of aerosol satellite retrievals in polar areas and over bright surfaces.

2.5.4 Institutional and other non-technical gaps

Depending on the objectives of detection and monitoring efforts, new institutional arrangements may be required to pool data from various sources as well as to ensure the necessary analytical and interpretative capacity. This could range from informal international collaborations – e.g. data sharing, alignment of observational protocols etc. – to formal cooperations.

Detection capabilities are not limited to Earth system observation, but they may need to include means of open and closed intelligence gathering and the corresponding analytical and interpretative processing of the data. This would require dedicated institutional collaboration arrangements.

2.5.5 Future technical needs for SRM monitoring

Future missions or technologies could include:

- Global high-vertical-resolution limb and solar occultation sensors for continuous stratospheric aerosol tracking.
- Geostationary aerosol and gas sensors beyond Europe, America and Asia (e.g., over the Pacific or Southern Hemisphere).
- Unmanned aerial systems (UAS) and stratospheric balloons for in situ aerosol and gas measurements.
- Expansion of ground-based radiation and aerosol networks, especially in Africa and the Southern hemisphere.
- Improvement of satellite-based AOD and especially other (e.g., absorption, size distribution) properties.

Chapter 3. Impact and Assessment

This chapter synthesises the results of the STATISTICS project and assesses their implications for future scientific research, technical development, and monitoring and detection capacities related to Solar Radiation Modification (SRM). It focuses on the identification of priority research and data gaps, the implications for satellite and non-satellite observing systems, the current and prospective capacity to detect and monitor SRM-related activities, and guidance for future European and international research efforts. The assessment integrates scientific and technical findings with broader considerations relevant for risk assessment, governance, and strategic roadmap development.

3.1 Conclusions from the joint STATISTICS / ACtion4Cooling workshop

An important phase of the project was the joint STATISTICS / Action4Cooling SRM workshop, held in June 2025 at DLR, which brought together a cross-section of the scientific community. The workshop resulted in a set of conclusions and recommendations, which are reproduced below.

Conclusions from the STATISTICS / ACtIon4Cooling workshop on SRM techniques - 17th June 2025

Support for Open-Ended Research
The workshop participants expressed clear support for open-ended research on Solar Radiation Modification (SRM) techniques, particularly through publicly funded mechanisms. Given the deep uncertainties and the high stakes involved with climate mitigation and adaptation, a robust scientific understanding of potential processes, impacts, risks and unintended consequences of SRM must be constrained by neither narrow policy frames nor prematurely operational agendas. Public funding can ensure independence, transparency, and broad stakeholder engagement in setting research priorities. European funding for research explicitly labelled as SRM would build a basis for an independent stance on the topic.

Enhanced Use of Natural Analogues and Existing Observations
Great scientific potential exists in studying natural (and anthropogenic) analogues of SRM, such as explosive volcanic eruptions, low-level degassing volcanoes, changes or variability in traffic (ship) and industry emissions, dust events in the upper troposphere, or contrail cirrus. These opportunities remain underexploited. In particular, satellite datasets – some of which contain relevant but as-yet-unanalysed observations – offer a valuable resource for improving our understanding of aerosol-cloud-radiation

interactions. A coordinated effort to mine and integrate such datasets is recommended. In particular, harmonizing assumptions made in models and satellite retrievals would help to better integrate observations and models (e.g. through digital twins). New observing capabilities should also be mobilized.

Field experiments: Clarity of Rationale and Participatory Design Are Crucial
While small-scale field experiments may eventually become necessary to resolve key scientific uncertainties that cannot be addressed by model experiments, natural analogues or laboratory studies alone, their justification and design must be articulated with great clarity. This includes defining specific scientific and/or technical objectives, ensuring transparent public communication, and co-developing experimental plans with a diverse range of stakeholders to maximise legitimacy, scientific and/or technical value, and ethical integrity. An assessment on potential impacts on weather and climate should be provided as part of the planning. It should be noted that field experiments relevant to SRM techniques may also be motivated by process understanding, regardless of SRM objectives.

Improved Observing System with Distinction Between Monitoring and Detection
The current global observing system is insufficient for monitoring key parameters relevant to SRM techniques, especially for Stratospheric Aerosol Injection (SAI), and for detecting SRM experiments below a certain size or uncoordinated deployment. There remain major observational gaps in trace gases, aerosol and cloud properties, vertical distribution, radiative effects, and troposphere-stratosphere coupling. Further risks are associated with the downscaling, or lack of open access availability to European research, of US current and future observing programmes and satellite missions. A dedicated effort is required to document monitoring priorities in order to enhance these capabilities. The ongoing effort to produce long-term homogenised climate data records relevant to SRM processes should be continued. Observing systems designed to study natural analogues and assess the impacts of planned field experiments may not necessarily be the same as those needed for early detection and attribution of uncoordinated SRM field experiments or deployment.

Improved Modelling Capabilities for Prediction and Attribution
Earth System Models are improving through resolution increase and more comprehensive representation of aerosol and cloud processes, but different models continue to disagree on some key aspects of the climate response to SRM. Moreover, the predictions at subseasonal, seasonal and decadal scales are insufficient to reliably anticipate the impacts of field experiments and potential deployment. Similarly, it is necessary to establish confidence in counterfactual simulations that would be required to quantify intended and unintended impacts of SRM field experiments or deployment.

Research is thus required on how trust in counterfactual simulations may be established. Further model improvements may build on insights from natural analogues and hypothetical future field experiments.

3.2 Implications for research gaps and future research prioritisation

A central outcome of the STATISTICS project is a refined understanding of where the most consequential scientific and technical uncertainties lie across the three SRM techniques considered: Stratospheric Aerosol Injection (SAI), Marine Cloud Brightening (MCB), and Cirrus and Mixed-phase Cloud Thinning (CCT/MCT).

Across all techniques, the findings confirm that **process-level understanding remains the dominant bottleneck**, particularly regarding aerosol-cloud-radiation interactions and their representation across models of different scales. While Earth System Models (ESMs) are indispensable for assessing large-scale and long-term impacts, the project demonstrates that progress in constraining uncertainties depends critically on better integration of observations, targeted modelling, and natural analogue studies.

For **SAI**, uncertainties related to aerosol microphysics, size distribution evolution, stratospheric heating rates, and ozone interactions remain high. The intercomparison of model simulations with satellite observations following moderate volcanic eruptions highlights persistent model spread, indicating that further work is required to reconcile simulated and observed aerosol evolution. Future research should prioritise improving microphysical schemes, better representing troposphere-stratosphere couplings, and exploiting observational constraints from both passive and active satellite instruments.

For **MCB**, the results underscore the scarcity of observational constraints on aerosol properties and cloud responses under realistic perturbations. The analysis of passive volcanic degassing events confirms their value as underexploited natural laboratories, but also reveals limitations related to spatial heterogeneity, background variability, and attribution challenges. Priority research areas include improved characterisation of aerosol size, composition, and hygroscopicity, as well as systematic evaluation of cloud macrophysical responses across different regimes.

For **CCT/MCT**, the findings reinforce that fundamental uncertainties persist regarding cloud susceptibility, ice nucleation pathways, and achievable radiative forcing. The use of satellite-derived cloud phase and microphysical properties demonstrates a viable pathway to constrain model realism, but also highlights the need for sustained efforts to bridge observational scales and model representations. Research prioritisation should focus on establishing robust baselines of cirrus and mixed-phase cloud properties before exploring intervention scenarios.

Overall, the project indicates that **future research prioritisation should favour activities that explicitly link observations, models, and detectability considerations**, rather than treating them as separate domains.

3.3 Data gaps and implications for satellite capability investments

The STATISTICS findings provide a first-order mapping of data gaps that are directly relevant to informing future satellite capability investments, particularly in a European context.

A key conclusion is that **existing satellite systems are sufficient for studying large natural analogues and hypothetical large-scale deployments**, but are generally insufficient for reliably detecting or characterising small-scale experiments or early-stage interventions. Limitations persist in terms of sensitivity to low aerosol optical depths, vertical resolution in the stratosphere, and the ability to measure aerosol compositions and size distribution.

Priority observational gaps include:

- Continuous, high-vertical-resolution profiling of stratospheric aerosols, including over polar regions;
- Improved sensitivity to weak aerosol perturbations against variable background conditions;
- Enhanced capability to retrieve aerosol absorption, size distribution, and composition;
- Sustained, high-quality ice supersaturation and cloud microphysical observations, particularly for ice and mixed-phase clouds;
- Improved temporal resolution, especially over oceans and the Southern Hemisphere.

The results suggest that **incremental improvements to existing missions are unlikely to be sufficient** to address these gaps. Instead, targeted investments in new-generation instruments – such as high-spectral-resolution limb sounders, advanced spaceborne lidars, and next-generation polarimeters – would be required to significantly improve monitoring and detection capabilities.

Importantly, the project highlights that **satellite investments should be guided by clearly articulated monitoring objectives**, distinguishing between scientific research needs, field experiment monitoring, and detection of uncoordinated or clandestine activities.

3.4 Role of international partnerships in complementing European capacities

The assessment confirms that no single region can independently develop a

comprehensive SRM monitoring and detection capability. International partnerships therefore emerge as a critical enabler for both scientific progress and governance-relevant monitoring.

From a European perspective, collaboration can help mitigate gaps arising from uneven geographical coverage, limited access to certain datasets, and uncertainties surrounding the future availability of non-European missions. Partnerships with international space agencies, meteorological organisations, and global observing networks could significantly enhance coverage, redundancy, and resilience.

Beyond technical considerations, international cooperation on monitoring can also contribute to **confidence-building and transparency**, echoing lessons from other domains such as arms control and nuclear non-proliferation. The STATISTICS findings suggest that shared methodologies, interoperable data products, and joint analysis frameworks could be as important as hardware investments themselves.

3.5 Complementary role of non-satellite-based data sources

While satellite observations play a central role in SRM research and monitoring, the project demonstrates that **non-satellite data sources are indispensable complements**.

Ground-based networks, such as sun-photometer arrays, radiation measurement stations, lidars, and trace gas monitoring systems, provide critical validation and high-precision reference measurements that satellites alone cannot deliver. In situ observations from aircraft, balloons, and unmanned aerial systems offer unique insights into aerosol composition and microphysics, particularly in the stratosphere. Commercial aircraft provide useful, yet sparse, measurements of ice supersaturation in the regions of in situ cirrus formation.

Reanalysis and data assimilation systems further act as integrative frameworks, combining heterogeneous observations with models to produce physically consistent datasets. However, the project finds that current assimilation systems are not yet optimised to represent SRM-relevant processes, indicating a need for methodological development if they are to support monitoring objectives effectively.

Strategically expanding and coordinating non-satellite observations, especially in under-sampled regions, would substantially improve both scientific understanding and monitoring robustness.

3.6 Current capacity for detecting clandestine tests or deployments

One of the most policy-relevant findings of the STATISTICS project concerns the **current limits of detectability** for SRM-related activities with a focus on SAI tests.

The analysis indicates that the efficiency and impacts of **small-scale field experiments or early-stage deployments, particularly for SAI, could plausibly remain undetected by the existing global observing system**, especially if conducted gradually or in regions with sparse observational coverage. For MCB and CCT, detectability is further complicated by strong natural variability and the difficulty of attributing observed changes to deliberate interventions rather than background processes. Detection thresholds depend strongly on the type of intervention, spatial and temporal scales, background variability, and the observing system used. Detectability would also depend on the region being considered as both the background variability and observing system vary spatially. Ground-based observing capabilities exhibit strong regional disparities in coverage, instrumentation, and data continuity. Moreover, data sharing cannot be taken as granted, owing to institutional or political constraints. In this context, satellite observations play a critical role by providing globally consistent and independently accessible measurements. AI techniques may further contribute by enabling cross-calibration and transfer learning between heterogeneous observing systems, thereby helping to bridge data gaps and improve inference in regions with sparse in situ measurements.

Our findings also underline that **detectability cannot be treated as binary**, but rather as a continuum that depends on scale, duration, and transparency of activities. This has important implications for both governance and public discourse.

3.7 Capacity for tracking atmospheric effects of large-scale tests or deployments

In contrast, the project finds that **hypothetical large-scale SRM deployments would almost certainly be detectable and trackable** with existing and near-future observing systems. Large perturbations to stratospheric aerosol loading, radiation budgets, or cloud properties would produce signals that exceed current detection thresholds and could be monitored using a combination of satellite and ground-based observations. However, the early detection of deployment-scale tests through current earth observation systems may require them to be directed to specifically observe particular atmospheric areas as they would not currently provide continuing comprehensive scanning of relevant parameters and attributing changes to a test would require using multi-year averages and thus inherently come with a delay. The earliest sources of detection are likely to come from **other means of information gathering** including open or closed intelligence sources (e.g., tracking airplane movements). These could in return be used to prompt a more focussed earth system observation that would provide complementary data to better understand the scale and effect of such tests or deployments.

However, even in such scenarios, challenges would remain in **attribution, impact quantification, and counterfactual analysis** – that is, determining what would have happened in the absence of intervention. Addressing these challenges requires advances in modelling, observational integration, and uncertainty quantification.

3.8 Towards a scientific-technical roadmap

A cross-cutting insight of the STATISTICS project is the value of **systematising detectability thresholds for different SRM techniques and intervention scales**. Such thresholds could serve multiple purposes:

- Informing policymakers about which activities are likely to be observable and which may go unnoticed;
- Supporting the responsible design of field experiments by aligning permissible scales of experiments or tests with monitoring capabilities;
- Clarifying distinctions between small-scale research activities and large-scale tests in public and policy debates including in particular based on an understanding of the level of risk for significant transboundary harm (which may likely be the legal threshold).

Developing such thresholds requires integrating technical parameters with non-technical considerations, including governance norms, risk tolerance, and transparency expectations. Engagement with stakeholders, research funders, and parallel initiatives – such as Co-CREATE – would therefore be essential.

Taken together, the STATISTICS findings support the development of a **scientific and technical roadmap** that links research priorities, observation system investments, and governance-relevant monitoring objectives. Such a roadmap would provide a structured basis for future European engagement with SRM research, monitoring, and international dialogue.

Chapter 4. Conclusions

We summarize here the main achievements of the STATISTICS project:

- A preliminary intercomparison of four global stratospheric aerosol models for the Ambae, Raikoke and Ulawun eruptions in 2019 and a comparison against satellite observations of the size distribution evolution,
- A unique synergetic retrieval of aerosol properties for the post-2018 degassing of the Kilauea volcano in Hawaï and an analysis of how the aerosols has influenced cloud amount and reflectivity in the Tropical Pacific Ocean region,
- An evaluation of the statistics of cloud phase and ice crystal number concentrations in a climate model against satellite observations and new simulations of how dust seeding affects mixed-phase clouds and cirrus clouds in the Arctic region,
- An intercomparison of the effects of stratospheric aerosols on direct and diffuse surface radiation between the GRASP and libRadtran radiative transfer models, and a further comparison to observations,
- An analysis of how the altitude of SAI impact on surface radiation translates into changes in PV yields and to which extent this can be mitigated by re-optimizing the PV array layout,
- Simulations of the detectability of early SAI experiments with new-generation satellite instruments, highlighting the added value of two new concept instruments over the current capability to detect early SAI.
- The joint organization with Action4Cooling of an interdisciplinary SRM workshop at the intersection between Earth Observation, climate modelling, and research on SRM governance.
- Dissemination of findings on the role of Earth Observation (EO) in supporting Solar Radiation Modification (SRM) research, and active engagement with stakeholders at European and international levels, including dialogue with experts, initiatives and other projects addressing atmospheric modelling and research governance.

Despite substantial progress, STATISTICS has highlighted remaining knowledge gaps.

- The spatial and temporal variations in the particle size following the eruptions of Raikoke and Ulawu differ among the models. While some models reproduce some aspects of the observed variations, none of the models represent all of the observed features. Yet the efficacy of SAI is likely to be strongly dependent on how the stratospheric aerosol size distribution evolves so it is important to have confidence in the model’s capability to simulate aerosol size.

- Analysis of the co-variations in aerosol and cloud properties before and after the Kilauae degassing in the tropical Pacific Ocean show a cloud dimming effect, i.e. a reduction in cloud albedo. This signal is opposite in sign to the cloud brightening effect commonly inferred from other natural and anthropogenic aerosol perturbations. These results require further investigation to document changes in cloud microphysical properties (e.g. cloud droplet number concentration or cloud droplet size) but also highlight the absence of a unified theoretical framework capable of reconciling contrasting cloud radiative responses to aerosol perturbations. Observations of gas, aerosol and clouds need to be combined with aerosol and climate models to study regional warming/cooling effects caused by natural and anthropogenic atmospheric emissions on clouds.
- Current climate models often lack robust representation of cirrus formation pathways, particularly the partitioning between homogeneous and heterogeneous freezing. The models also lack an evaluation of the occurrence and characteristics of ice supersaturated regions (ISSRs), which are well established observationally to be conducive to homogeneous freezing. This uncertainty directly affects the simulation of cirrus cloud properties, their radiative impact and the quantification of the potential of CCT.
- The detectability of the impacts of early SAI deployments (near- or mid-term experiments) on the stratospheric composition, e.g. on the stratospheric ozone layer, are still to be quantitatively evaluated.

Across Solar Aerosol Injection (SAI), Marine Cloud Brightening (MCB), and Cirrus Cloud Thinning (CCT), both modelling and observational activities conducted in STATISTICS indicate that structural uncertainties remain dominant over parametric uncertainties. For SAI, differences in nucleation schemes and model numerics alone can lead to different outcomes on the evolution of the aerosol size distribution. In MCB studies, contrasting responses across regions and/or natural analogues may reflect genuine regime dependence, but methodological differences between studies (i.e., structural assumptions in experimental design and diagnostics) cannot be ruled out. For CCT, the representation of ice microphysical processes and associated parametrisations remains a central modelling issue. Collectively, these findings suggest that uncertainty is primarily rooted in process representation and model architecture rather than in the tuning of individual parameters.

Solar Radiation Modification (SRM) entails multiple layers of risk that must be evaluated with care. Physical risks associated with large-scale deployment include unintended regional climate responses (e.g., perturbations of precipitation patterns), stratospheric chemistry effects (e.g. ozone depletion in the case of SAI), and termination shock in the event of abrupt cessation. Field experiments represent a particular challenge when

discussing SRM (Rechmond Roche et al., 2025; Hernandez-Galindo et al., 2025; co-CREATE project). Small-scale field experiments are generally not thought to carry physical risks. Large-scale field experiments may carry physical risks, whose magnitude depends on the magnitude of the field experiments, including localized atmospheric perturbations. The possibility of technological side effects also needs to be considered. Detection of field experiments represents an ongoing challenge.

Beyond physical impacts, SRM research also raises societal and governance risks. These include moral hazard concerns, geopolitical tensions linked to unilateral action, uneven distribution of risks and benefits, and erosion of trust if research is perceived as advancing deployment agendas without broad societal consent. Governance frameworks remain fragmented, and international norms are still evolving in a context where scientific understanding is incomplete.

These risks must be weighed against the need for robust research to inform policy decisions. In an international landscape where SRM remains controversial yet increasingly discussed in scientific and policy arenas, insufficient knowledge may itself constitute a risk, particularly if future climate impacts intensify. Advancing transparent, internationally coordinated research (with strong governance safeguards) is therefore essential to enable evidence-based decision-making while minimizing both physical and societal harms.

Monitoring capacities need improving and factor in the possibility of coordinated field campaigns or unilateral tests. STATISTICS has focused on detectability issues for SAI experiments. A monitoring capacity for the stratosphere represents a priority in the context of SRM given the central role of SAI in the SRM portfolio, the current state of the observing system, and already-planned future missions.

Technical work that enables detecting and continual monitoring of both desired and undesired SRM activities may hold great significance as outlined by the Science Advisors recommendations. This may include the prevention of near-term deployment, crucial data support for research and international assessments, and, if done collaboratively and transparently, strengthen international relations and science-diplomacy for future decisions on SRM. The international discussion mirrors this growing recognition of the importance of technical and scientific work in this area.

References

Bani, P., C. Oppenheimer, P. Allard, H. Shinohara, V. Tsanev, S. Carn, M. Lardy, E. Garaebiti, First estimate of volcanic SO_2 budget for Vanuatu island arc, *Journal of Volcanology and Geothermal Research*, 211-212, 36-46, doi: 0.1016/j.jvolgeores.2011.10.005, 2012.

Baur, S., B.M. Sanderson, R. Séférian, and L. Terray, Solar radiation modification challenges decarbonization with renewable solar energy, *Earth Syst. Dynam.*, 15, 307–322, doi: 10.5194/esd-15-307-2024, 2024.

Bellamy, R., J. Chilvers, N.E. Vaughan, and T.M. Lenton, A review of climate geoengineering appraisals, *WIREs Clim Change*, 3: 597-615, doi: 10.1002/wcc.197, 2012

Bernath, P., C. Boone, A. Pastorek, D. Cameron, M. Lecours, Satellite characterization of global stratospheric sulfate aerosols released by Tonga volcano, *Journal of Quantitative Spectroscopy and Radiative Transfer*, 299, 108520, doi: 10.1016/j.jqsrt.2023.108520, 2023.

Biermann, F., et al., Solar geoengineering: The case for an international non-use agreement. WIREs *Climate Change*, 13(3), e754, doi: 10.1002/wcc.754, 2022 & https://www.solargeoeng.org/

Boichu, M., R. Grandin, L. Blarel, B. Torres, Y. Derimian, P. Goloub, et al, Growth and global persistence of stratospheric sulfate aerosols from the 2022 Hunga Tonga–Hunga Ha'apai volcanic eruption. *Journal of Geophysical Research: Atmospheres*, 128, e2023JD039010.doi: 10.1029/2023JD039010, 2023.

Boichu, M., T. Mathurin, VOLCPLUME, an interactive web portal for the multiscale analysis of volcanic plume physico-chemical properties [Interactive web-based resource]. https://doi.org/10.25326/362, 2022.

Bourassa, A. E., L. A. Rieger, N. D. Lloyd, and D. A. Degenstein, Odin-OSIRIS stratospheric aerosol data product and SAGE III intercomparison, *Atmos. Chem. Phys*., 12, 605–614, doi: 10.5194/acp-12-605-2012, 2012.

Bozzo, Alessio, et al. "An aerosol climatology for global models based on the tropospheric aerosol scheme in the Integrated Forecasting System of ECMWF." *Geoscientific Model Development* 13.3 (2020): 1007-1034.

Breen, K. H., Barahona, D., Yuan, T., Bian, H., and James, S. C.: Effect of volcanic emissions on clouds during the 2008 and 2018 Kilauea degassing events, *Atmos. Chem. Phys.*, 21, 7749-7771, doi: 10.5194/acp-21-7749-2021, 2021.

Brent, K., Simon, M., McDonald, J. From informal to formal governance of solar radiation management. *Climate Policy*, 1-18, 2024.

Buriez, J. C., Vanbauce, C., Parol, F., Goloub, P., Herman, M., Bonnel, B., Fouquart, Y., Couvert, P., and Seze, G.: Cloud detection and derivation of cloud properties from POLDER, *Int. J. Remote Sens.*, 18, 2785–2813, doi: 10.1080/014311697217332, 1997.

Carn, S., V. Fioletov, C. McLinden, et al. A decade of global volcanic SO_2 emissions measured from space. *Sci. Rep.*, 7, 44095, doi: 10.1038/srep44095, 2017.

Chen, Y., Haywood, J., Wang, Y. *et al.* Substantial cooling effect from aerosol-induced increase in tropical marine cloud cover. *Nat. Geosci.* 17, 404-410, doi: 10.1038/s41561-024-01427-z, 2024.

Christensen, M. W., et al., Opportunistic experiments to constrain aerosol effective radiative forcing, *Atmos. Chem. Phys.*, 22, 641–674,2022. doi: 10.5194/acp-22-641-2022.

Climate Overshoot Commission, https://www.overshootcommission.org/report, 2023.

Cuesta, J., Lopatin, A., Flamant, C., El Amraoui, L., Ferreira De Brito, J., Mallet, M., Sicard, M., Turquety, S., Di Biagio, C., Formenti, P., Khaykin, S., Xueref-Remy, I., Gros, V., Noël, V., Petit, J.-E., Torres, B., Qayyum, F., and Merdji, A.: Overview of French efforts for the innovative characterisation of aerosols and cloud interactions with the future Atmosphere Observing System, EGU General Assembly 2025, Vienna, Austria, 27 Apr–2 May 2025, EGU25-14129, doi: 10.5194/egusphere-egu25-14129, 2025.

Derimian, Y., Dubovik, O., Huang, X., Lapyonok, T., Litvinov, P., Kostinski, A. B., Dubuisson, P., and Ducos, F., Comprehensive tool for calculation of radiative fluxes: illustration of shortwave aerosol radiative effect sensitivities to the details in aerosol and underlying surface characteristics, *Atmos. Chem. Phys.*, 16, 5763–5780, doi: 10.5194/acp-16-5763-2016, 2016.

Deuzé, J. L., Goloub, P., Herman, M., Marchand, A., Perry, G., Susana, S., and Tanré, D.: Estimate of the aerosol properties over the ocean with POLDER, *J. Geophys. Res. Atmos.*, 105, 15329– 15346, doi: 10.1029/2000JD900148, 2000.

Diamond, M.S., A. Gettelman, M.D. Lebsock, A. McComiskey, L.M. Russell, R. Wood, & G. Feingold, To assess marine cloud brightening's technical feasibility, we need to know what to study—and when to stop, *Proc. Natl. Acad. Sci. U.S.A.*, 119, e2118379119, doi: 10.1073/pnas.2118379119, 2022.

Diamond, M.S., Detection of large-scale cloud microphysical changes within a major shipping corridor after implementation of the International Maritime Organization 2020 fuel sulfur regulations, *Atmos. Chem. Phys.*, 23, 8259-8269, doi:10.5194/acp-23-8259-2023, 2023.

Duchamp, C., F. Wrana, B. Legras, P. Sellitto, R. Belhadji, and C. von Savigny, Observation of the aerosol plume from the 2022 Hunga Tonga—Hunga Ha'apai eruption with SAGE III/ISS. *Geophysical Research Letters*, 50, e2023GL105076, doi: 10.1029/2023GL105076, 2023.

Eastham, S.E., A.H. Butler, S.J. Doherty, B. Gasparini, S. Tilmes, E.M. Bednarz, U. Burkhardt, G. Chiodo, D. J Cziczo, M.S. Diamond, D.W. Keith, T. Leisner, D.G. Macmartin, J. Quaas, P.J. Rasch, O. Sourdeval, I. Steinke, C. Thompson, D. Visioni, R. Wood, L. Xia, P Yu, Addressing

gaps in scientific knowledge could improve accuracy of climate intervention assessments, submitted, 2025.

Elias, T., Ferlay, N., Chesnoiu, G., Chiapello, I., and Moulana, M.: Regional validation of the solar irradiance tool SolaRes in clear-sky conditions, with a focus on the aerosol module, Atmos. Meas. Tech., 17, 4041-4063, doi: 10.5194/amt-17-4041-2024, 2024.

Feingold et al., Physical science research needed to evaluate the viability and risks of marine cloud brightening. *Sci. Adv.*, 10, eadi8594, doi: 10.1126/sciadv.adi8594, 2024.

Flament, T., D. Trapon, A. Lacour, A, Dabas, F. Ehlers, and D. Huber, Aeolus L2A aerosol optical properties product: standard correct algorithm and Mie correct algorithm, *Atmos. Meas. Tech.,* 14, 7851-7871, doi: 10.5194/amt-14-7851-2021, 2021.

Flower, V.J.B., and R.A. Kahn, Twenty years of NASA-EOS multi-sensor satellite observations at Kīlauea volcano (2000–2019), *Journal of Volcanology and Geothermal Research*, 415, doi: 10.1016/j.jvolgeores.2021.107247, 2021.

Fougnie, B., Marbach, T., Lacan, A., Lang, R., Schlüssel, P., Poli, G., Munro, R., and Couto, A. B.: The multiviewing multi-channel multi-polarisation imager – Overview of the 3MI polarimetric mission for aerosol and cloud characterization, *J. Quant. Spectrosc. Rad. Transfer*, 219, 23–32, doi: 10.1016/j.jqsrt.2018.07.008, 2018.

Gasparini, B., Z. McGraw, T. Storelvmo and U. Lohmann, To what extent can cirrus cloud seeding counteract global warming?, *Env. Res. Letts*., 15, 5, doi: 10.1088/1748-9326/ab71a3, 2020.

Gjelsvik, A. B., David, R. O., Carlsen, T., Hellmuth, F., Hofer, S., McGraw, Z., Sodemann, H., and Storelvmo, T. (2025). Using a region-specific ice-nucleating particle parameterization improves the representation of Arctic clouds in a global climate model. *Atmospheric Chemistry and Physics*, *25*(3), 1617-1637, doi: 10.5194/acp-25-1617-2025

Gkikas, A., Gialitaki, A., Binietoglou, I., Marinou, E., Tsichla, M., Siomos, N., Paschou, P., Kampouri, A., Voudouri, K. A., Proestakis, E., Mylonaki, M., Papanikolaou, C.-A., Michailidis, K., Baars, H., Straume, A. G., Balis, D., Papayannis, A., Parrinello, T., and Amiridis, V.: First assessment of Aeolus Standard Correct Algorithm particle backscatter coefficient retrievals in the eastern Mediterranean, *Atmos. Meas. Tech.*, 16, 1017-1042, doi: 10.5194/amt-16-1017-2023, 2023.

Grandin, R., M. Boichu, T. Mathurin, and N. Pascal, Automatic estimation of daily volcanic sulfur dioxide gas flux from TROPOMI satellite observations: Application to Etna and Piton de la Fournaise. *Journal of Geophysical Research: Solid Earth*, 129, e2024JB029309, doi: 10.1029/2024JB029309, 2024.

Gryspeerdt, E., J. Quaas, T. Goren, D. Klocke, and M. Brueck, An automated cirrus classification, *Atmos. Chem. Phys*., 18, 6157–6169, doi: 10.5194/acp-18-6157-2018, 2018.

Gryspeerdt, E., O. Sourdeval, J. Quaas, J. Delanoë, M. Krämer, and P. Kühne, Ice crystal number concentration estimates from lidar–radar satellite remote sensing – Part 2: Controls on the ice

crystal number concentration, *Atmos. Chem. Phys.,* 18, 14351-14370, doi: 10.5194/acp-18-14351-2018, 2018.

Hasekamp, O. P., Fu, G., Rusli, S. P., Wu, L., Di Noia, A., aan de Brugh, J., Landgraf, J., Martijn Smit, J., Rietjens, J., and van Amerongen, A.: Aerosol measurements by SPEXone on the NASA PACE mission: expected retrieval capabilities, *J. Quant. Spectrosc. Rad. Transfer*, 227, 170-184, doi: 10.1016/j.jqsrt.2019.02.006, 2019.

Haywood, J. M., et al., Observations of the eruption of the Sarychev volcano and simulations using the HadGEM2 climate model, *J. Geophys. Res.*, 115, D21212, doi:10.1029/2010JD014447, 2010.

Haywood, J.M., O. Boucher, C. Lennard, T. Storelvmo, S. Tilmes, and D. Visioni, World Climate Research Program Lighthouse Activity: An assessment of major research gaps in solar radiation modification research, *Frontiers in Climate*, doi: 10.3389/fclim.2025.1507479, 2025.

Hernandez-Galindo, I., A. Määttänen, B.H. Redmond Roche, O. Boucher, P. Irvine, and J. C. Moore, Solar radiation modification past field experiments: A review of the scientific and technical aspects for governance, *submitted*, 2025.

Hofer, S., L.C. Hahn, J.K. Shaw, *et al.* Realistic representation of mixed-phase clouds increases projected climate warming. *Commun Earth Environ* 5, 390, doi: 10.1038/s43247-024-01524-2, 2024.

Höpfner, M., B. Funke, S. Bender, Q. Errera, B.-M. Sinnhuber, J. Ungermann, D-04-01 CAIRT LINEAR SWB ATBDD14-4-README-3, CAIRT PERREC, 2025.

Jörimann, A., Sukhodolov, T., Luo, B., Chiodo, G., Mann, G., and Peter, T.: REtrieval Method for optical and physical Aerosol Properties in the stratosphere (REMAPv1), *Geosci. Model Dev.*, 18, 6023-6041, doi: 10.5194/gmd-18-6023-2025, 2025.

Kahn, R. A., Gaitley, B. J., Garay, M. J., Diner, D. J., Eck, T. F., Smirnov, A., and Holben, B. N.: Multiangle Imaging SpectroRadiometer global aerosol product assessment by comparison with the Aerosol Robotic Network, *J. Geophys. Res.*, 115, D23209, doi: 10.1029/2010JD014601, 2010.

Kleinschmitt, C., O. Boucher, S. Bekki, F. Lott, and U. Platt, The Sectional Stratospheric Sulfate Aerosol module S3A-v1 within the LMDZ general circulation model: Description and evaluation against stratospheric aerosol observations, *Geosc. Mod. Dev.*, 10, 3359-3378, doi:10.5194/gmd-10-3359-2017, 2017.

Kloss, C., Sellitto, P., Legras, B., Vernier, J.-P., Jégou, F., Venkat Ratnam, M., et al. Impact of the 2018 Ambae eruption on the global stratospheric aerosol layer and climate. J*ournal of Geophysical Research: Atmospheres*, 125, e2020JD032410, doi:10.1029/2020JD032410, 2020.

Kloss, C., G. Berthet, P. Sellitto, F. Ploeger, G. Taha, M. Tidiga, M. Eremenko, A. Bossolasco, F. Jégou, J.-B. Renard, and B. Legras, Stratospheric aerosol layer perturbation caused by the 2019

Raikoke and Ulawun eruptions and their radiative forcing, *Atmos. Chem. Phys.,* 21, 535–560, doi: 10.5194/acp-21-535-2021, 2021.

Kok, J.F., A.A. Adebiyi, S. Albani, Y. Balkanski, R. Checa-Garcia, M. Chin, P.R. Colarco, D.S. Hamilton, Y. Huang, A. Ito, M. Klose, L. Li, N.M. Mahowald, R.L. Miller, V. Obiso, C. Pérez García-Pando, A. Rocha-Lima, and J.S. Wan, Contribution of the world's main dust source regions to the global cycle of desert dust, *Atmos. Chem. Phys*., 21, 8169–8193, doi: 10.5194/acp-21-8169-2021, 2021.

Kovilakam, M., L.W. Thomason, N. Ernest, L. Rieger, A. Bourassa, and L. Millán, The Global Space-based Stratospheric Aerosol Climatology (version 2.0): 1979–2018, *Earth Syst. Sci. Data*, 12, 2607-2634, doi: 10.5194/essd-12-2607- 2020, 2020.

Kovilakam, M., L. Thomason, and T. Knepp, SAGE III/ISS aerosol/cloud categorization and its impact on GloSSAC, *Atmos. Meas. Tech*., 16, 2709–2731, doi: 10.5194/amt-16-2709-2023, 2023.

Kravitz, B., et al., Climate model response from the Geoengineering Model Intercomparison Project (GeoMIP), *J. Geophys. Res. Atmos.*, 118, 8320–8332, doi:10.1002/jgrd.50646, 2013.

Kravitz, B., Robock, A., Tilmes, S., Boucher, O., English, J. M., Irvine, P. J., Jones, A., Lawrence, M. G., MacCracken, M., Muri, H., Moore, J. C., Niemeier, U., Phipps, S. J., Sillmann, J., Storelvmo, T., Wang, H., and Watanabe, S., The Geoengineering Model Intercomparison Project Phase 6 (GeoMIP6): simulation design and preliminary results, *Geosci. Model Dev.*, 8, 3379-3392, doi: 10.5194/gmd-8-3379-2015, 2015.

Kremser, S., Thomason, L. W., von Hobe, M., Hermann, M., Deshler, T., Timmreck, C., Toohey, M., Stenke, A., Schwarz, J. P., Weigel, R., Fueglistaler, S., Prata, F. J., Vernier, J.-P., Schlager, H., Barnes, J. E., Antuña-Marrero, J.-C., Fairlie, D., Palm, M., Mahieu, E., Notholt, J., Rex, M., Bingen, C., Vanhellemont, F., Bourassa, A., Plane, J. M. C., Klocke, D., Carn, S. A., Clarisse, L., Trickl, T., Neely, R., James, A. D., Rieger, L., Wilson, J. C., and Meland, B.: Stratospheric aerosol – observations, processes, and impact on climate, *Rev. Geophys.*, 54, 278-335, doi: 10.1002/2015RG000511, 2016.

Kumler, A., B. Kravitz, C. Draxl, L. Vimmerstedt, B. Benton, J. K. Lundquist, M. Martin, H. J. Buck, H. Wang, C. Lennard, L. Tao, Potential effects of climate change and solar radiation modification on renewable energy resources, *Renewable and Sustainable Energy Reviews*, 207, doi: 10.1016/j.rser.2024.114934, 2025.

Hou, X., Wild, M., Folini, D., Kazadzis, S., and Wohland, J.: Climate change impacts on solar power generation and its spatial variability in Europe based on CMIP6, *Earth Syst. Dynam*., 12, 1099-1113, doi: 10.5194/esd-12-1099-2021, 2021.

Lange, A., U. Niemeier, A. Rozanov, and C. von Savigny, Investigating the ability of satellite occultation instruments to monitor possible geoengineering experiments, *EGUsphere* [preprint], doi: 10.5194/egusphere-2025-1005, 2025.

Li L, Dubovik O, Derimian Y, Schuster GL, Lapyonok T, Litvinov P, Ducos F, Fuertes D, Chen C, Li Z, Lopatin A. Retrieval of aerosol components directly from satellite and ground-based measurements. *Atmos. Chem. Phys.*, 19, 13409-13443, 2019.

Määttänen, A., Merikanto, J., Henschel, H., Duplissy, J., Makkonen, R., Ortega, I. K., and Vehkamaki, H.: New parameterizations for neutral and ion-induced sulfuric acid-water particle formation in nucleation and kinetic regimes, *J. Geophys. Res.-Atmos.*, 123, 1269–1296, doi:10.1002/2017JD027429, 2018.

Malavelle, F., Haywood, J., Jones, A. *et al.* Strong constraints on aerosol–cloud interactions from volcanic eruptions. *Nature*, 546, 485-491, doi: 10.1038/nature22974, 2017.

Medcraft, C., W.A. Davis, and D. Harrison, Flash atomisation of saltwater through convergent divergent nozzles: implications for marine cloud brightening, preprint, 2025.

Mitchell, D. L., A. Garnier, J. Pelon, and E. Erfani, CALIPSO (IIR–CALIOP) retrievals of cirrus cloud ice-particle concentrations, *Atmos. Chem. Phys.*, 18, 17325-17354, doi: 10.5194/acp-18-17325-2018, 2018.

Moroney, C., and K. Mueller. MISR data product specification for the MISR Level 2 Cloud Product, 2012.

NASEM, Reflecting sunlight, Recommendations for solar geoengineering research and research governance, 2021.

Niemeier, U., & Timmreck, C., What is the limit of climate engineering by stratospheric injection of SO 2?. *Atmospheric Chemistry and Physics*, *15*(16), 9129-9141, doi:10.5194/acp-15-9129-2015, 2015.

O'Neill, B. C., Tebaldi, C., van Vuuren, D. P., Eyring, V., Friedlingstein, P., Hurtt, G., Knutti, R., Kriegler, E., Lamarque, J.-F., Lowe, J., Meehl, G. A., Moss, R., Riahi, K., and Sanderson, B. M.: The Scenario Model Intercomparison Project (ScenarioMIP) for CMIP6, *Geosci. Model Dev*., 9, 3461-3482, doi: 10.5194/gmd-9-3461-2016, 2016.

Pfeifroth, U., Drücke, J., Kothe, S., Trentmann, J., Schröder, M., and Hollmann, R.: SARAH-3 – satellite-based climate data records of surface solar radiation, *Earth Syst. Sci. Data*, 16, 5243–5265, doi:10.5194/essd-16-5243-2024, 2024.

Philippe, S. Monitoring and Verifying the Deployment of Solar Geoengineering In: Governance of the Deployment of Solar Geoengineering. Edited by Robert N. Stavins and Robert C. Stowe. Cambridge, Mass.: Harvard Project on Climate Agreements, February 2019.

Prilliman, M., *et al*., Technoeconomic analysis of changing PV array convective cooling through changing array spacing, *IEEE Journal of Photovoltaics*, 12, 6, 1586-1592, doi: 10.1109/JPHOTOV.2022.3201464, 2022.

Quaglia, I., Visioni, D., Pitari, G., and Kravitz, B.: An approach to sulfate geoengineering with surface emissions of carbonyl sulfide, *Atmos. Chem. Phys.*, 22, 5757–5773, doi:10.5194/acp-22-5757-2022, 2022.

Qayyum, F., J. Cuesta, A.B. Merdji, A. Lopatin, O. Dubovik, D. Nandan Piyush, L. El Amraoui, and R. Ferrare, Vertical distribution of the concentrations of multiple aerosol types derived from the multiwavelength spaceborne lidar of the future Atmosphere Observing System, EGU General Assembly 2025, Vienna, Austria, 27 Apr–2 May 2025, EGU25-15896, doi: 10.5194/egusphere-egu25-15896, 2025.

Quaglia, I., Timmreck, C., Niemeier, U., Visioni, D., Pitari, G., Brodowsky, C., Brühl, C., Dhomse, S. S., Franke, H., Laakso, A., Mann, G. W., Rozanov, E., and Sukhodolov, T.: Interactive stratospheric aerosol models' response to different amounts and altitudes of SO_2 injection during the 1991 Pinatubo eruption, *Atmos. Chem. Phys.,* 23, 921–948, doi:10.5194/acp-23-921-2023, 2023.

Raptis, P.I., S. Kazadzis, B. Psiloglou, N. Kouremeti, P. Kosmopoulos, A. Kazantzidis, Measurements and model simulations of solar radiation at tilted planes, towards the maximization of energy capture, *Energy*, 130, doi: 10.1016/j.energy.2017.04.122, 2017.

Redmond Roche, B.H., I. Hernandez-Galindo, A. Määttänen, J.C. Moore, O. Boucher, M. Dollner, A. Duffey, B. Gasparini, A. N. Koyun, D. McGrath, I. Steinke, J. Vinders, D. Visioni, and P.J. Irvine, Assessment of plausible solar radiation modification field experiments from an expert-led workshop reveals the need for differentiated governance, *Earth's Future*, submitted, 2025.

Richter, J. H., Visioni, D., MacMartin, D. G., Bailey, D. A., Rosenbloom, N., Dobbins, B., Lee, W. R., Tye, M., and Lamarque, J.-F., Assessing Responses and Impacts of Solar climate intervention on the Earth system with stratospheric aerosol injection (ARISE-SAI): protocol and initial results from the first simulations, Geosci. Model Dev., 15, 8221-8243, doi: 10.5194/gmd-15-8221-2022, 2022.

Rémy, S., et al. Description and evaluation of the tropospheric aerosol scheme in the European Centre for Medium-Range Weather Forecasts (ECMWF) Integrated Forecasting System (IFS-AER, cycle 45R1). *Geoscientific Model Development* 12.11 (2019): 4627-4659.

Salter S., G. Sortino and J. Latham, Sea-going hardware for the cloud albedo method of reversing global warming, *Phil. Trans. R. Soc. A.*, 366, 3989–4006, 2008.

SAPEA, Solar radiation modi!cation. Berlin: SAPEA, doi: 10.5281/zenodo.14283096, 2024.

Schleussner, C.F., et al., Overconfidence in climate overshoot. *Nature*, 634, 366-373, 2024.

Schmidt, A. *et al.*, Satellite detection, long-range transport, & air quality impacts of volcanic sulfur dioxide from the 2014–2015 flood lava eruption at Bárðarbunga (Iceland). *J. Geophys. Res*, 9739-9757, 2015. doi: doi:10.1002/2015JD023638.

Seidel, D.J., Feingold, G., Jacobson, A.R. and Loeb, N., 2014. Detection limits of albedo changes induced by climate engineering. *Nature Climate Change*, *4*(2), pp.93-98.

Seland, Ø., Bentsen, M., Olivié, D., Toniazzo, T., Gjermundsen, A., Graff, L. S., ... and Schulz, M., Overview of the Norwegian Earth System Model (NorESM2) and key climate response of CMIP6 DECK, historical, and scenario simulations, *Geosci. Model Dev.*, 13, 6165–6200, doi: 10.5194/gmd-13-6165-2020, 2020.

Sellitto, P., A. Podglajen, R. Belhadji, *et al.* The unexpected radiative impact of the Hunga Tonga eruption of 15th January 2022. *Commun. Earth Environ.,* 3, 288, doi:10.1038/s43247-022-00618-z, 2022.

Sellitto, P., R. Belhadji, J. Cuesta, A. Podglajen, and B. Legras, Radiative impacts of the Australian bushfires 2019–2020 - Part 2: Large-scale and in-vortex radiative heating, *Atmos. Chem. Phys.,* 23, 15523-15535, doi: 10.5194/acp-23-15523-2023, 2023.

Sellitto, P., R. Siddans, R. Belhadji, E. Carboni, B. Legras, A. Podglajen, C. Duchamp, and B. Kerridge, Observing the SO_2 and sulfate aerosol plumes from the 2022 Hunga eruption with the Infrared Atmospheric Sounding Interferometer (IASI). *Geophy. Res. Letts.*, 51, e2023GL105565. doi: 10.1029/2023GL105565, 2024.

Shreve, T., Grandin, R., Boichu, M. et al. From prodigious volcanic degassing to caldera subsidence and quiescence at Ambrym (Vanuatu): the influence of regional tectonics. *Sci. Rep.,* 9, 18868, doi: 10.1038/s41598-019-55141-7, 2019.

Smith, W., The cost of stratospheric aerosol injection through 2100, *Environ. Res. Lett.* 15, 114004, doi: 10.1088/1748-9326/aba7e7, 2020.

Smith, C.J., Crook J.A., Crook R., et al., Impacts of stratospheric sulfate geoengineering on global solar photovoltaic and concentrating solar power resource. *Journal of Applied Meteorology and Climatology*, 56, 1483-1497, doi:10.1175/JAMC-D-16-0298.s1, 2017.

Sofieva, V.F., A. Rozanov, M. Szelag, J.P. Burrows, C. Retscher, R. Damadeo, D. Degenstein, L.A. Rieger, and A. Bourassa, CREST: a Climate Data Record of Stratospheric Aerosols, *Earth Syst. Sci. Data*, 16, 5227–5241, doi: 10.5194/essd-16-5227-2024, 2024.

Solar radiation modification: a call for balanced research, https://www.call-for-balance.com/letter

Storelvmo, T., and N. Herger, Cirrus cloud susceptibility to the injection of ice nuclei in the upper troposphere, *J. Geophys. Res. Atmos.*, 119, 2375-2389, doi:10.1002/2013JD020816, 2014.

Tackett, J. L., Kar, J., Vaughan, M. A., Getzewich, B. J., Kim, M.-H., Vernier, J.-P., Omar, A. H., Magill, B. E., Pitts, M. C., and Winker, D. M.: The CALIPSO version 4.5 stratospheric aerosol subtyping algorithm, *Atmos. Meas. Tech.*, 16, 745-768, doi: 10.5194/amt-16-745-2023, 2023.

Tilmes, S., et al., CESM1(WACCM) Stratospheric Aerosol Geoengineering Large Ensemble Project. *Bull. Amer. Meteor. Soc.*, 99, 2361-2371, doi: 10.1175/BAMS-D-17-0267.1, 2018.

Tilmes, S., MacMartin, D. G., Lenaerts, J. T. M., van Kampenhout, L., Muntjewerf, L., Xia, L., Harrison, C. S., Krumhardt, K. M., Mills, M. J., Kravitz, B., and Robock, A.: Reaching 1.5 and 2.0 °C global surface temperature targets using stratospheric aerosol geoengineering, *Earth Syst. Dynam*., 11, 579-601, doi: 10.5194/esd-11-579-2020, 2020.

Timmreck, C., Mann, G. W., Aquila, V., Hommel, R., Lee, L. A., Schmidt, A., Brühl, C., Carn, S., Chin, M., Dhomse, S. S., Diehl, T., English, J. M., Mills, M. J., Neely, R., Sheng, J., Toohey, M., and Weisenstein, D., The Interactive Stratospheric Aerosol Model Intercomparison Project (ISA-MIP): motivation and experimental design, *Geosci. Model Dev.*, 11, 2581-2608, doi:10.5194/gmd-11-2581-2018, 2018.

Toll, V., Christensen, M., Gassó, S., & Bellouin, N.. Volcano and ship tracks indicate excessive aerosol-induced cloud water increases in a climate model. *Geophysical Research Letters*, 44, 12,492-12,500, doi: 10.1002/2017GL075280, 2017.

Toll, V., *et al.*, Glaciation of liquid clouds, snowfall, and reduced cloud cover at industrial aerosol hot spots.*Science,* 386,756-762, doi: 10.1126/science.adl0303, 2024.

Trepte et al., CALIGOLA: A New Spaceborne Lidar Mission, International Symposium on Spaceborne Lidar, https://ntrs.nasa.gov/api/citations/20240006526/downloads/CALIGOLA_Overview_StMalo.pdf, St Malo, France, June 2024

UNEP, United Nations Environment Programme, Emissions Gap Report 2023: Broken Record – Temperatures hit new highs, yet world fails to cut emissions (again). Nairobi. doi: 10.59117/20.500.11822/43922, 2023.

UNEP, United Nations Environment Programme, One Atmosphere: An independent expert review on Solar Radiation Modification research and deployment, 2024.

UNESCO, Report of the World Commission on the Ethics of Scientific Knowledge and Technology (COMEST) on the ethics of climate engineering, 2023.

Urbanek, B., S. Groß, M. Wirth, C. Rolf, M. Krämer, and C. Voigt, High depolarization ratios of naturally occurring cirrus clouds near air traffic regions over Europe. *Geophysical Research Letters*, 45, 13,166-13,172. doi: 10.1029/2018GL079345, 2018.

Vattioni, S., Stenke, A., Luo, B., Chiodo, G., Sukhodolov, T., Wunderlin, E., & Peter, T., Importance of microphysical settings for climate forcing by stratospheric SO2 injections as modeled by SOCOL-AERv2. *Geoscientific Model Development*, *17*(10), 4181-4197, doi: 10.5194/gmd-17-4181-2024, 2024.

Vattioni, S., Käslin, S. K., Dykema, J. A., Beiping, L., Sukhodolov, T., Sedlacek, J., Keutsch, F. N., Peter, T., & Chiodo, G. Microphysical interactions determine the effectiveness of Solar Radiation Modification via stratospheric solid particle injection. *Geophysical Research Letters*, 51(19). doi.org/10.1029/2024GL110575, 2024

Vattioni, S., Peter, T., Weber, R. *et al.* Injecting solid particles into the stratosphere could mitigate global warming but currently entails great uncertainties. *Commun Earth Environ* 6, 132, doi:10.1038/s43247-025-02038-1, 2025.

Vehkamaki, H., Kulmala, M., Napari, I., Lehtinen, K., Timmreck, C**.**, Noppel, M. & Laaksonen, A., An improved parameterization for sulfuric acid-water nucleation rates for tropospheric and stratospheric conditions. *Journal of Geophysical Research-Atmospheres*, *107*(D22): 4622. doi:10.1029/2002JD002184, 2002.

Visioni, D., MacMartin, D. G., Kravitz, B., Boucher, O., Jones, A., Lurton, T., Martine, M., Mills, M. J., Nabat, P., Niemeier, U., Séférian, R., and Tilmes, S.: Identifying the sources of uncertainty in climate model simulations of solar radiation modification with the G6sulfur and G6solar Geoengineering Model Intercomparison Project (GeoMIP) simulations, *Atmos. Chem. Phys*., 21, 10039–10063, doi: 10.5194/acp-21-10039-2021, 2021.

Visioni, D., A. Robock, J. Haywood, M. Henry, and A. Wells, A new era for the Geoengineering Model Intercomparison Project (GeoMIP). *Bull. Amer. Meteor. Soc.,* 104, E1950-E1955, doi: 10.1175/BAMS-D-23-0232.1, 2023.

Visioni, D., Robock, A., Haywood, J., Henry, M., Tilmes, S., MacMartin, D. G., Kravitz, B., Doherty, S. J., Moore, J., Lennard, C., Watanabe, S., Muri, H., Niemeier, U., Boucher, O., Syed, A., Egbebiyi, T. S., Séférian, R., and Quaglia, I.: G6-1.5K-SAI: a new Geoengineering Model Intercomparison Project (GeoMIP) experiment integrating recent advances in solar radiation modification studies, *Geosci. Model Dev*., 17, 2583–2596, doi: 10.5194/gmd-17-2583-2024, 2024.

Watson-Parris, D., M.W. Christensen, A. Laurenson, D. Clewley, E. Gryspeerdt, and P. Stier, Shipping regulations lead to large reduction in cloud perturbations. *Proceedings of the National Academy of Sciences*, 119(41), e2206885119, doi: 10.1073/pnas.2206885119, 2022.

WCRP Lighthouse activity on climate intervention, https://www.wcrp-climate.org/ci-overview, 2024.

Weisenstein, D. K., D. Visioni, H. Franke, U. Niemeier, S. Vattioni, G. Chiodo, T. Peter, and D.W. Keith, An interactive stratospheric aerosol model intercomparison of solar geoengineering by stratospheric injection of SO_2 or accumulation-mode sulfuric acid aerosols, *Atmos. Chem. Phys.*, 22, 2955–2973, doi: 10.5194/acp-22-2955-2022, 2022.

World Meteorological Organization (WMO). Scientific Assessment of Ozone Depletion: 2022, GAW Report No. 278, 509 pp.; WMO: Geneva, 2022.

Wood, R., Assessing the potential efficacy of marine cloud brightening for cooling Earth using a simple heuristic model, *Atmos. Chem. Phys.*, 21, 14507-14533, doi: 10.5194/acp-21-14507-2021, 2021.

Wrana, F., U. Niemeier, L.W. Thomason, S. Wallis, and C. von Savigny, Stratospheric aerosol size reduction after volcanic eruptions, *Atmos. Chem. Phys.*, 23, 9725-9743, doi: 10.5194/acp-23-9725-2023, 2023.

Wrana, F., von Savigny, C., Zalach, J., and Thomason, L. W.: Retrieval of stratospheric aerosol size distribution parameters using satellite solar occultation measurements at three wavelengths, *Atmos. Meas. Tech.,* 14, 2345-2357, doi: 10.5194/amt-14-2345-2021, 2021.

Yuan, T., H. Song, R. Wood, C. Wang, L. Oreopoulos, S.E. Platnick, et al., Global reduction in ship-tracks from sulfur regulations for shipping fuel. *Science Advances*, 8(29), eabn7988. Doi: 10.1126/sciadv.abn7988, 2022.

Zhang, Z., J.C. Moore, D. Huisingh, and Y. Zhao, Review of geoengineering approaches to mitigating climate change, *Journal of Cleaner Production*, 103, 898-907, doi: 10.1016/j.jclepro.2014.09.076, 2015.

Zhu, J., J. E. Penner, A. Garnier, O. Boucher, M. Gao, L. Song, et al., Decreased aviation leads to increased ice crystal number and a positive radiative effect in cirrus clouds. *AGU Advances*, 3, e2021AV000546, doi: 10.1029/2021AV000546, 2022.

Appendix

Appendix I

Appendix I provides supplementary information on the GRASP radiative transfer simulations (Chapter 2.4).

Refractive Indices of each aerosol type												
wvl (nm)	RRI (DU)	CRI (DU)	RRI (SS)	CRI (SS)	RRI (OM)	CRI (OM)	RRI (BC)	CRI (BC)	RRI (SU)	CRI (SU)	RRI (SU)	CRI (SU)
410.0	1.581823	0.005606	1.5	3.0e-8	1.53	0.005	1.6999	0.45	1.539650	1.0e-7	1.439	1.0e-8
443.0	1.553253	0.004214	1.5	3.0e-8	1.53	0.005	1.6999	0.45	1.537505	1.0e-7	1.4359	1.0e-8
490.0	1.555098	0.002680	1.5	2.0e-8	1.53	0.005	1.6999	0.45	1.534451	1.0e-7	1.4319	1.0e-8
555.0	1.555490	0.001414	1.499473	1.0e-8	1.53	0.006	1.6999	0.45	1.530288	1.0e-7	1.4299	1.0251e-8
670.0	1.550223	0.000543	1.490000	1.1e-7	1.53	0.007	1.6999	0.45	1.524640	1.0e-7	1.4284	1.7723e-8
865.0	1.535715	0.000526	1.480000	2.824e-5	1.52	0.011950	1.6999	0.45	1.517300	1.8e-7	1.4249	1.8987e-7
1623.7	1.526110	0.000304	1.454648	6.6421e-4	1.490195	0.020024	1.6999	0.45	1.488808	1.6064e-4	1.3984	2.2287e-4
2036.2	1.514857	0.000370	1.446722	1.56895e-3	1.420000	0.008289	1.6999	0.45	1.470661	1.20839e-3	1.3819	1.3303e-3
Source	Dubovik 2002		Hess 1998 [CAMS]		Ghosh 1999 [MERRA2]		Hess 1998 (modified) [CAMS]		Toon 1976		Hummel 1988	

Table A1: The refractive indices for various aerosols: DU, SS, OM, BC, and SU. A separate value is also provided for SU (Hummel 1988) specifically for use in aerosol injection. The source for each value is indicated in the bottom row.

GRASP's vertical grid structure: The GRASP model's vertical grid configuration is detailed below, showing layer heights relative to sea level (in meters):

[40000,35000,34000,33500,33000,32500,32000,31500,31000,30500,30000,29500,29000,28500,28000,27500,27000,26500,26000,25500,25000,24500,24000,23500,23000,22500,22000,21500,21000,20500,20000,19500,19000,18500,18000,17500,17000,16500,16000,15500,15000,14500,14000,13500,13000,12500,12000,11500,11000,10500,10000,9500,9000,8500,8000,7500,7000,6500,6000,5500,5000,4500,4000,3500,3000,2500,2000,1800,1600,1400,1200,1000,900,800,700,600,500,400,300,200,100,10]

2024	Dates	
Jan	11	20
Feb	15	17
Mar	04	22
Apr	13	23
May	10	11
Jun	07	09
Jul	29	30
Aug	05	27
Sep	15	19
Oct	11	24
Nov	04	29
Dec	26	27

Table A2: Cloud-free days, 2 days/month, selected for 2024 at SIRTA station.